5. SITE 907[1]

Shipboard Scientific Party[2]

HOLE 907A

Date occupied: 5 August 1993

Date departed: 8 August 1993

Time on hole: 2 days, 17 hr, 3 min

Position: 69°14.989′N, 12°41.894′E

Bottom felt (drill pipe measurement from rig floor, m): 1811.6

Distance between rig floor and sea level (m): 10.8

Water depth (drill pipe measurement from sea level, m): 1800.8

Total depth (from rig floor, m): 2035.7

Penetration (m): 224.1

Number of cores (including cores with no recovery): 26

Total length of cored section (m): 224.1

Total core recovered (m): 229.98

Core recovery (%): 102.6

Oldest sediment cored:
Depth (mbsf): 216.3
Nature: silty mud
Earliest age: Miocene

Hard rock:
Depth (mbsf): 216.3
Nature: basalt

Basement:
Depth (mbsf): 216.3
Nature: basalt

Principal results: Site 907 (proposed Site ICEP-1) is located in the southwestern part of the Norwegian-Greenland Sea, on the eastern Iceland Plateau West of the extinct Iceland Plateau spreading axis on oceanic crust of about magnetic Anomaly 6B-age (approximately 22–24 Ma). It is also West of the Jan Mayen Ridge (a microcontinent that originally was part of the Greenland continental margin). Site 907 is part of an intended paleoenvironmental transect from the Norwegian (ODP Leg 104) to the Greenland continental margin, as well as one of the southern tie points of a North-South transect through the North Atlantic-Arctic Gateways. Site 907 also was located on a relatively shallow part of the Iceland Plateau providing access to an undisturbed, flat-lying, pelagic sediment sequence.

The site location had been selected at shotpoint 400 of the ICEP1-89, Segment A multichannel seismic reflection line collected by University of Bergen, Norway. The seismic line could be correlated with confidence to the reflection data collected aboard the *JOIDES Resolution* during site approach, which together with the 3.5-kHz record also established the undisturbed nature of the pelagic sedimentary sequence.

Our plans were to conduct double or triple APC- and XCB-coring at this site to obtain a complete stratigraphic sequence of Neogene and Quaternary pelagic sediments and to reach basement. Hole 907A was APC-cored to 216.3 mbsf, where the core barrel bounced, indicating a hard interface. We then continued to XCB-core and achieved a total penetration of 224.1 mbsf; the last two cores were in basalt. After completion of Hole 907A, a successful logging program was run. A medical emergency requiring the immediate evacuation of a sick crew member prevented us from drilling the B and C holes.

Five sedimentary lithostratigraphic units were recognized at Site 907 (on top of the basalt encountered at 216.3 mbsf):

Unit I: (0–16.8 mbsf) Quaternary dark grayish brown to grayish brown clayey silts, silty clays, and foraminifer-bearing silty muds with minor amounts of biosilica-bearing silty carbonate ooze. Most color boundaries are gradational because of the pervasive bioturbation. This unit is distinguished by the presence of biogenic calcareous material, primarily foraminifers. In addition to the biogenic components, the coarse fractions consist of quartz, feldspar, and mica, with little volcanic glass. Dropstones (i.e., ice-rafted debris) >1 cm are rare.

Unit II: (16.8–56.3 mbsf) Pliocene to Pleistocene clayey silts and silty clays, characterized by the absence of biogenic carbonate and the abundance of silt- and sand-sized siliciclastic grains. The silts and clays are dark grayish brown to dark gray and gray and commonly massive, but sometimes show faint mottling. Volcanic glass is rare, increasing slightly toward the bottom of this unit.

Unit III: (56.3–118.1 mbsf) Upper Miocene to Pliocene clayey silts and silty clays, with biogenic silica, more volcanic glass than above, and a decrease in the percentages of quartz and feldspar. They are primarily dark olive gray, olive gray, and very dark gray. In addition to volcanic glass, the coarse fractions consist of quartz, feldspar, mica, and accessory minerals. Dropstones are found throughout. With the exception of ash layers, all lithology and color boundaries are gradational due to pervasive bioturbation. Two subunits can be defined: Subunit IIIA has interbedded nannofossil ooze and nannofossil silty clay, whereas Subunit IIIB does not.

Unit IV: (118.1–197.3 mbsf) Middle to upper Miocene dark greenish gray to dark gray ash- and biosilica-bearing silty clays and clayey silts, with greenish gray color bands throughout the unit. Moderate to intensive bioturbation is present throughout, giving the sediments a mottled appearance and resulting in many gradational color and lithology boundaries. Abundant, often graded ash layers ranging in thickness from 1 to 15 cm are common in the upper part of the unit.

Unit V: (197.3–216.3 mbsf) Middle Miocene dark olive gray clayey mud and silty clay, which is distinguished from Unit IV by its high quartz and clay and low biosilica contents. Mottling and color changes occur. Burrows are commonly filled with sand-sized volcanic glass.

The micropaleontological studies of the recovered sediment sequence at Site 907 demonstrated that it consists of Pliocene to Quaternary hemipelagic deposits, upper and middle Miocene biosiliceous oozes, and middle Miocene ash-rich muds. Siliceous microfossils in Core 21H-CC have an age of 14 Ma, whereas dinoflagellates suggest an age not older than 16 Ma for Core 23H-CC. Most major pelagic microfossil groups have con-

[1] Myhre, A.M., Thiede, J., Firth, J.V., et al., 1995. *Proc. ODP, Init. Repts.*, 151: College Station, TX (Ocean Drilling Program).

[2] Shipboard Scientific Party is as given in the list of participants preceding the Table of Contents.

tributed to a detailed biochronology that is supported by an excellent magnetostratigraphy.

Calculated bulk sedimentation rates range from about 10 to 20 m/m.y. in the upper Miocene to Quaternary part of the drilled section to >80 m/m.y. in the middle Miocene. Correlation to previous micropaleontological studies of DSDP Legs 38 and 94 and ODP Legs 104 and 105 proved difficult because of a number of factors: location of the new site under different water masses, better coring techniques, scarceness of calcareous materials, variable preservation of siliceous species, and high percentages of endemic species. Site 907 siliceous microfossil assemblages suggest highly productive surface waters during middle Miocene–early Pliocene. The subsequent decline of microfossil deposition and the increased presence of ice-rafted materials since late Pliocene, led to the deposition of overlying, mostly terrigenous sediments typical of glacial depositional environments.

Geochemical measurements documented the scarceness of calcareous materials, which are, with the exception of a few thin nannofossil-rich horizons in the Pliocene, restricted to the upper part of the Quaternary. Organic carbon contents were generally low, and the components are mostly of terrigenous origin. Shipboard physical property measurements and logging established the cyclic nature of most of the penetrated sediment column. The uphole increase in wet-bulk density and decrease in porosity occurs at roughly 55 mbsf, which coincides with the onset of major ice-rafted debris (IRD) deposition at about 2.6 Ma.

High heat-flow values (observed by the Adara tool and confirmed by logging), together with a number of geochemical anomalies, point to the possible existence of hydrothermal fluid flow through the deeper part of the sampled sequence.

The sedimentary sequence rests on top of acoustic basement consisting of nearly aphyric basalts probably erupted in shallow water (<500 m). Each of the recovered units is homogeneous and massive, distinguished by glassy tops and bottoms with abundant vesicles. They indicate that the cooling units are pillow basalts.

In summary, Site 907 fulfilled its objectives in as far as we collected a more or less complete Neogene and Quaternary paleoenvironmental section as the southern part of the North Atlantic-Arctic Gateways problem. However, it did not fulfill our expectations of a particularly high stratigraphic resolution section, or of extensive carbonate sedimentation in the Neogene and Quaternary on the Iceland Plateau.

BACKGROUND AND SCIENTIFIC OBJECTIVES

Background

The drill sites on the Iceland Plateau are part of a paleoenvironmental transect from Norway to Greenland to study the history of the advection of temperate, saline Atlantic waters to the Norwegian Sea and of cold, brackish, partly ice-covered Arctic waters to the Greenland and Iceland seas. This transect is designed to cover the climatically highly sensitive and variable thermal gradient between polar areas near East Greenland and temperate areas off Norway. The sites drilled on the Vøring Plateau during Leg 104 (Eldholm, Thiede, Taylor, et al., 1987b; 1989b) anchor the eastern end of the transect, and sites planned on the Greenland continental margin form its western end (see Fig. 17 of "Introduction" chapter, this volume). Site 907 is located between these end members and was supposed to monitor the history of oceanic and climatic fronts moving East and West across the Iceland Plateau, to derive an open-ocean record of ice-rafted debris (IRD) and carbonate, and to determine the history of formation of northern-source deep waters.

The Iceland Sea is the final region for production and modification of deep waters initially formed in the Arctic Ocean and Greenland Sea (Aagaard et al., 1985), prior to export into the North Atlantic Ocean (see Fig. 14 of "Introduction" chapter, this volume). Data from this region are needed to determine the evolution of these water masses. The area also is suited for studies of the chemical (stable-isotope) character of intermediate and deep waters through time. This will help our understanding of the initiation of North Atlantic Deep Water (NADW) and the evolution of global ocean circulation.

Site 907 (see Fig. 17 of "Introduction" chapter, this volume) is located on the Iceland Plateau, a shallow plateau defined by the 1800-m contour, which gently increases in depth away from the spreading axis, the Kolbeinsey Ridge (see Fig. 3 of "Introduction" chapter, this volume). The southeastern part of the plateau drops off into the Norway Basin; to the South the plateau shallows toward the Iceland shelf. The northern boundary of the plateau is defined by the western segment of the Jan Mayen Fracture Zone, a prominent escarpment-like feature separating the plateau from the deeper Greenland Basin.

An extinct, short-lived spreading axis between magnetic Anomalies 6C and 5D has been suggested to exist on the eastern Iceland Plateau before the present-day Kolbeinsey Ridge came into existence (see Fig. 4 of "Introduction" chapter) (Johnson et al., 1972; Talwani and Eldholm, 1977). According to Talwani and Eldholm (1977), the extinct spreading axis probably represented a period of adjustment associated with the major westward shift of spreading between Anomalies 7 and 5. Vogt et al. (1980), however, ruled out the intermediate axis and proposed that spreading from the Kolbeinsey Ridge was symmetrical since post-Anomaly 7 time. If we accept the intermediate axis interpretation, Site 907 has been drilled on Anomaly 6B crust, between 22 and 24 Ma. Using the Vogt et al. (1980) interpretation, Site 907 is on crust of Anomaly 5B age, between 14 and 15 Ma.

The Iceland Plateau is associated with an opaque, extremely smooth acoustic basement reflector (Fig. 1), with only short indistinct reflector elements observed below. In some places the opaque reflector is interrupted by peaks appearing to pierce the layer and originate from deeper levels. This led Eldholm and Windisch (1974) to suggest that real oceanic basement was buried beneath the opaque horizon. The opaque horizon is associated with a fairly low seismic velocity of 3.3 km/s (Myhre and Eldholm, 1981). Furthermore, the opaque horizon exhibits no obvious age-depth relationship as expected for young oceanic crust.

The sedimentary sequence in the area can be divided into two major units: the uppermost sequence is characterized by weak, continuous, flat-lying reflectors, and the lower sequence is almost transparent (Fig. 1). Site 348, Leg 38 (Talwani, Udintsev et al., 1976), is located to the South of Site 907 at the eastern side of the extinct axis on Anomaly 6A crust, about 22 Ma. At Site 348, 544.0 m was penetrated and spot-cored, with a pelagic Quaternary and Neogene sequence of 526.6 m on top of basalt. The K/Ar dating of the tholeiitic basalt provided an age of 18–19 Ma, and its texture varied from fine- to medium-grained without any pillow lavas observed. The basalt appeared to be part of a major sill or dike body that could be the opaque seismic layer, and deeper oceanic basement as well as masked sediment layers cannot be ruled out.

Objectives

The primary objective of Site 907 was to recover an undisturbed pelagic sedimentary sequence with a content of calcareous pelagic fossils that would make it possible to monitor the formation and variation of oceanic fronts moving back and forth across the Icelandic Plateau. The site was planned as a midpoint in an East-West regional transect in the southern part of the Norwegian-Greenland Sea, from the Greenland Margin across the Iceland Plateau and the Norway Basin to the Norwegian Margin. It also constitutes part of a bathymetric transect from the plateau into the Norway Basin. The site was expected to give an open-ocean record of IRD and carbonate, as it is isolated from local continental influence. The site location also was chosen to find higher concentrations of calcareous pelagic fossils than were obtained at the previous DSDP and ODP sites in the Norwegian-Greenland Sea.

The location of Site 907 also makes it possible to monitor the formation of northern-source deep waters through time, because the Ice-

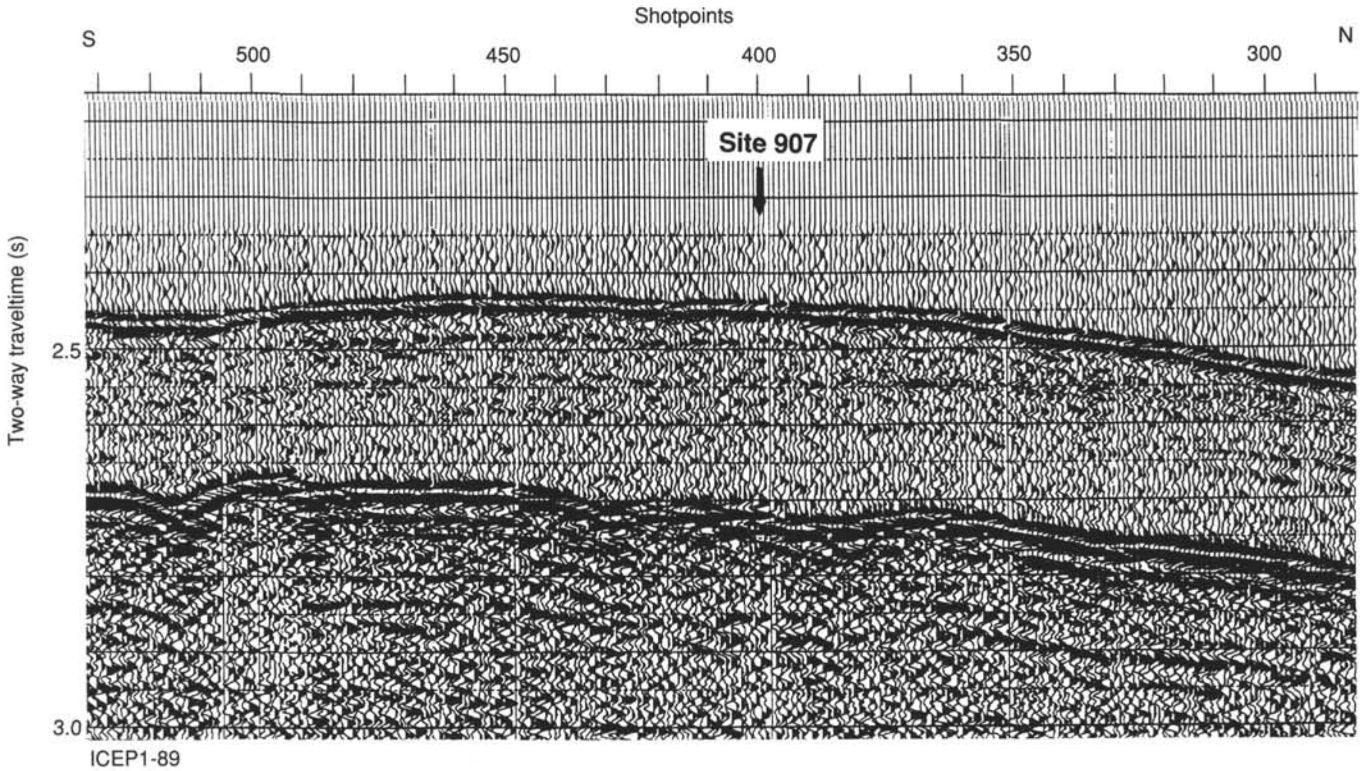

Figure 1. Seismic line ICEP 1-89, Segment A. Site 907 is located at shotpoint 400.

land Plateau is the final station for deep-water production and modification of deep waters formed in the Greenland Sea and Arctic Ocean before they are exported into the North Atlantic Ocean. The late Cenozoic histories of formation and chemistry of northern-source deep waters were to be described through studies of continuously cored sediment sections. The site is located on middle Miocene crust and is overlain by about 360 m of sediment, probably allowing high-resolution studies of the last 10–12 m.y. Piston cores document Pleistocene pelagic carbonate sequences with pronounced glacial-interglacial cycles and ash layers.

The strong reflector under the main sedimentary sequence at 0.28 s two-way traveltime (TWT) was to be drilled to determine if what appeared to be acoustic basement was the real volcanic basement. However, additional reflector segments at approximately 0.43 s TWT below the seafloor have been observed.

OPERATIONS

St. John's, Newfoundland, Port Call

Leg 151 officially began with the first mooring line ashore at Berth 17 in St. John's Harbor, Newfoundland, at 2015 hr (local time), 24 July 1993. On 25 July the crew change was completed and outgoing and incoming freight was handled. The pacing item at the Leg 151 port call was SEDCO's overhaul of the heave compensator and installation of a new electrical umbilical cord on the top drive. Lamont-Doherty Earth Observatory (LDEO) installed a new logging cable.

St. John's to Site 907

The last mooring line was away at 1319 hr, 29 July 1993. The ship transited the entrance to St. John's Harbor, and the sea voyage to ICEP-1 (Site 907) began at 1400 hr, 29 July. The clock was advanced 0.5 hr on 30 July from 0000 to 0030 hr, 1.0 hr on 2 August from 0000 to 0100 hr, and 1 hr on 5 August from 0000 to 0100 hr to put the ship on Universal Time Coordinated (UTC) for the rest of the leg. The 1755-nmi transit required 159.7 hr for an average speed of 11.0 kt.

The seismic survey at Site 907 started at 0932 hr, 5 August, and covered 21.9 nmi in 3.6 hr at an average speed of 6.1 kt. The seismic gear was retrieved, and a Datasonics 354B beacon was dropped at 1051 hr, 5 August, at 69°14.944′N, 12°41.949′W. The survey was continued past the beacon drop for 6.1 nmi in 1.0 hr at 6.1 kt.

The ship was on location at 1248 hr and the precision depth recorder (PDR) indicated a water depth of 1815.4 meters below rig floor (mbrf). Despite the temporary loss of the signal from the primary beacon, the ship was stabilized in dynamic positioning (DP) mode at 1315 hr. Another Datasonics 354B beacon was then dropped to be a backup beacon.

Hole 907A

An advanced hydraulic piston corer/extended core barrel (APC/XCB) drill bit was run. Because the PDR indicated a water depth of 1815.4 mbrf, Core 151-907A-1H was shot with the bit at 1809.4 m. The recovery was 7.27 m; therefore, the sediment surface depth was 1811.6 mbrf and 1800.8 meters below sea level (mbsl). The location of Hole 907A is 69°14.989′N, 12°41.894′W. Cores 907A-1H to -23H were taken from 0.0 to 216.3 mbsf, with 216.3 m cored and 224.1 m recovered (102.6% recovery) (Table 1). Overpull on the APC increased from 10,000 lb at 35.8 mbsf up to 65,000 lb at 187.8 mbsf. Cores were not oriented, and the Adara temperature shoe was run on Cores 907A-3H, -6H, -9H, and -12H. Negligible concentrations of biogenic methane (5 ppm) were encountered in headspace gas analyses.

Core 23H bounced when it hit a hard object at the end of its stroke and ended the APC section. Cores 907A-24X through -26X were taken from 216.3 to 224.1 mbsf in basalt, with 7.8 m cored and 4.88 m recovered (62.6% recovery). Coring with the XCB was terminated when two hard-formation TCI XCB shoes were destroyed.

Table 1. Coring summary, Hole 907A.

Core	Date (Aug. 1993)	Time (UTC)	Depth (mbsf)	Length cored (m)	Length recovered (m)	Recovery (%)
151-907A-						
1H	5	1940	0.0–7.3	7.3	7.27	99.6
2H	5	2015	7.3–16.8	9.5	9.81	103.0
3H	5	2115	16.8–26.3	9.5	9.89	104.0
4H	5	2145	26.3–35.8	9.5	9.88	104.0
5H	5	2220	35.8–45.3	9.5	10.10	106.3
6H	5	2315	45.3–54.8	9.5	10.06	105.9
7H	5	2350	54.8–64.3	9.5	9.90	104.0
8H	6	0030	64.3–73.8	9.5	9.82	103.0
9H	6	0130	73.8–83.3	9.5	10.19	107.2
10H	6	0205	83.3–92.8	9.5	9.92	104.0
11H	6	0240	92.8–102.3	9.5	10.07	106.0
12H	6	0335	102.3–111.8	9.5	9.97	105.0
13H	6	0405	111.8–121.3	9.5	10.00	105.2
14H	6	0435	121.3–130.8	9.5	9.93	104.0
15H	6	0535	130.8–140.3	9.5	9.70	102.0
16H	6	0605	140.3–149.8	9.5	9.92	104.0
17H	6	0640	149.8–159.3	9.5	10.01	105.3
18H	6	0715	159.3–168.8	9.5	9.87	104.0
19H	6	0750	168.8–178.3	9.5	9.99	105.0
20H	6	0825	178.3–187.8	9.5	9.85	103.0
21H	6	0900	187.8–197.3	9.5	9.59	101.0
22H	6	0935	197.3–206.8	9.5	9.58	101.0
23H	6	1015	206.8–216.3	9.5	9.78	103.0
24X	6	1305	216.3–217.3	1.0	0.53	53.0
25X	6	1610	217.3–221.0	3.7	2.41	65.1
26X	6	2100	221.0–224.1	3.1	1.94	62.6
Coring totals				224.1	229.98	102.6

The hole was prepared for logging by circulating the hole clean, making a conditioning trip to 63 mbsf, and going back to bottom. The bit was positioned at 82.8 mbsf for logging, with spacing to pick up to 63 mbsf to log the upper hole.

About 2.25 hr were lost when the first attempt to log was terminated because the old rope socket had two broken ground wires (it was rebuilt), and the second attempt to log was terminated when the head on the sonic tool failed a continuity test (it was replaced). The logs were run as follows:

Log No. 1: Dual induction/sonic; log to 198.4 mbsf in 3.75 hr.
Log No. 2: Neutron/density; log to 192.4 mbsf in 3.5 hr.
Log No. 3: FMS; log to 192.4 mbsf in 3.0 hr.
Log No. 4: GST; log to 189.3 mbsf in 2.75 hr.

The GST logging tool could not be pulled into the bit past the flapper valve, and attempts to clean out any obstructions by circulating and pumping 30 bbl high-viscosity mud pills were not successful. After 1.75 hr of work, the tool could not be pulled into the pipe enough to cause a pressure increase. The Kinley wireline crimping tool and cutter was dropped to cut the logging line in the bottom drill collar, and the line was retrieved. The drill string was retrieved without incident, and the bit and GST tool cleared the rotary table at 0400 hr, 8 August, ending Hole 907A. The GST tool and Americium radioactive source were recovered without damage. No clay or torpedo damage was found to explain the flapper valve problem; therefore, the flapper was probably tripped by the shoulder on the GST tool.

Emergency Medical Evacuation

On 7 August, Dr. Jim Hampton advised that a situation had developed that might require an emergency medical evacuation. Oscar Gabinay, SOS welder, experienced nausea and vomiting shortly after sailing from St. John's. He was hospitalized, but after observing the patient for 24 hr, Dr. Hampton advised at 0600 hr, 8 August, that, although the patient's condition was stabilized for a few days, he felt the patient should be evacuated. The beacons were pulled immediately and preparations made for the sea voyage. Iceland Coast Guard recommended that the best medical evacuation point was Northwest Iceland. The U.S. Air Force base at Keflavik was contacted, and they sent two helicopters and a fixed-wing aircraft to the rendezvous point at 1448 hr, 8 August, with an ETA at the Reykjavik hospital of 1710 hr.

After the evacuation, we decided to bypass Site 907, proceed directly to the Fram Strait, and core in ice-free water at proposed Site FRAM-2 (Site 908) until the ice-breaker *Fennica* arrived, then go immediately to the Yermak Plateau sites.

LITHOSTRATIGRAPHY

Introduction

The sediments recovered at Site 907 are dominated by unlithified silty clay and clayey silt, dark grayish brown in the upper half of the hole and olive gray, greenish gray, and grayish green in the lower half. Thin black, olive, and green bands are present and may be diagenetic in origin. Bioturbation is light to heavy throughout, in general obscuring distinct color banding and possibly lithologic boundaries. Five lithologic units were identified, primarily on the basis of varying amounts of biogenic and siliciclastic material, and volcanic glass (Fig. 2; Table 2). Most of the lithologic boundaries are gradational, as the different components that were used to define the boundaries change at different depths. Dropstones >1.0 cm, although never abundant, are present from the top of the hole through Section 151-907A-13H-4 (118 mbsf).

Volcanic ash layers, <1 cm to 15 cm in thickness, are present from the top through 184 mbsf (Section 151-907A-20H-4/5). Below this, ash pods are present down to 197 mbsf (Core 21H). Although an important lithologic component (Fig. 3), the ashes are not a major factor in distinguishing lithologic units and are discussed separately at the end of this section.

Description of Lithologic Units

Lithologic Unit I:

Sections 151-907A-1H-1, 0 cm, through 151-907A-2H-CC, 31 cm (0–16.8 mbsf)
Thickness: 16.8 m
Age: Quaternary

Lithologic Unit I is distinguished by the presence of biogenic calcareous material, primarily foraminifers. It is dominated by clayey silt, silty clay, and foraminifer-bearing silty mud with minor amounts of biosilica-bearing silty carbonate ooze, clayey foraminifer ooze, silty mud, foraminifer-bearing clay, foraminifer silty clay, and ash. The most pervasive colors are dark grayish brown and dark brown, but thinner intervals of olive brown, grayish brown, gray, olive, and olive gray are present. With the exception of the ash layers, all of the color boundaries are gradational. This is attributed to pervasive bioturbation. The subtle color changes do not directly correlate with changes in $CaCO_3$ percentage, which show more variation over shorter intervals than does the color.

In addition to the biogenic component, the coarse fraction consists of quartz, feldspar, and mica, with little volcanic glass.

Dropstones >1 cm are rare. The two identified in Section 2H-3, 50 cm (10.8 mbsf), and Section 2H-6, 125 cm (16.03 mbsf), are both basaltic (Table 3). Mud clasts were recovered in the upper 50 cm of Core 2H and are probably caused by drilling disturbance.

Three distinct ash layers, 10 to 18 cm thick, are present (Table 4; Fig. 3). All three have sharp bases, are graded, and have gradational contacts with the overlying lithology.

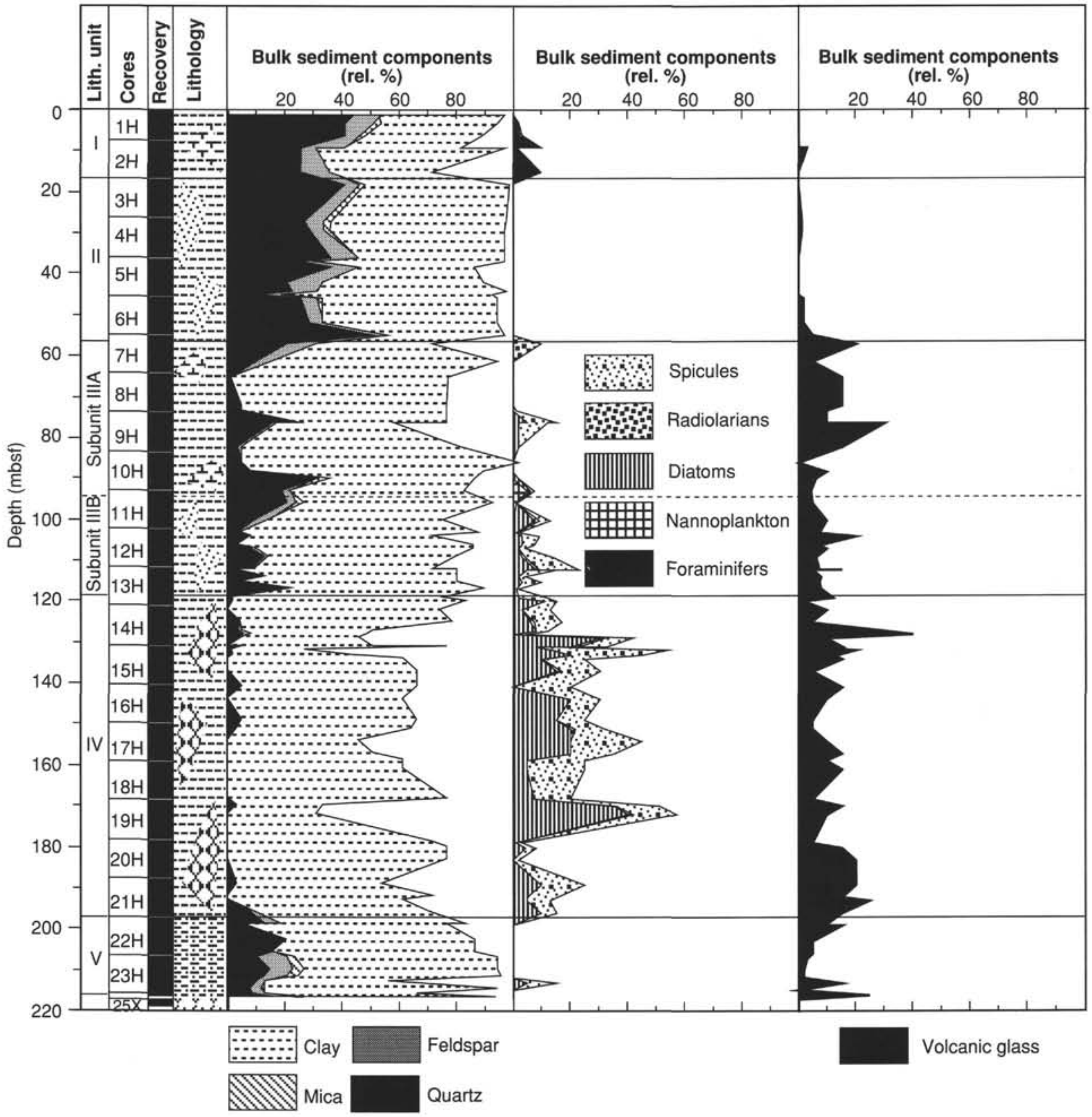

Figure 2. Graphic summary of lithologic units for Hole 907A, and percentages of the three components used to define the lithologic units: dominant siliciclastic components, biogenic content, and volcanic glass.

Lithologic Unit II:

Sections 151-907A-3H-1, 0 cm, through 151-907A-7H-1, 150 cm (16.8–56.3 mbsf)
Thickness: 39.5 m
Age: Pliocene to Quaternary

Lithologic Unit II is predominantly clayey silt and silty clay, characterized by the absence of biogenic carbonate and silica and the abundance of silt- and sand-sized siliciclastic grains.

Clayey silt and silty clay compose more than 90% of the unit and are primarily dark grayish brown, dark gray, and gray. These lithologies are commonly massive but show faint mottling as a result of bioturbation in Cores 4H and 5H, and laminae of dark grayish brown, dark olive, and olive in Cores 3H through 5H. Dark greenish gray beds in Core 6H, up to 60 cm in thickness, are more indurated. A centimeter-sized concretion is present in Section 6H-6, 60 cm (53.4 mbsf). Small dropstones (<1 cm in size) are present throughout the unit (Fig. 4), and large dropstones are rare, with five observed (Table 3).

The dominant components in the clayey silt and silty clay are, in order of decreasing abundance: clay (5% to 90%), quartz (5% to 40%), feldspar (5% to 35%), mica (<5%), and accessory minerals (<5%). Volcanic glass is rare but shows a slight increase toward the base of the unit. Carbonate percentages seldom exceed 1%.

Four minor lithologies are present in Unit II: (1) grayish olive clay; (2) dark gray and dark grayish brown ash (see the following section); (3) dark gray diatom- and ash-bearing silty clay; and (4) gray-

Table 2. Summary of lithologic units, Site 907.

Unit	Dominant lithologies	Interval, mbsf (thickness, m)	Age	Occurrence (core-section)
I	Interbedded silty clay, clayey silt, and foraminifer-bearing silty mud and silty clay.	0–16.8 (16.8)	Quaternary	1H-1 to 2H-CC, 31 cm
II	Silty clay and clayey silt. Defined by the absence of biogenic sediments.	16.8–56.3 (39.5)	Pliocene to Quaternary	3H-1 to 7H-1, 150 cm
IIIA	Interbedded silty clay and clayey silt with thin nannofossil ooze beds. Minor biogenic silica, decrease in % quartz.	56.3–94.1 (37.8)	late Miocene to Pliocene	7H-2, 0 cm, to 11H-2, 30 cm
IIIB	Silty clay and clayey silt, some biogenic silica, no calcareous nannofossils.	94.1–118.1 (24.0)	late Miocene	11H-2, 30 cm, to 13H-6, 30 cm
IV	Biosilica-bearing silty clay and clayey silt. No dropstones, very little quartz.	118.1–197.3 (79.2)	middle to late Miocene	13H-6, 30 cm, to 22H-1, 0 cm
V	Clayey mud and silty clay. Decrease in biosilica, increase in quartz.	197.3–216.3 (19.0)	middle Miocene	22H-1, 0 cm, to 24-1, 0 cm

ish brown carbonate mud. Clay appears to be restricted to Section 4H-1, 0–30 cm (26.3 to 26.6 mbsf), and includes quartz, feldspars, and opaques as accessory grains. Diatom- and ash-bearing silty clay was observed in Section 6H-2, 72–100 cm (28.52 to 28.8 mbsf), overlying one of the indurated greenish gray layers. Carbonate mud is present in Sections 5H-CC, 5–14 cm, and 6H-1, 45–55 cm (Fig. 5). Sediment in 5H-CC is disturbed, but the bed in Section 6H-1 has a sharp upper contact and a gradational lower contact. The carbonate mud consists of well-sorted, very fine silt- to clay-sized, rounded particles of carbonate with minor amounts of quartz. There is no evidence for a biogenic origin; hence, the sediment is referred to as detrital.

Lithologic Unit III: .

Sections 151-907A-7H-2, 0 cm, through 151-907A-13H-6, 30 cm (56.3–118.1 mbsf)
Thickness: 61.8 m
Age: late Miocene to Pliocene

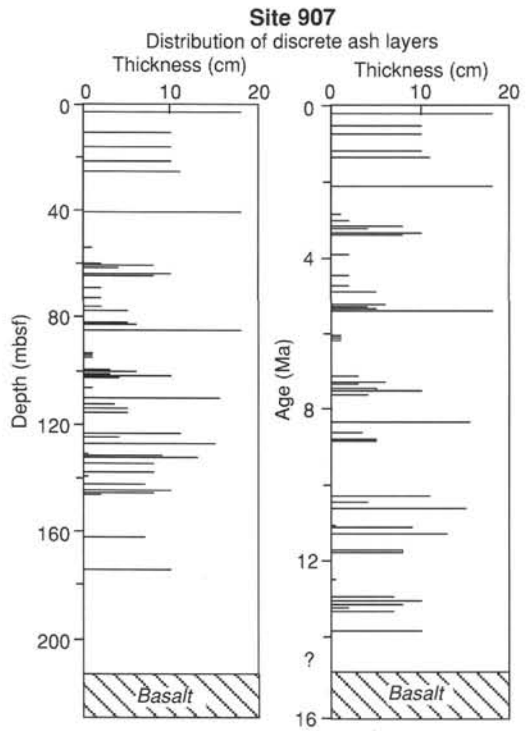

Figure 3. Graphic summary of ash layers >1 cm thick vs. depth in the core and age.

Lithologic Unit III is defined by the presence of biogenic silica, an increase in volcanic glass content, and a decrease in the percentage of quartz and feldspar. Clayey silt and silty clay compose about 40% of the unit and are primarily dark olive gray, olive gray, and very dark gray. In minor intervals the silty clay is dark greenish gray, olive, and gray. The dominant silt- and sand-sized components are, in increasing order: mica, accessory minerals, feldspar, and quartz. Dark gray, olive gray, and dark greenish gray, ash-bearing silty clay composes about 30% of the unit. In addition to volcanic glass, the coarse fraction consists of quartz, feldspar, mica, and accessory minerals. Clay beds, primarily dark gray, are present in up to 1.5-m-thick layers. Six dropstones >1 cm in diameter are present. With the exception of ash layers, all lithologies and color boundaries are gradational as a result of pervasive bioturbation. Ash layers are common (Table 4, Fig. 3), and in general have sharp bottom contacts and, in some layers, sharp upper contacts (Fig. 6). Two subunits are defined: Subunit IIIA has interbedded nannofossil ooze and nannofossil silty clay; Subunit IIIB does not.

Subunit IIIA:

Sections 151-907A-7H-2, 0 cm, through 11H-2, 30 cm (56.3–94.1 mbsf)
Thickness: 37.8 m
Age: late Miocene to Pliocene

Five layers of nannofossil ooze and one layer of nannofossil silty clay, 2 to 53 cm thick, are present. Outside of the thin Holocene layer at the top of Core 1H, these are the only nannofossil-rich layers at this site

The layers are present as follows:

Table 3. Dropstones >1 cm in diameter.

Core, section, interval (cm)	Depth (mbsf)	Diameter (cm)	Lithology
151-907A-			
2H-3, 50	10.8	5.0	basalt
2H-6, 125	16.0	6.0	basalt
4H-1, 41	26.71	1.0	—
4H-6, 49	34.29	2.0	—
4H-6, 99	34.79	6.0	gneiss
6H-2, 21	47.01	1.0	siltstone
6H-6, 0	52.80	3.0	—
7H-2, 36	56.66	4.0	quartzite
8H-6, 55	72.35	1.0	basalt
11H-1, 112	93.92	1.5	sandstone
11H-1, 141	94.21	1.0	—
11H-3, 140	97.20	5.5	—
13H-4, 21	116.5	1.0	quartz gneiss
13H-4, 62	116.9	3.5	metal piece contaminant

Note: — = lithology not determined.

Table 4. Summary of ash layers >1 cm thick.

Core, section, interval (cm)	Depth (mbsf)	Thickness (cm)	Color	Munsell color code Hue	V	C
151-907A-						
1H-3, 56–74	3.56–3.74	18.0	Very dark gray	3Y	3.0/	2
2H-3, 90–100	11.20–11.30	10.0	Gray	5Y	4.0/	1
2H-6, 130–140	16.10–16.20	10.0	Black	5Y	2.5/	2
3H-4, 45–55	21.75–21.85	10.0	Dark grayish brown	3Y	4.0/	2
3H-6, 110–121	25.40–25.51	11.0	Grayish olive	10Y	4.0/	2
5H-4, 31–49	40.61–40.79	18.0	Very dark gray	3Y	3.0/	0
6H-6, 107–108	53.87–53.88	1.0	Dark gray	10YR	4.0/	1
7H-4, 85–87	60.15–60.17	2.0	Dark gray	5Y	4.0/	1
7H-5, 15–23	60.95–61.03	8.0	Black-brown	5Y	2.5/	1
7H-5, 89–93	61.69–61.73	4.0	Black	5Y	2.5/	1
7H-6, 120–120	63.50–63.50	<1	Black	5Y	2.5/	1
7H-6, 130–140	63.60–63.70	10.0	Grayish brown	3Y	5.0/	2
8H-1, 0–8	64.30–64.38	8.0	Gray	10YR	5.0/	1
8H-4, 40–42	69.20–69.22	2.0	Black	5Y	3.0/	1
8H-6, 120–122	73.00–73.02	2.0	Black	5Y	3.0/	1
9H-2, 37–39	75.67–75.69	2.0	Dark gray ?			
9H-3, 31–36	77.11–77.16	5.0	Dark gray ?			
9H-6, 63–68	81.93–81.98	5.0	Dark gray ?			
9H-6, 100–104	82.30–82.34	4.0				
9H-6, 114–120	82.44–82.50	6.0	Gray	5Y	5.0/	1
10H-1, 145–150	84.75–84.80					
10H-2, 0–13	84.80–84.93	18.0	Black	5Y	2.5/	1
11H-1, 70–71	93.50–93.51	1.0	Grayish olive	10Y	4.0/	2
11H-1, 74–75	93.54–93.55	1.0	Very dark gray	5Y	3.0/	1
11H-1, 134–135	94.14–94.15	1.0	Gray	5Y	4.0/	1
11H-5, 103–106	99.83–99.86	3.0	Gray	5Y	4.0/	1
11H-6, 30–36	100.60–100.66	6.0	Pale olive	10Y	6.0/	2
11H-6, 50–53	100.80–100.83	3.0	Very dark gray	5Y	3.0/	1
11H-6, 129–134	101.59–101.64	5.0	Very dark gray	5Y	3.0/	1
11H-7, 21–31	102.01–102.11	10.0	Gray	5Y	4.0/	1
12H-1, 48–52	102.78–102.82	4.0	Black	N	2.0/	0
12H-3, 123–124	106.53–106.54	1.0	Dark grayish brown	10YR	4.0/	2
12H-6, 24–39.5	110.04–110.20	15.5	Gray	5Y	5.0/	1
13H-1, 68–71.5	112.48–112.52	3.5	Black	5Y	2.5/	1
13H-2, 97–102	114.27–114.32	5.0	Gray	10YR	5.0/	1
13H-3, 105–110	115.85–115.90	5.0	Dark greenish gray	5GY	4.0/	1
14H-2, 25–36	123.05–123.16	11.0	Dark gray-gray			
14H-3, 79–83	125.09–125.13	4.0	Dark gray-gray			
14H-4, 130–145	127.10–127.25	15.0	Dark gray	N	4.0/	0
15H-1, 18–18.5	130.98–130.99	0.5				
15H-1, 64–73	131.44–131.53	9.0				
15H-2, 18–31	132.48–132.61	13.0	Dark greenish gray	5G	4.0/	1
15H-3, 128–136	135.08–135.16	8.0				
15H-5, 93–101	137.73–137.81	8.0	Very dark gray	5Y	3.0/	1
15H-6, 97–97	139.27–139.27	<1	Black ?			
16H-2, 62–69	142.42–142.49	7.0	Dark gray-black	5Y	3.0/	1
16H-4, 10–20	144.90–145.00	10.0	Grayish green	5G	4.0/	2
16H-4, 75–83	145.55–145.63	8.0	Grayish green	5G	4.0/	2
16H-4, 95–97	145.75–145.77	2.0	Grayish green	5G	4.0/	2
18H-2, 143–150	162.23–162.30	7.0	Grayish green	5G	4.0/	2
20H-4, 148–150	184.28–184.30					
20H-5, 0–8	184.30–184.38	10.0	Gray	5Y	5.0/	1

Notes: V = value. C = chroma.

1. nannofossil ooze, gray—7H-3, 43–62 cm (58.23–58.42 mbsf);
2. biosilica- and ash-bearing nannofossil ooze, gray—7H-3, 121–123, (59.01–59.03 mbsf);
3. biosilica- and ash-bearing nannofossil ooze, gray—7H-3, 126–128 cm (59.06–59.08 mbsf);
4. biosilica- and ash-bearing nannofossil ooze, gray—7H-6, 97–150 cm (63.27–63.80 mbsf);
5. biosilica-bearing nannofossil ooze, light gray—7H-7, 42 cm, to 8H-1, 50 cm (64.22–64.5 mbsf);
6. silica-bearing nannofossil silty clay, gray—11H-2, 0–27 cm (94.30–94.57 mbsf, Fig. 7).

Thus the first five layers are between 56 and 65 mbsf. Of these layers, only the topmost layer is a pure nannofossil ooze. All of the others contain 10% to 25% biosilica, and the middle three also contain between 10% and 25% ash. Below this interval are 29 m barren of carbonate, with a single additional carbonate-rich layer at 94 mbsf. This layer, however, only has 26% nannofossils and is a biosilica-bearing nannofossil silty clay.

Other minor lithologies are present. A dark gray to gray, biosilica- and ash-bearing silty clay is present in Section 7H-2, 0 cm, through 7H-3, 43 cm (56.30–58.23 mbsf), and a dark olive gray to dark gray, ash- and biosilica-bearing silty clay is present in Section 9H-1, 125 cm, through 9H-3, 140 cm (75.05–78.2 mbsf).

Subunit IIIB:

Sections 11H-2, 30 cm, through 13H-6, 30 cm (94.1–118.1 mbsf)
Thickness: 24.0 m
Age: late Miocene

Subunit IIIB lacks biogenic carbonate and has a higher biosilica content than does Subunit IIIA. Three minor lithologies were observed in this subunit. Biosilica-bearing silty clay is present in several intervals throughout the subunit. The color is primarily dark gray or different shades of greenish gray. Quartz and feldspar are present in minor amounts. A greenish gray to dark gray ash-bearing silty mud is present in Section 12H-2, 0–150 cm. A dark gray to greenish gray

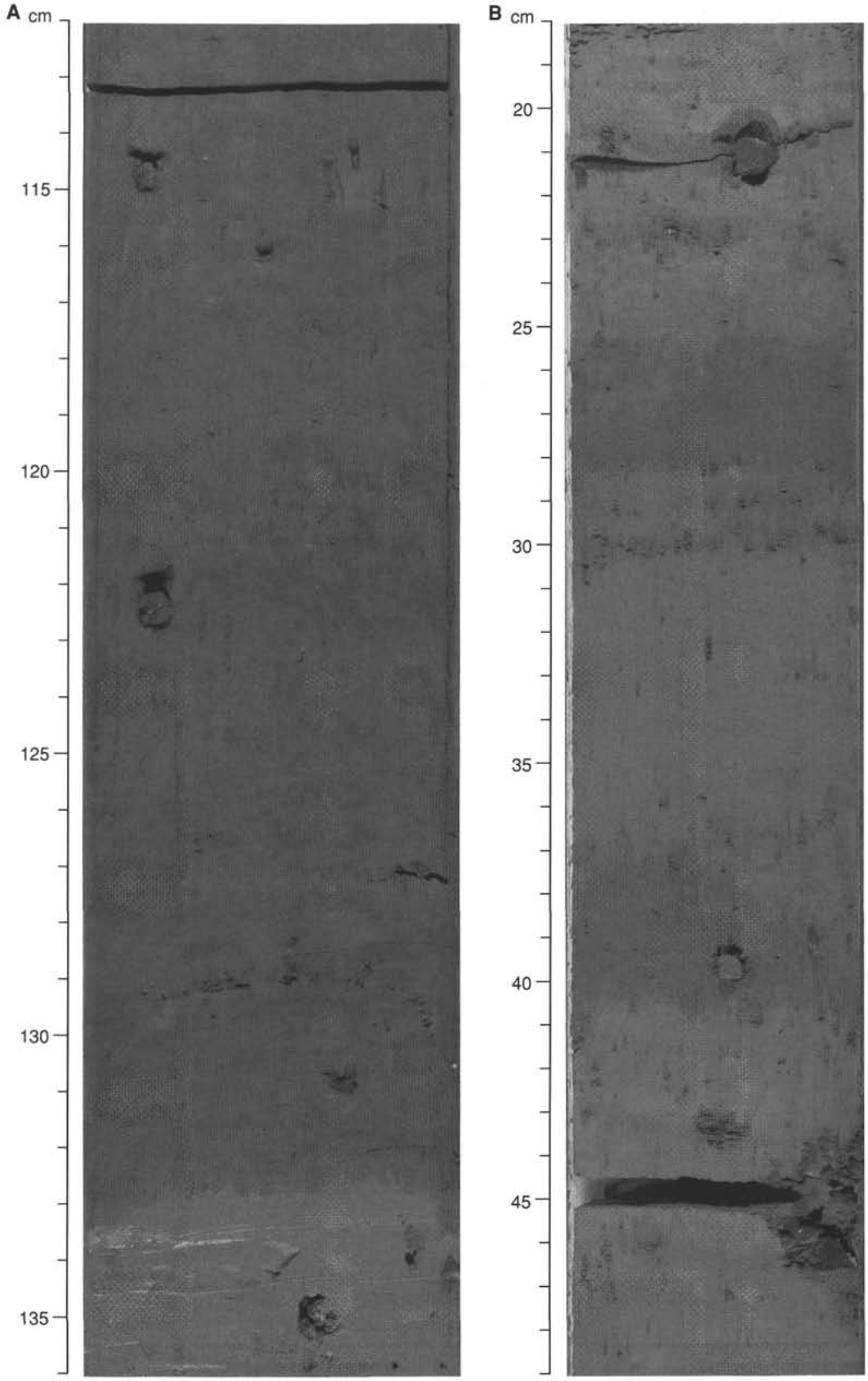

Figure 4. Small dropstones are present in both dark and light variations in sediment color. **A.** Lithologic Unit I, interval 151-907A-1H-4, 112–136 cm, brown and dark brown silty clay and clayey silt. **B.** Interval 151-907A-6H-2, 18–49 cm, gray and dark gray silty clay and clayey silt.

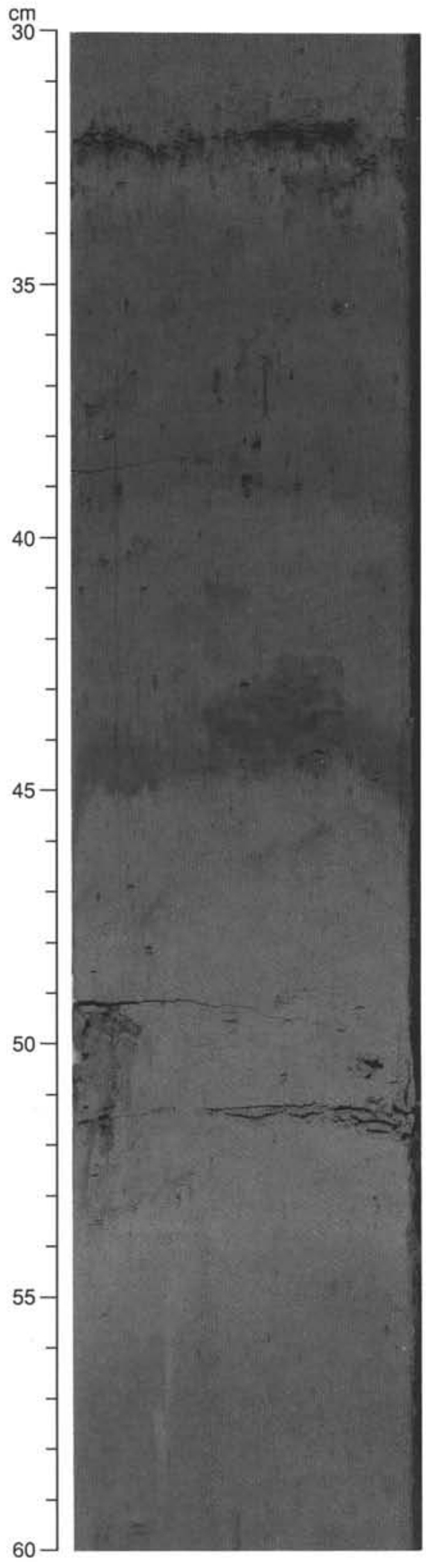

Figure 5. Interval 151-907A-6H-1, 30–60 cm. Carbonate mud (45–55 cm), interbedded with silty clay and clayey silt. Note the gradational lower contact and sharp upper contact. Coarser-grained sediment, indicative of IRD is present in both the gray and dark gray layers, and a thin, coarser layer is present at 32 cm.

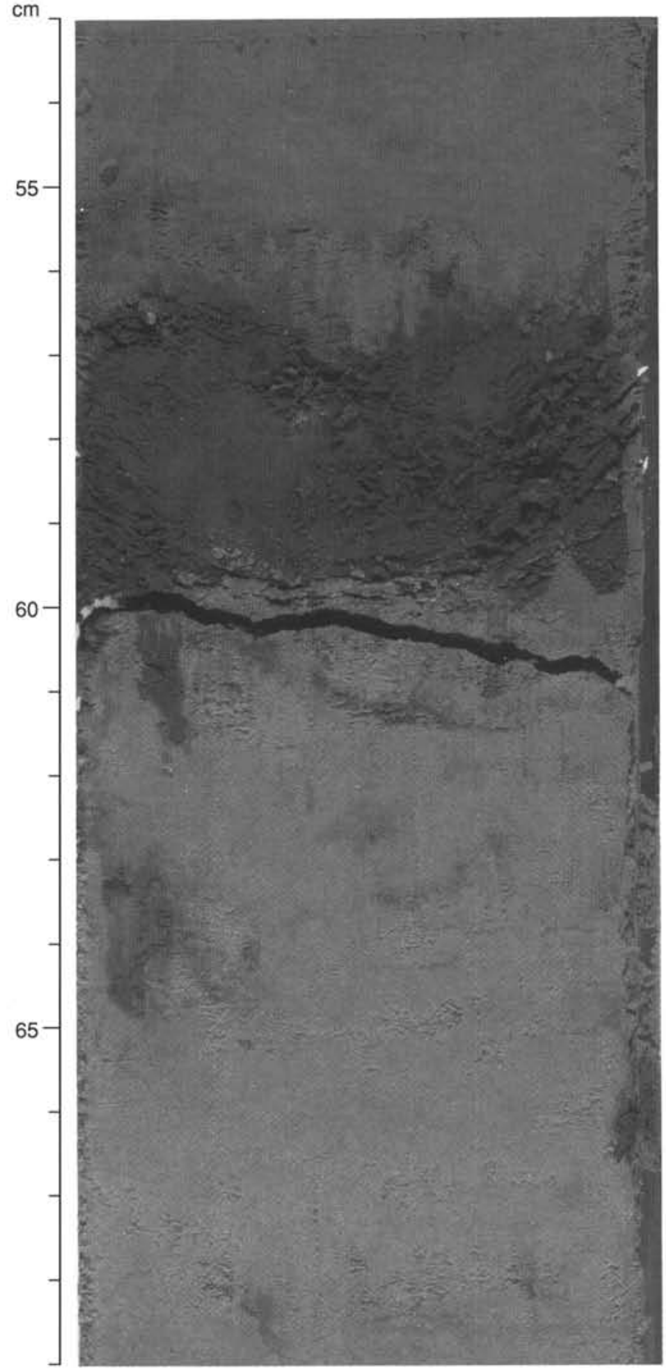

Figure 6. Interval 151-907A-11H-6, 53–69 cm. Dark ash layer in lithologic Unit III, with sharp upper and lower contacts. Bioturbators have displaced some of the ash, particularly at the base of the layer.

layer composed of ash- and biosilica-bearing clay was observed in Section 13H-5, 50 cm, through Section 13H-6, 30 cm.

Lithologic Unit IV:

Sections 151-907A-13H-6, 30 cm, through 22H-1, 0 cm (118.1–197.3 mbsf)
Thickness: 79.2 m
Age: middle to late Miocene

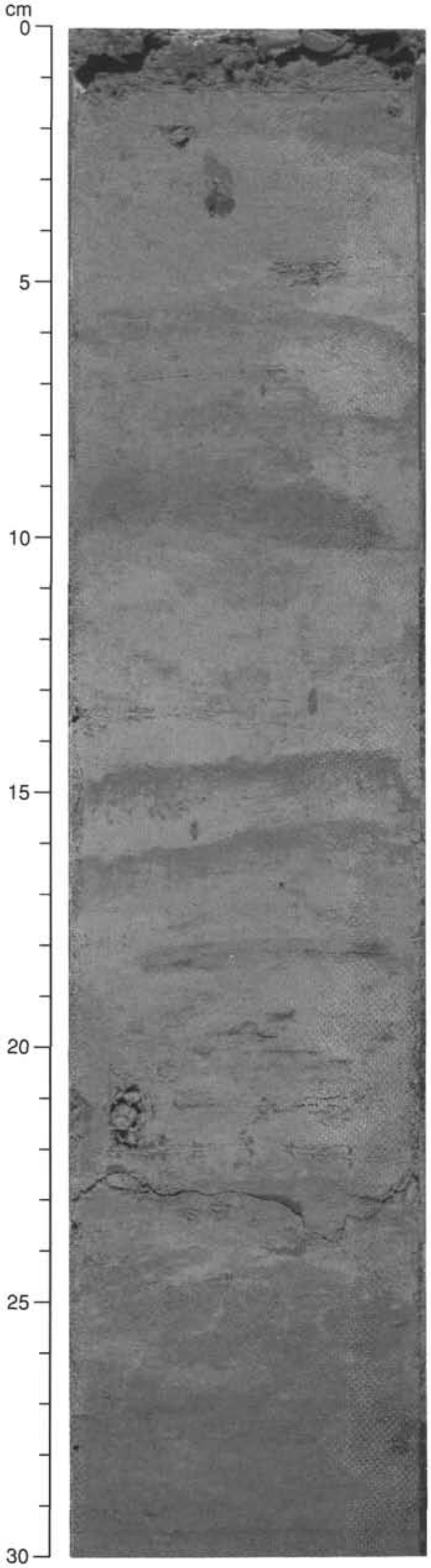

Figure 7. Interval 151-907A-11H-2, 0–30 cm (94.30–94.60 mbsf). Silica-bearing nannofossil silty clay at the base of lithologic Subunit IIIA. Many discrete burrows, including *Zoophycos*, can be seen in the high carbonate interval.

Lithologic Unit IV is defined by relatively high biosilica (~10%–35%) and volcanic glass contents (10%–15%), and low quartz content (<5%), and by the absence of dropstones. The major lithologies are ash- and biosilica-bearing silty clay and clayey silt, dark greenish gray to dark gray. Greenish gray color bands are found throughout the unit. With the exception of the ash layers (e.g., Fig. 8), all of the color boundaries are gradational, attributed to bioturbation. Moderate to heavy bioturbation is present throughout, giving a mottled appearance to the sediments. Green to gray and black burrows are common (Fig. 9A), some containing abundant volcanic glass shards.

Abundant ash layers ranging in thickness from 1 to 15 cm are common in the upper portion of the unit from 118.1 to 146 mbsf, averaging nearly one per section (Table 4, Fig. 3). The thicker layers are commonly graded (Fig. 8). Below 146 mbsf and toward the base of the unit, ash pods become common (Fig. 9B), and at least some are attributed to bioturbation of former ash layers.

Lithologic Unit V:

Sections 151-907A-22H-1, 0 cm, through 23H-CC (197.3–216.3 mbsf)
Thickness: 19.0 m
Age: middle Miocene

Lithologic Unit V is distinguished from Unit IV by higher quartz (10%–15%) and clay (80%–90%) contents and lower biosilica (<5%). Volcanic glass content is low compared with that in Units III and IV.

The major lithologies in Unit V are relatively homogeneous dark-olive-gray clayey mud and silty clay. Mottling and color changes in Core 23H are gradational and attributed to moderate to extensive bioturbation. Burrows are commonly filled with sand-sized volcanic glass.

No discrete ash layers are observed, although volcanic glass abundances range from 5% to 15% in the major lithologies. Zeolitic silty mud is present in Section 23H-2, 25 cm, and zeolites are also a minor component in Section 23H-6, 25 cm. A pyrite concretion and a pyrite burrow were observed in Sections 22H-2 and -6, respectively.

Interpretation

The lithostratigraphy at Site 907 reflects changes in oceanographic, climatic, and tectonic conditions, which strongly influenced sediment production, transport, and preservation. Our interpretations are based primarily on abundance and compositional changes in the siliciclastic and biogenic components.

Lithologic Unit V is a fine-grained siliciclastic unit, composed of clayey mud and silty clay, with 10%–20% quartz and little or no biogenic component. The origin of the coarse siliciclastic fraction (quartz, feldspar, mica) and its method of transport is not known. Possible modes of transport include ice-rafting, sediment-gravity flows such as turbidity currents, and aeolian transport. Ice-rafting is not likely, as the nearby land masses were not thought to be glaciated at this time. No sedimentary structures were observed that would support the turbidite interpretation, but detecting such structures in these moderately to heavily bioturbated, fine-grained sediments may require x-radiographs. Aeolian transport of sediment as coarse as fine sand is possible (Shaw et al, 1974) and has been documented (Folger, 1970). Because the coarse fraction falls within this size range, it may have been blown in from nearby ice-free land masses. In any case, the absence of a comparable siliciclastic component in the overlying unit suggests that these transport mechanisms were not operating during the deposition of Unit IV.

Unit IV contains very little quartz, feldspar, and mica. Biosilica is a major component, 10%–50% of the sediment. Based on the relatively high biogenic content, these sediments are interpreted as hemipelagic to pelagic in origin. The dominance of biosiliceous components suggests a high productivity interval. Nutrient-rich deep

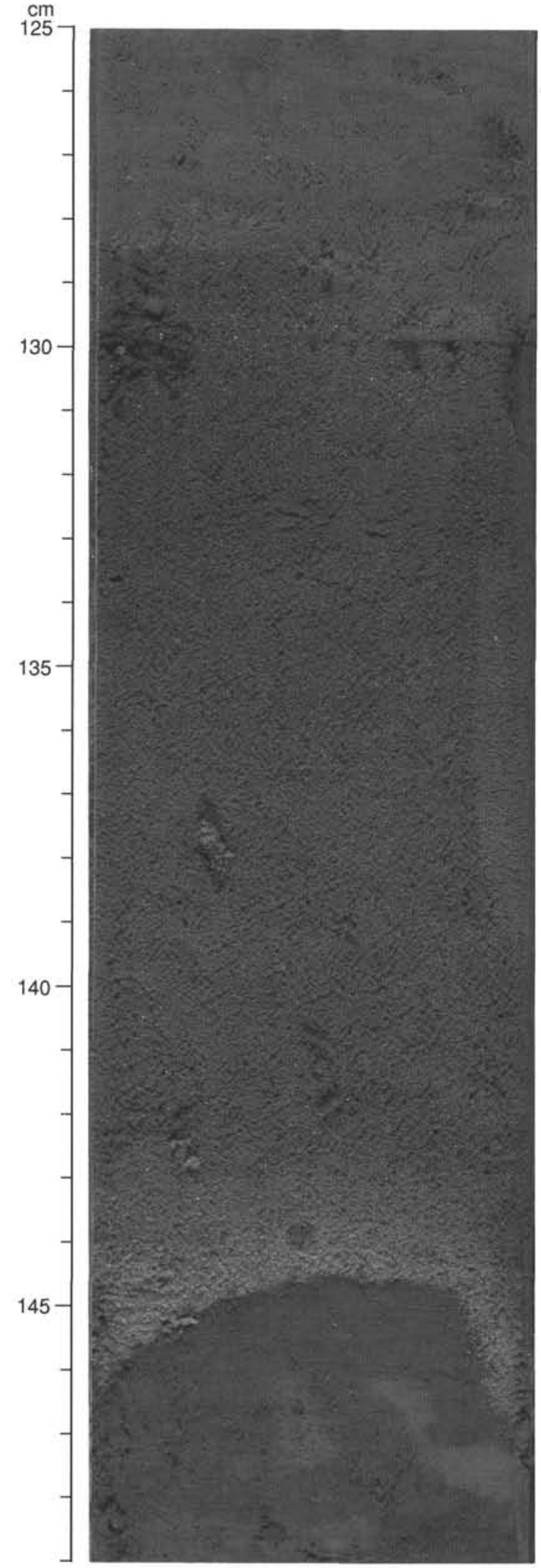

Figure 8. Interval 151-907A-14H-4, 125–149 cm. Graded ash layer with sharp base in lithologic Unit IV. Evidence of bioturbation is found below the base and at the top of the layer.

waters, correspondingly enriched in CO_2, may partially explain the lack of biogenic carbonate through dissolution. High rates of biosiliceous sedimentation may also have diluted biogenic carbonate deposition. Magnetostratigraphic data supports the inference of high sedimentation rates in the deposition of the lower two-thirds of this unit.

The boundary between Units IV and III is defined by an increase in quartz and is accompanied by the first appearance of dropstones (>1 cm) at 116 mbsf, both of which we interpret to be ice-rafted. This change, however, is the last in a series of steps that distinguish these two units. The decrease in sedimentation rate at about 135 mbsf is also within an interval that includes a hiatus (11–13 Ma). Biogenic silica decreases at approximately 128 mbsf (10.5 Ma) and is followed by dropstones and ice-rafted debris (IRD) about 12 m higher, approximately 9 Ma. This relation suggests that these trends were not closely linked, and that inferred expansion of sea ice associated with increased glaciation was not the primary cause of decreased biosilica contents. Lower biosilica contents may have resulted from decreased productivity because of lower upwelling rates and/or increased dissolution of biosilica related to greater ventilation of intermediate waters.

Unit III represents a transitional phase between Unit IV sediments (marked by high biosilica and low siliciclastic contents) and Unit II sediments (marked by low to absent biosilica and high siliciclastic contents). Thus the decrease in biogenic silica, begun in Unit IV, continues into Unit III (Fig. 2).

Unit IIIA contains the only layers of non-Holocene nannofossil ooze and nannofossil silty clay that were recovered at this site, and these layers are the criteria for distinguishing two subunits (Fig. 7). The first bed containing nannofossils is at 94.57 mbsf (~6.4 Ma), followed by a group of beds between 64.80 and 58.23 mbsf (~3.2 Ma). In this group, five nannofossil ooze layers were deposited in less than 0.3 m.y. All but the topmost of these layers also contain between 10% and 25% biosilica, and the top layer contains about 6% biosilica, indicating high productivity as well as high carbonate production and preservation. Biosilica-bearing layers are present in at least two other intervals in this unit, 56.30–58.23 and 75.05–78.20 mbsf, indicating reversion to high productivity conditions.

The close spacing and distinctiveness of the silica-bearing nannofossil layers suggest major and probably rapid changes in the overlying oceanographic fronts at the end of the Miocene and in the early Pliocene. These nannofossil layers may represent intervals of amplified response of the Norwegian-Greenland Sea to Northern Hemisphere climate change because of the incursion of warm North Atlantic surface waters. However, it is perhaps significant that there were no foraminiferal carbonate oozes deposited during the global warmth of the late Miocene and early Pliocene, in contrast to that of the late Quaternary as seen in Unit I.

Unit II is interpreted to represent the upper Pliocene and the bulk of the Quaternary. The dropstones, high quartz and feldspar content, and consistently dark color all indicate a glacial regime, beginning as early as 3 Ma. The lack of microfossils in general may be attributed to three causes: low productivity, preferential removal by dissolution or bottom currents, and/or dilution by siliciclastic material; however, this last explanation is insufficient to explain the unit's essentially barren sediments with no large attendant changes in sedimentation rate from the fossiliferous sediments above and below. Calcite dissolution may explain the near lack of carbonate in the pre-Brunhes period, as documented at Sites 642 and 643 (Henrich, 1989). In that study, preservation was unrelated to water depth. Dissolution may have been driven by diagenesis rather than water column chemistry, unless deep and intermediate waters were corrosive to calcite. No evidence exists for increased biosilica dissolution during this interval. Another possibility is decreased surface productivity. Productivity may have been negatively affected by oceanographic changes associated with increased glaciation. These include expanded sea-ice cover,

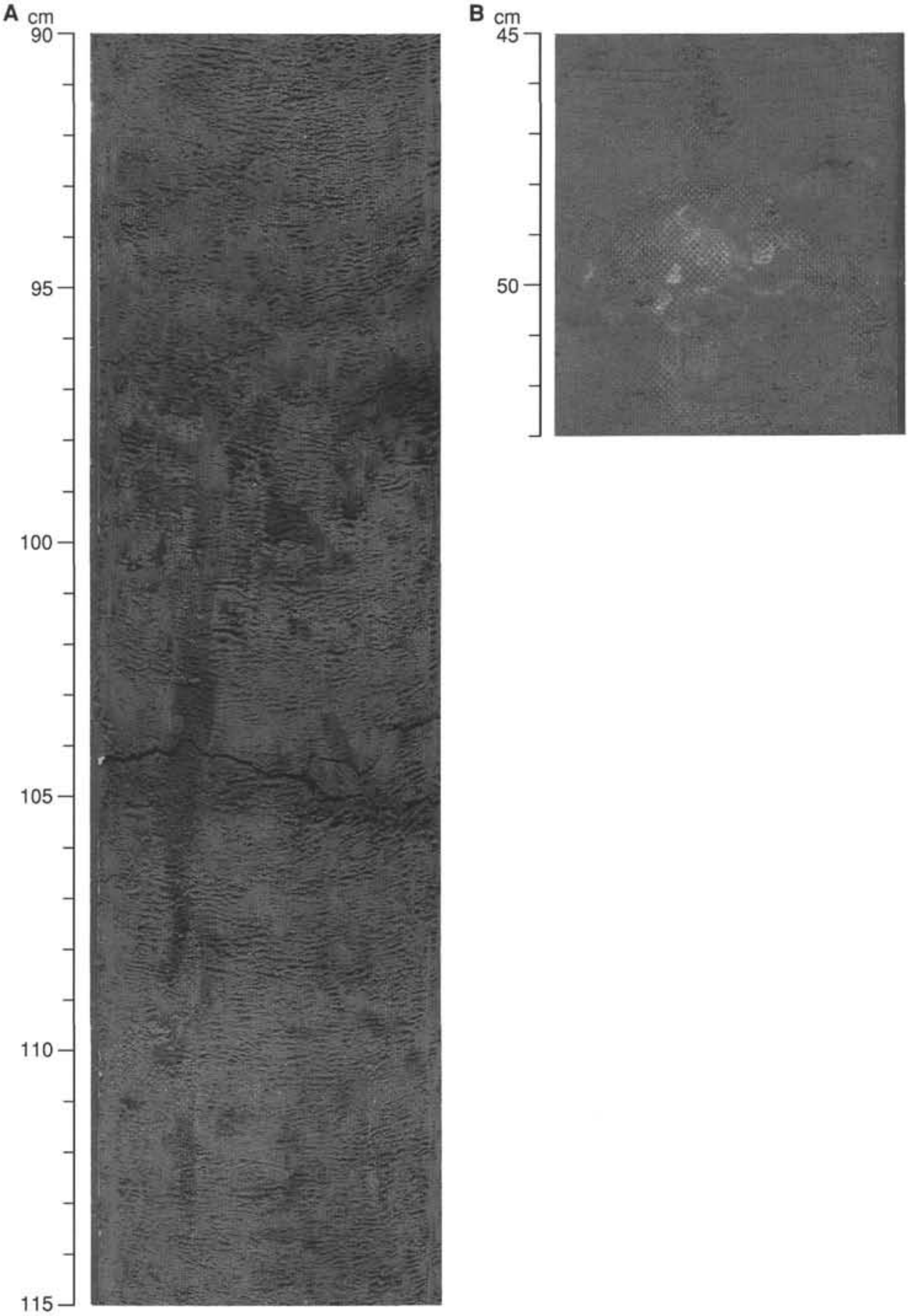

Figure 9. Bioturbation of ash layers. **A.** Interval 151-907A-15H-6, 90–115 cm. Thin ash layer at 97 cm may have been displaced by bioturbators. **B.** Interval 151-907A-20H-4, 45–53 cm. Ash pods may be all that remain of an ash layer.

cooler surface temperatures, increased stratification of the water column, and decreased upwelling of nutrients supplied to surface waters. A sharp increase in quartz and feldspar grains as well as greater dropstone abundance supports the suggestion that glaciation increased during the time represented by Unit II.

Unit I is interpreted to be the record of the last 0.8 m.y. of the Quaternary, slightly longer than the duration of the Brunhes normal magnetic polarity chron. High siliciclastic contents (including IRD) and dark-colored sediments characterize this unit, reflecting primarily glacial conditions. The uppermost 23 cm of Core 1H, rich in calcareous microfossils, may represent the Holocene interglacial. The underlying 16.6 m of dominantly glacial sediments are interrupted by episodic deposition of carbonate-rich layers, including a prominent foraminifer-rich layer in Section 1H-5, 45–80 cm.

The alternating fossiliferous and fossil-poor sediment, as well as color changes on a scale of tens of centimeters to one meter, is interpreted to represent climatic cycles. Within the lower half of Unit I, interglacials are represented by foraminifer-bearing sediments, and glacials are represented by microfossil-barren silty clays. Both contain IRD. Each type of sediment represents about one-half of this part of the unit (Core 2H). Several interpretations are possible for the similarity in sediment thickness: (1) if the assumption of constant sedimentation rate is correct, sedimentation rates did not vary between glacial and interglacials; (2) lowered glacial sedimentation rate, and therefore the glacials represent longer periods of time; (3) lower interglacial sedimentation rate, and therefore the interglacials represent longer periods of time; or (4) the interglacials were initially thinner, and bioturbation has mixed the foraminifers into the adjacent sediment, lowering the microfossil content but extending it over a larger interval. The smear-slide data do not help us to distinguish among these possibilities, although the coarse-grained siliciclastic component does not increase during the glacial intervals. This may be because of constant ice-rafting, altered iceberg trajectories, or changes in the IRD volume, with the contribution from the different components remaining the same (e.g., 30% coarse quartz when IRD contribution is low or high.)

Throughout the upper half of Unit I, interglacials represent substantially less of the sediment recovered. The late Quaternary climatic regime, represented by Core 1H, may have been marked by longer or more pronounced glacial episodes, lower interglacial sedimentation rates, or higher glacial sedimentation rates. Paradoxically, interglacials may have been warmer, as indicated by two intervals of distinctly higher carbonate values (lighter in color), and dominated by foraminifers.

Volcanic Ash Layers

Forty-eight distinct ash layers, >1 cm thick, were identified in all the lithologic units except lithologic Unit V (Table 4, Fig. 3). The ash also occurs as sand to coarse, silt-sized, fresh glass shards in pocket infillings (Fig. 9B). These infillings are not included in Table 4 or Figure 3. They are thought to be produced by bioturbation (i.e., thin ash layers destroyed by bioturbation and/or ash displaced in burrows; Figs. 7 and 9A).

Thickness of individual ashes ranges from a few millimeters to 18 cm (6.6 cm average). Commonly the ashes show a fining upward trend with a sharp basal contact and a gradual upper contact showing evidence of mixing by burrowing (Fig. 8), but lacking distinct burrows. Many lower contacts have distinct burrows (Fig. 6). Ash color varies from black to gray with more or less brown, olive, or greens.

Colorless shards, which may indicate rhyolitic composition, are dominant over brown shards, which are either absent or only present in minor amounts. Morphologically, platy, bubble-wall shards are dominant over pumice and vesicular shards. The darkness of the ash layers appears to depend mainly on the amount of pyrite and pyrite-coated shards rather than on the amount of brown glasses. Within very dark layers (Fig. 6), the shards are commonly coated with pyrite.

Compared with ODP Sites 642 and 643, the ash layers of Hole 907A are distinctly thicker (7 cm vs. 1 cm) and more abundant. This is consistent with an air-fall origin from eruptions on Iceland leading to thicker deposits at Site 907, closer to the tephra source. If, however, the ashes are as rhyolitic as the light color indicates, then a non-Icelandic source may be required.

The ash content at this site presents another puzzle. Using the paleomagnetic age model (Fig. 3), ash-layer deposition has been fairly constant throughout the Neogene. Yet, the percentage of ash in the sediments is negligible in the Quaternary and upper Pliocene, and is relatively constant in the rest of the section, even though the number of ash layers increases (Figs. 2 and 3). This makes it difficult to invoke either a constant air fall of ash or bioturbation as mechanisms for distributing/redistributing the ash within these sediments. Bioturbators would have more time and more ash to disperse into the surrounding sediments in the intervals of slower sedimentation rate and higher ash density (e.g., 60–150 mbsf), and this is not seen.

BIOSTRATIGRAPHY

Introduction

Biostratigraphic studies of Site 907 demonstrate that it consists of Pliocene to Pleistocene hemipelagic sediments, upper and middle Miocene biosiliceous oozes, and middle Miocene volcanic ash-rich mud.

Because Leg 151 was the third DSDP/ODP leg in the Norwegian-Greenland Sea, some biostratigraphic correlations were made to DSDP Legs 38 and 94 and ODP Legs 104 and 105. However, correlation proved difficult for these northern sites because most of the standard planktonic schemes proved insufficient. Biostratigraphic difficulties encountered include the scarceness of calcareous material, high percentage of endemic species, high accumulation of volcanic ash, and variable preservation of siliceous microfossils, particularly in the Pliocene-Quaternary and in middle Miocene ash-rich sediments.

Diatoms

Diatoms at Site 907 are tentatively assigned to Neogene biozones defined by Schrader and Fenner (1976) from DSDP Leg 38, Site 348, which is located near Site 907. The chronology of the Leg 38 diatom biostratigraphy was later revised by Baldauf (1984). Several problems associated with previous studies, however, such as stratigraphic and sampling discontinuities and the use of rare and sporadically occurring taxa as marker species, limit the applicability of the previous zonations, even within the Iceland Plateau region.

Diatoms in Hole 907A are generally abundant and well preserved where they occur (Fig. 10). Samples from Cores 151-907A-1H through 151-907A-5H-CC are barren of diatoms. Several samples from Core 151-907A-6H contain non-age-diagnostic, heavily silicified diatoms, such as *Stephanopyxis turris*, suggesting dissolution of more lightly silicified forms. An assemblage of well-preserved diatoms, assigned to the *Thalassiosira oestrupii* Zone of Schrader and Fenner (1976), is identified in Sample 151-907A-6H-CC. This assemblage includes *T. oestrupii*, *Roperia tessellata*, *Nitzschia atlantica*, and other forms typical of the modern interglacial North Atlantic Ocean. It also includes rare *Nitzschia marina*/*reinholdii* transitional forms, which are characteristic of upper Pliocene to lower Pleistocene sediments of low to middle latitudes. *Proboscia (Rhizosolenia) barboi* is absent, as is *Thalassiosira nidulus*. The *T. oestrupii* Zone ranges down to near the Pliocene/Pleistocene boundary, according to Schrader and Fenner (1976), although Baldauf (1984) and Barron (1985) place the base of the *T. oestrupii* Zone in the upper Pleistocene.

The *P. (R.) barboi* Zone of Schrader and Fenner (1976) is identified in Sample 151-907A-7H-CC and in Core 151-907A-8H by the occurrence of *P. barboi*, *Thalassiothrix miocenica*, *T. nidulus* and *T. oestrupii*. Sample 151-907A-8H-CC contains *P. barboi*, *T. miocenica*, *T. lineatum*, *Coscinodiscus marginatus*, *Nitzschia pseudocylindrica*, *T. nidulus*, and common *Stephanogonia hanzawae*, indicating the upper Pliocene boundary between the *P. (R.) barboi* Zone and the *Thalassiosira kryophila* Zone (Schrader and Fenner, 1976). This sample also contains abundant *Chaetoceros* spores, indicating high primary production. The base of the Pliocene, within the *T. kryophila* Zone, is identified by the first occurrence of *T. oestrupii* and *Thalassiosira jacksonii* in Sample 151-907A-10H-3, 98–100 cm, or in the barren interval between Sample 151-907A-10H-CC and Sample 151-907-10H-3, 98-100 cm. This datum agrees well with Site 907 paleomagnetic data.

The *T. kryophila* Zone is identified down to Core 151-907A-11H. The upper Miocene *C. marginatus* Zone is recognized in Sample 151-907A-12H-1,75–76 cm, with the common occurrence of *C. mar-*

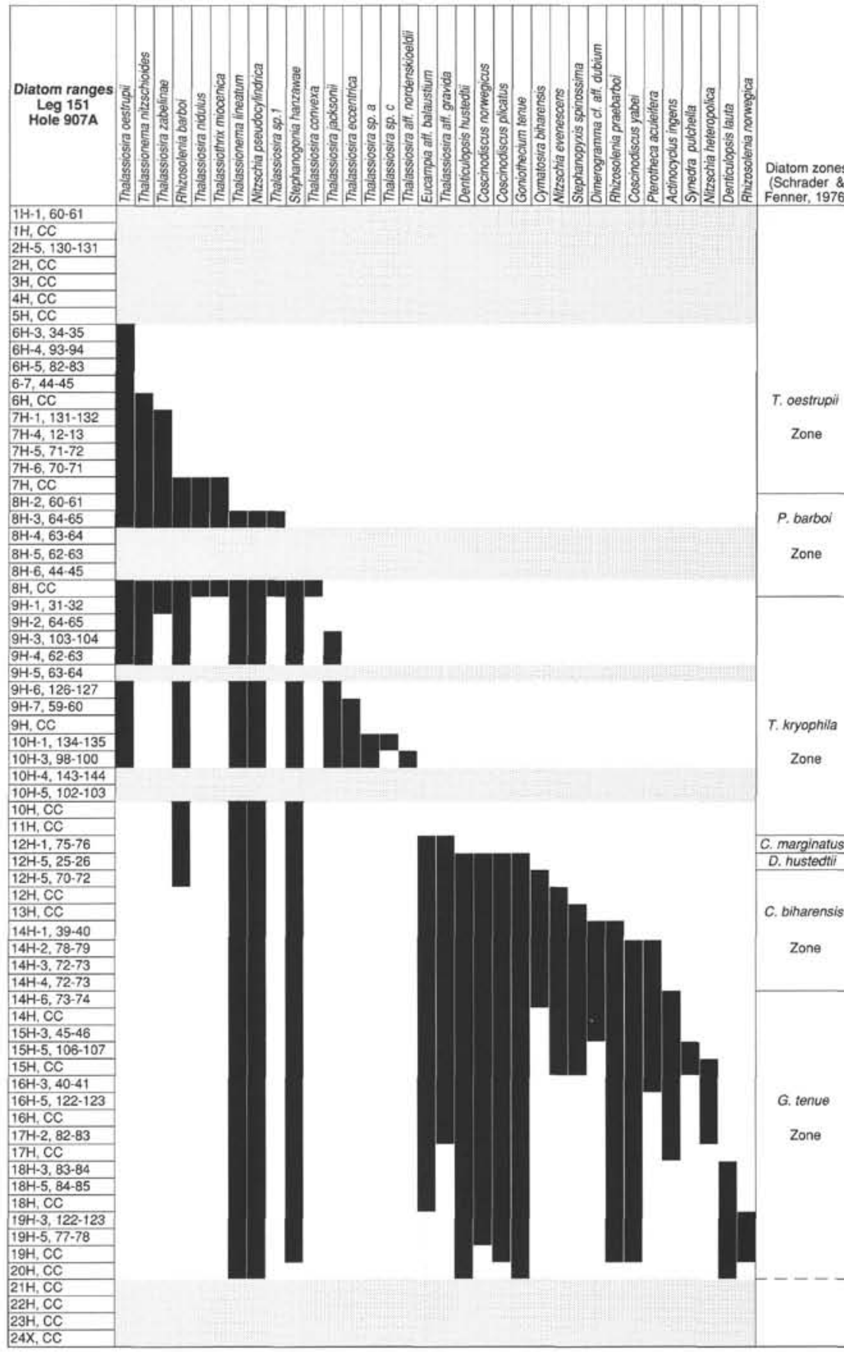

Figure 10. Occurrence of biostratigraphically important diatoms as recognized during shipboard analyses. Correlation to diatom zones of Schrader and Fenner (1976) is shown to the right. Shaded zones represent barren intervals.

ginatus. Diatoms of the top of the upper Miocene *Denticulopsis hustedtii* Zone are present in Sample 151-907A-12H-5, 25–26 cm.

The upper middle Miocene to upper Miocene *Cymatosira biharensis* Zone is present in Samples 151-907A-12H-5, 70–72 cm, through 151-907A-14H-6, 73–74 cm, with the occurrence of *C. biharensis*, *D. hustedtii*, *Goniothecium tenue*, *Eucampia* sp. aff. *E. balaustium*, and *Proboscia barboi/praebarboi* transitional forms. The top of this zone cannot be positively identified due to the absence of *Azpietia endoi* in Hole 907A. The middle Miocene *G. tenue* Zone, defined by the last occurrence of *Actinocyclus ingens*, is found in Sample 151-907A-14H-6, 73–74 cm. Also in this sample are *D. hustedtii*, *G. tenue*, *C. plicatus*, and *P. barboi/praebarboi* transitional forms. Middle Miocene sediments are recognized from beneath Sample 151-907A-14H-6, 73-74 cm, to Core 151-907A-20H-CC. *Proboscia praebarboi* s.s. has its highest occurrence in Sample 151-907A-15H-3, 45–46 cm. Sample 151-907A-18H-CC has the highest occurrence of *Denticulopsis lauta*. The oldest sediment identified by diatoms at Site 907 is the middle Miocene *G. tenue* Zone in Core 151-907A-20H. The fact that neither *Rhizosolenia miocenica* nor *Nitzschia porteri* were observed in Hole 907A suggests that the *R. miocenica* Zone is not present. Cores 151-907A-21H through 151-907A-24X are barren of diatoms. The thick middle Miocene section results from high primary productivity and complementary good silica preservation, which led to unusually high sediment accumulation rates.

Silicoflagellates

The occurrence of biostratigraphically important silicoflagellates was monitored during shipboard analysis of diatoms, although no detailed studies of silicoflagellate biostratigraphy were attempted. Sili-

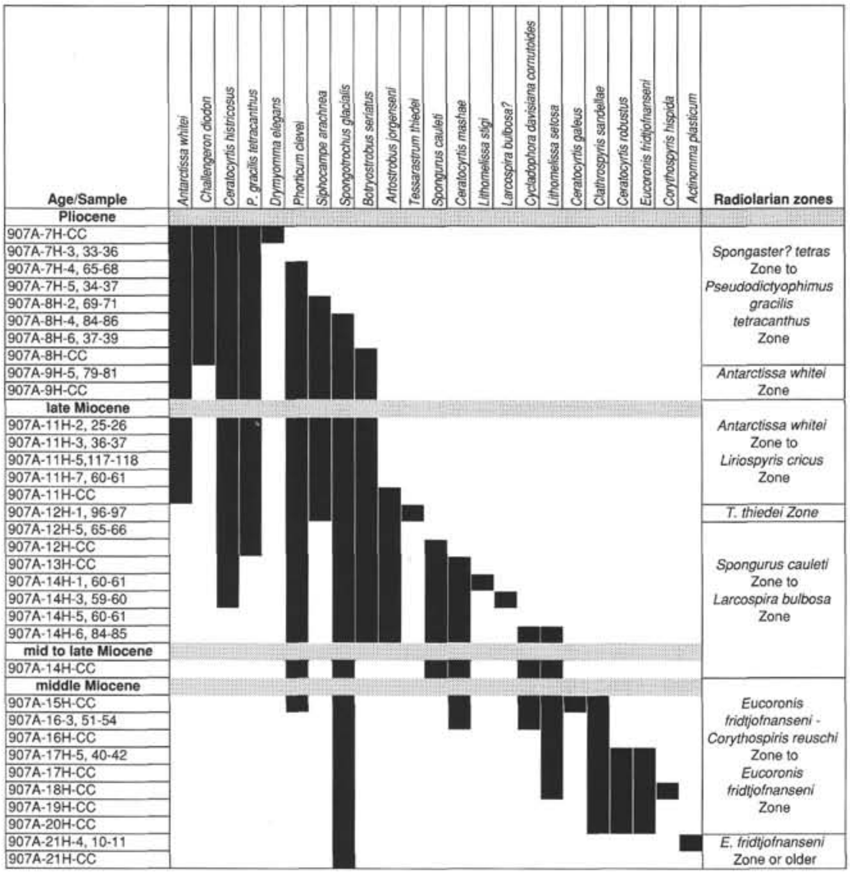

Figure 11. Ranges of selected radiolarians in Hole 907A. Barren intervals are not included. Zonal assignment (on right) follows zonation of Goll and Bjørklund (1989).

coflagellate biostratigraphic studies in the Norwegian Sea (ODP Leg 104) by Ciesielski et al. (1989) and Locker and Martini (1989) were used for regional biostratigraphic reference, despite conflicts of nomenclature between these studies. No stratigraphic conflicts between diatoms and silicoflagellates were observed.

Radiolarians

Radiolarian biostratigraphy is based on the examination of strewn slides of sediment >63μm prepared from Samples 151-907A-1H-CC to -23H-CC and an additional 20 core samples collected on board. Although the occurrence of radiolarians in core-catcher samples is nearly continuous below Core 151-907A-5H, diversity, abundance, and preservation vary widely throughout the observed sequence. The fauna bears strong resemblance to assemblages documented in the Iceland and Norwegian seas on DSDP Leg 38 (Bjørklund, 1976) and ODP Leg 104 (Goll and Bjørklund, 1989). Rare cosmopolitan species are present in addition to a few forms described from North Atlantic Ocean DSDP sites (e.g., Rockall Plateau; Westberg-Smith and Riedel, 1984). Where possible, the biostratigraphic zonation developed by Goll and Bjørklund (1989) for the Norwegian Sea has been applied to Site 907. Several markers used in this zonation, however, are absent, resulting in longer-ranging age assignments for some sedimentary intervals. Absence of these markers may be due to poor preservation and generally low abundances in parts of the hole, to hiatuses, or to the position of the site outside of the biogeographic range of these species. Occurrences of biostratigraphically useful taxa are shown in Figure 11.

Samples 151-907A-1H-CC through 5H-CC, representing the Quaternary (and possibly uppermost Pliocene) record at Site 907, are barren of radiolarians. Non-age-diagnostic species of *Actinomma, Spongurus,* and *Spongotrochus* are present in Sample 151-907A-6H-CC. Samples 151-907A-7H-CC through 9H-CC contain a moderately preserved assemblage of upper Pliocene radiolarians, including abundant *Antarctissa whitei* and specimens of *Challengeron diodon, Ceratocyrtis histricosus, P. gracilis tetracanthus, Phorticum clevei, Siphocampe arachnea, Spongotrochus glacialis,* and *Hexaconthium pachydermum. Cycladophora davisiana davisiana,* a marker for the uppermost Pliocene and Quaternary and a relatively cosmopolitan species, is not present in this hole. On the basis of its absence, the abundance of *A. whitei* (which has its highest range in the uppermost Pliocene *Spongaster*? *tetras* Zone of Goll and Bjørklund, 1989), and the presence of the marker taxon *P. gracilipes tetracanthus*, Samples 151-907A-7H-3, 33–36 cm, and 151-907A-8H-CC are placed in the middle to upper Pliocene *S. tetras* Zone–*P. gracilipes tetracanthus* Zone of Goll and Bjørklund (1989). The fauna in Samples 151-907A-9H-5, 79–81 cm, and 151-907A-9H-CC contains *A. whitei* in the absence of *P. gracilipes tetracanthus* and *Liriospyris cricus* (marker taxon for the upper Miocene), suggesting an assignment of this assemblage to the lower Pliocene *A. whitei* Zone.

Sample 151-907A-10H-CC is barren of radiolarians, although other siliceous microfossils, including sponge spicules and rare diatoms, are present. Samples from Core 151-907A-11H (151-907A-11H-2, 25–26 cm, -11H-3, 36–37 cm, -11H-5, 117–118 cm, and -11H-CC) have a very low abundance and diversity of radiolarians, including *S. glacialis, C. histricosus, H. pachydermum, Botryostrobus seriatus,* and *Artostrobus jorgenseni.* Unfortunately, none of these species are marker taxa in the sense of Goll and Bjørklund (1989), with the exception of *A. whitei.* On the basis of the range of this species and its stratigraphic position in the hole, Core 151-907A-11H samples also are assigned to the lower Pliocene *A. whitei* Zone or the upper part of the upper Miocene *L. cricus* Zone. Paleomagnetic data from this site supports an age of late Miocene, although *L. cricus* is not present in Hole 907A. A short hiatus at this level also is indicated by the paleomagnetic data, and may account for the absence of this species. It also should be noted that some samples within this core and the next (e.g., Samples 151-907A-11H-7, 60–61 cm, and 151-907A-12H-1, 96–97 cm) are completely barren of radiolarians, illustrating the variable nature of silica preservation at Site 907.

Radiolarians in Sample 151-907A-12H-5, 65–66 cm, include *Tessarastrum thiedei, Siphocampe arachnea, C. histricosus,* and *S. glacialis.* On the Vøring Plateau the full range of *T. thiedei* is within the upper Miocene and defines the *T. thiedei* Zone of Goll and Bjørklund (1989). Below this level, Samples 151-907A-12H-CC, -13H-CC, -14H-1, 60–61 cm, -14H-3, 59–60 cm, and -14H-5, 60–61 cm, also are assigned to the upper Miocene. These samples lack *T. thiedei* but contain an abundance of the upper Miocene marker taxon *Spongurus cauleti.* Marker taxa for intermediate zones between *T. thiedei* Zone and the *S. cauleti* Zone are absent (i.e., *Larcospira bulbosa* and *Hexalonche esmarki*), and these samples therefore may range in zonal assignment from the base of the *S. cauleti* Zone to the top of the *L. bulbosa* Zone of Goll and Bjørklund (1989). A possible hiatus in this interval is suggested by paleomagnetic data, which may account for the absence of marker species.

Sample 151-907A-14H-6, 84–85 cm, contains rare specimens of the lower upper Miocene marker *S. cauleti* co-occurring with radiolarian species more typical of the middle Miocene, including *Lithomelissa setosa* and *Ceratocyrtis mashae.* The assemblage is herein assigned to the lower upper or upper middle Miocene. The first occurrence of *S. cauleti* at Hole 907A represents one of several chronostratigraphic discrepancies between this locality and Sites 642 and 643 on the Vøring Plateau in the Norwegian Sea. Goll and Bjørklund (1989) calibrated the first appearance of *S. cauleti* with paleomagnetic data at Sites 642 and 643. According to their studies, this species appeared and became extinct in a short interval approximately 6.3 Ma to 7.9 Ma. Calibration of the first and last occurrences of *S. cauleti* to paleomagnetic data at Site 907, however, gives an older range of approximately 8.4 to 10.8 Ma. Similar results have been found on board in comparing upper and middle Miocene diatom events with paleomagnetic data from the 6.0 to 13.0 Ma interval. Radiolarian events prior to 6.0 Ma and after 13.0 Ma are still in agreement with calibrated ages determined by Goll and Bjørklund (1989).

Samples 151-907A-14H-CC through -21H-4, 10–11 cm, consist of more typical middle Miocene radiolarians of the Norwegian-Greenland Sea, including: *Eucoronis fridtjofnanseni, C. mashae, Ceratocyrtis robustus, Clathrospyris sandellae, Corythospyris hispida,* and *Actinomma plasticum.* Although a few of the middle Miocene marker taxa of Goll and Bjørklund (1989) have been documented (e.g., *E. fridtjofnanseni),* many others are missing, and zonal assignments in this part of the core are difficult. Some absences may be due to the presence of an upper middle Miocene hiatus, which also is suggested by diatom and paleomagnetic data. Post-cruise study of this interval with detailed sampling will determine whether these markers are truly absent, and if so, how the Goll and Bjørklund (1989) zonation should be modified to better reflect radiolarian biostratigraphy on the Iceland Plateau.

No radiolarians older than middle Miocene have been documented at Site 907. Volcanic-rich Samples 151-907A-21H-CC, -22H-CC, and -23H-CC have numerous specimens of *Spongotrochus* spp., *Porodiscus* spp., and *Actinomma* spp. None of the species is known to be age diagnostic. One of these samples, 151-907A-21H-CC, is unique in possessing a nearly monogeneric and very abundant assemblage of spongodiscids. Generally considered to be indicative of surface faunas, these spongodiscids may suggest a relatively restricted environment for radiolarians at the time of deposition.

Calcareous Nannofossils

Calcareous nannofossils are rare to absent in Hole 907A, except in a calcareous layer in the upper part of the sequence where they are moderately preserved. Nannofossils occur in nine of the 31 samples analyzed. Sample 151-907A-2H-CC contains a few specimens of *Coccolithus pelagicus, Gephyrocapsa parallela, Gephyrocapsa oceanica,* and *Helicosphaera carteri.* The presence of *G. parallela* indicates an age younger than middle Quaternary above the Jaramillo Event (younger than 0.89 Ma; Sato et al., 1991) and correlates to upper NN19 to NN21 zonation of Martini (1971). Abundant reworked specimens from the Upper Cretaceous and Paleogene, such as *Watznaueria barnesae, Prediscosphaera cretacea, Micula decussata, Kamptnerius magnificus, Microrhabdulus decoratus, Isthmolithus recurvus, Calcidiscus formosus, Reticulofenestra umbilica,* and *Dictyococcites bisectus,* are also present. These reworked specimens amount to more than 90% of the total number of calcareous nannofossils found in this sample.

Samples 151-907A-7H-3, 56–57 cm, -7H-6, 101-102 cm, and -7H-CC, 7–10 cm, are nannofossil ooze characterized by the abundant occurrence of *C. pelagicus,* which forms more than 99% of total specimens. Rare specimens of *Crenalithus doronicoides, Dictyococcites productus,* and *Pseudoemiliania lacunosa* are also in these samples. The occurrences of *P. lacunosa* and *C. doronicoides,* without *Gephyrocapsa* spp. and *Reticulofenestra pseudoumbilica,* indicate assignment to upper Pliocene Zones NN16 to NN18.

Sample 151-907A-11H-2, 21–22 cm, contains *R. pseudoumbilica, Reticulofenestra gelida,* and abundant *C. pelagicus,* but no *Coccolithus miopelagicus.* Thus, the flora ranges from Zone NN8 to Zone NN15 (upper Miocene to lower Pliocene). A few *C. pelagicus* specimens are found in Samples 151-907A-8H-CC, -14H-CC, and -15H-CC. However, zonal marker species are not found in these three samples.

Donnally (1989) studied calcareous nannofossils from Leg 104 and found relatively few nannofossils, but did find reworked specimens from the Cretaceous and Paleogene in the middle Miocene to Quaternary sediments. Nannofossil assemblages of Hole 907A are similar to those from Leg 104 in that they are characterized by low diversity and abundance of nannofossils and by the presence of Cretaceous and Paleogene reworked specimens. However, species diversity is lower, and the nannofossil occurrence is more limited in Hole 907A.

Planktonic Foraminifers

Planktonic foraminifer biostratigraphy of Site 907 is based on the examination of core-catcher and 25 additional samples. Planktonic foraminifers are abundant but low in diversity from the top of Hole 907A down to Sample 151-907A-2H-1, 131–132 cm. The abundance decreases drastically between Sample 151-907A-2H-3, 137–140 cm, and -3H-CC. No planktonic foraminifers were obtained beneath Sample 151-907A-3H-CC with the exception of Core 151-907A-7H.

The *Neogloboquadrina* biostratigraphy developed by Spiegler and Jansen (1989) was used in this study. This zonation recognizes the occurrence of *Neogloboquadrina pachyderma* sinistral Zone as younger than 1.7 Ma, and the *Neogloboquadrina atlantica* sinistral Zone as Pliocene. This zonation is useful in interpreting two planktonic foraminiferal zones in Hole 907A. Unfortunately, both zones in Hole 907A are separated by a barren interval, preventing better planktonic foraminiferal biostratigraphy.

The *N. pachyderma* sinistral Zone is recognized in Samples 151-907A-1H-1, 15–18 cm, through -3H-CC. The assemblages are dominated by the cold-water species *N. pachyderma* sinistral and very few specimens of *Globigerina bulloides, Turborotalia quinqueloba,* and *N. pachyderma* dextral. Further support of a Pleistocene age for the upper portion of Hole 907A are rare ice-rafted *Inoceramus* prisms and Cretaceous foraminifers found in Sample 151-907A-2H-CC. The presence of ice-rafted sediments with abundant Pleistocene planktonic foraminifera could indicate the initial phase of deglaciation. The *N. atlantica* sinistral Zone is documented in Core 151-907A-7H. Species identified include the zone fossil and *G. bulloides.*

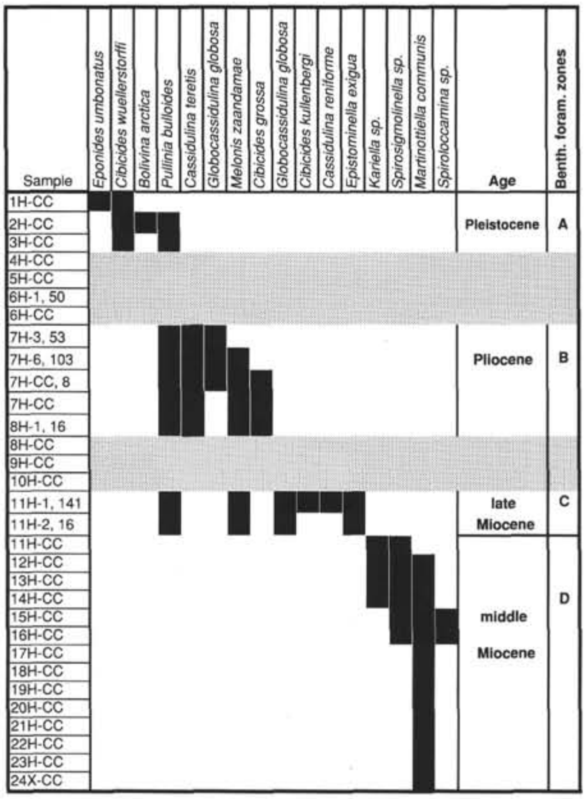

Figure 12. Percentage data of biostratigraphically important benthic foraminifers in Hole 907A.

Benthic Foraminifers

Shipboard analyses of benthic foraminifers at Site 907 were done using core-catcher samples and selected shipboard samples (Fig. 12). The benthic foraminifers range in age from the Miocene to Quaternary and dominate planktonics in most shipboard samples. In the upper Quaternary section, low productivity appears to be the reason for the low sedimentation rate. The carbonate-rich interval is found from 0 to 17 mbsf but includes only two core-catcher samples. Dissolution appears to be the main cause of the lack of calcareous material in the Pliocene and especially in the Miocene where calcareous material is found only in one short interval.

Site 907 can be divided into four benthic foraminiferal assemblage zones. These are designated, from top to bottom, as Zone A through D. Zone A is represented by the two uppermost core-catcher samples. The uppermost Sample 151-907A-1H-CC contains only rare *Eponides umbonatus*. This foraminifer is only found in the Norwegian Sea in Pleistocene sediments younger than Isotope Stage 13. Sample 151-907A-2H-CC contains *Bolivina arctica*. This species is an endemic species from the Arctic Ocean and is found dominantly on the Vøring Plateau during Isotope Stages 16–18. Therefore, Zone A represents the carbonate-bearing Quaternary section at Site 907. Beneath Zone A is a barren interval; therefore, it is unclear where the boundary lies between the two zones.

Zone B is characterized by abundant *Cassidulina teretis* and contains *Cibicides grossa* in the lower part. Both of these species are considered indicative of Pliocene sediments in the Arctic Ocean (King, 1983; Knudsen and Asbjörnsdottir, 1991). In continental shelf sediments, the disappearance of *C. grossa* is used to mark the Pliocene/Quaternary boundary, but the absence of *C. grossa* from the upper part of Zone B may be an artifact of the sparse sampling interval. Furthermore, on the Vøring Plateau, Pliocene sediments contain abundant *C. teretis* and *Globocassidulina globosa*. Therefore, the presence/absence of *C. grossa* is not used as the Pliocene/Quaternary boundary marker in this study.

Upper Miocene foraminifers, a *Cibicides kullenbergi* and *Epistominella exigua* assemblage, are found in Samples 151-907A-11H-1,139–143 cm, and 151-907A-11H-2, 15–17 cm. Noticeably absent are the *Uvigerina* spp., which are common in the middle Miocene of Site 642 (ODP Leg 104). These samples constitute Zone C (Fig. 12).

Middle Miocene foraminifers are found in the lower half of Site 907A from Samples 151-907A-11H-CC through -24X-CC. Zone D consists of rare agglutinated foraminifers including *Martinottiella communis*, *Spirosigmoilinella sp.*, and *Spiroloccamina sp.* These foraminifers also were found in the Miocene sediment of Legs 38 and 104. This assemblage is found in the core catchers up to and including Sample 151-907A-24X-CC, which consists of gravel with sandy matrix. The matrix contained an agglutinated assemblage of variable preservation. This assemblage may be in situ, but it also may represent reworked sediment during the drilling process.

Palynology

Core-catcher samples were processed from Cores 151-907A-1H through -23H. Heavy liquid separation of residues was not done. Therefore, all sample slides have large amounts of silt, and the palynomorphs are diluted and rare to few in abundance in most samples. Samples 151-907A-2H-CC, -3H-CC, and -5H-CC through -8H-CC are barren of organic matter.

Amorphous organic matter (AOM) and plant fragments are rare in Samples 151-907A-1H-CC, -4H-CC, -9H-CC, and -10H-CC, but become increasingly common downhole beginning from Sample 151-907A-11H-CC, and are most abundant in Sample 151-907A-19H-CC. Terrestrial pollen and spores show a pattern similar to AOM and plant fragments, and are most common in Sample 151-907A-22H-CC.

Dinoflagellate cysts are rare when present. Preservation is moderate to poor. Except for rare occurrences of *Achomosphaera* sp. and *Spiniferites* sp. in Sample 151-907A-1H-CC, no dinoflagellates were observed above Sample 151-907A-12H-CC. No zonal boundaries could be distinguished, as most zonal marker species were not observed. However, *Palaeocystodinium golzowense* occurs sporadically from Samples 151-907A-14H-CC through -23H-CC, and *Systematophora* sp. occurs sporadically from Samples 151-907A-12H-CC through -23H-CC. The genera *Palaeocystodinium* and *Systematophora* have their last occurrences in middle to lower upper Miocene sediments in the North Atlantic Ocean, Labrador Sea, Baffin Bay, and Norwegian Sea (Head et al., 1989b, c), which indicates that Samples 151-907A-14H-CC through -23H-CC are of early late Miocene age or older. In addition, a specimen similar to that figured as *Cristadinium* sp. 1 by Head et al. (1989b) occurs in Sample 151-907A-18H-CC. *Cristadinium* sp. 1 was reported in middle to lower upper Miocene sediments from Baffin Bay (Head et al., 1989b). A specimen similar to *Reticulatosphaera actinocoronata* occurs in Sample 151-907A-22H-CC. This species has a reported age range of late Eocene to early Pliocene in the North Atlantic Ocean (Head et al., 1989c). Specimens similar to *Impagidinium* sp. 3 of Manum et al. (1989) occur in Sample 151-907A-12H-CC. This taxon ranges from lower to upper Miocene at ODP Site 643. Finally, Sample 151-907A-23H-CC contains rare *Labyrinthodinium truncatum*. This taxon has its lowest occurrence at about the base of the middle Miocene in the Norwegian Sea (Manum et al., 1989) and Baffin Bay (Head et al., 1989b). Thus, the base of the sediment sequence at Site 907 is constrained to be no older than middle Miocene. Additional taxa observed in this section are *Achomosphaera* sp., several acritarch forms, *Batiacasphaera* sp., *Cyclopsiella*? sp., *Lejeunecysta* sp., *Operculodinium* sp., *Platycystidia*? sp., *Selenopemphix* sp., *Spiniferites* spp., and *Tectatodinium* sp.

Biostratigraphic Synthesis

Site 907 was selected for two primary objectives: (1) to be used as the western part of a transect across the Norwegian-Greenland Sea; (2) to provide a high-resolution stratigraphy of calcareous and siliceous microfossils. These objectives were only partially met. Low sedimentation rates in the Brunhes will make high-resolution studies difficult at this site. However, Site 907 remains useful as a western tie-point for Miocene to Quaternary stratigraphy and paleoceanography of the Norwegian-Greenland Sea.

Based on microfossil evidence, Site 907 extends to middle middle Miocene. Siliceous microfossils indicate an age of 14 Ma in Sample 151-907A-21H-CC, but age-diagnostic fossils are absent below that level. Dinoflagellate evidence below Core 151-907A-21H indicates the base of the sediment section is no older than about 16 Ma (see "Sedimentation Rates and Their Implications" in the "Paleomagnetics" section, this chapter).

The upper Miocene/middle Miocene boundary is recognized in Core 151-907A-14H-6 (129.5 mbsf) by the last occurrence of the diatom *A. ingens*, which marks the top of the *G. tenue* Zone (Fig. 13). The Pliocene/upper Miocene boundary occurs at 83.3 mbsf, in the top of Core 151-907A-10H according to paleomagnetic evidence (see "Paleomagnetics" section, this chapter). This is corroborated by the first occurrence of diatoms *T. oestrupii* and *T. jacksonii* in Sample 151-907A-10H-3, 98–100 cm. These diatom datums are dated by Bodén (1992) at about 5.2 Ma. Radiolarians, calcareous nannofossils, and benthic foraminifers also indicate samples from Core 151-907A-11H to be Miocene.

The Pliocene/Quaternary boundary is recognized at 37 mbsf in the middle of the Olduvai Event (Cande and Kent, 1992). This agrees with the calcareous nannofossils and planktonic and benthic foraminifers, which recognize Pliocene microfossils in Core 151-907A-7H. Biostratigraphic assignments to the Quaternary are confirmed by calcareous nannofossils, and planktonic and benthic foraminifers, which were found in Sample 151-907A-2H-CC.

Middle Miocene sediments are rich in siliceous microfossils, which indicates that surface waters were enriched in nutrients, possibly resulting from upwelling conditions in the Norwegian-Greenland Sea during this time. This upwelling increased the productivity of surface-water species but in turn decreased bottom-water pH, resulting in the dissolution of the calcareous microfossils. This upwelling continued into the late Miocene and early Pliocene. However, there were two brief episodes of carbonate preservation, which are represented in Cores 151-907A-11H and 151-907A-7H.

The increase of ice rafting during the late Pliocene and the return of colder conditions are coeval with a decline in the abundance of siliceous microfossils. An interval spanning the upper Pliocene to lower Quaternary is barren of all microfossils. The cause of this barren interval is unknown, but a similar interval was found at Leg 104 sites (Osterman and Qvale, 1989). Beginning in the Brunhes, calcareous microfossils become more abundant in the upper two cores of Hole 907A, predominately during the interglacial intervals.

PALEOMAGNETICS

Shipboard paleomagnetic studies performed at Site 907 followed the methods described in the "Explanatory Notes" chapter, this volume. The prime objective of these studies was to recover a magneto-

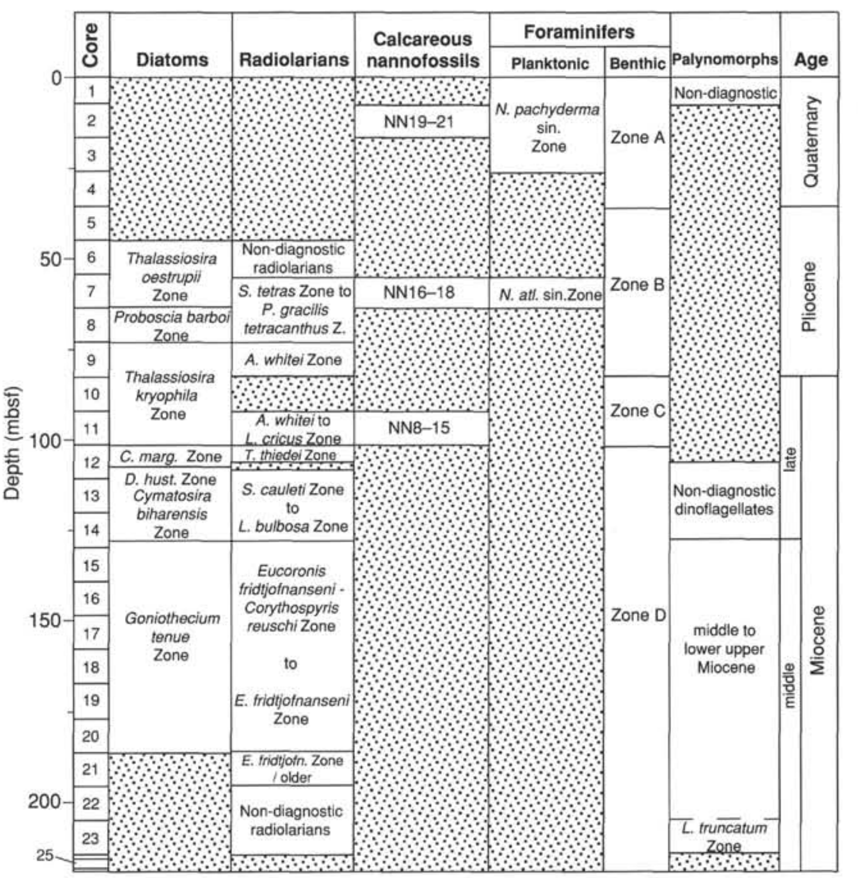

Figure 13. Biostratigraphies and correlation of the different microfossil groups of Hole 907A.

stratigraphic record from the core that could provide a chronostratigraphic framework for the sediments of Site 907.

General Magnetic Character of Site 907 Sediments

The intensity of the natural remanent magnetization (NRM) of the Hole 907A sediments was fairly high (~10^{-2} Am^{-1}) and remained quite measurable after AF (alternating field) demagnetization to 30 mT (NRM_{30}). The magnitude of the NRM after AF demagnetization did show significant variation with depth and was correlated with magnetic susceptibility changes as determined from the cores (Fig. 14). Susceptibility and especially NRM_{30} intensity show a tendency toward bimodality (Fig. 15), and perhaps suggest that these distributions are controlled by processes other than dilution, such as grain size variation or chemical alteration. The occasional high amplitude spikes in susceptibility and NRM_{30} are often related to abrupt depositional events such as ice-rafted debris (IRD) pulses or ash layers. The general trend toward lower intensities at depth is similar to that observed at other sites in the Norwegian Sea, but the decrease is much more gradual and smaller in magnitude than the rather abrupt decrease in intensity observed in the Leg 104 sites (Bleil, 1989). The sharp zone of low NRM_{30} intensities between 168 and 182 mbsf in Hole 907A is accompanied by a similar but less abrupt low in magnetic susceptibility, and is probably related to the presence of pyrite in this zone. Although the NRM_{30} intensity and susceptibility do not correlate with trends in the Leg 104 sites, they could be a useful tool for local lithological correlations.

AF Demagnetization Behavior

Detailed progressive AF demagnetization experiments were performed on seven discrete pilot samples with peak demagnetizing fields ranging up to 60 mT (Fig. 16). An additional pilot group of cores was demagnetized at five levels in the pass-through AF demagnetizer. These preliminary experiments indicate the NRM is carried by a fairly high coercivity material with a median destructive field generally at least 20 mT, and in many cases as large as 30 mT. AF demagnetization also indicates that the NRM of the cores often contains spurious components of magnetization that were largely removed by AF demagnetization to 30 mT. Often these lower coercivity components of NRM were directed steeply downward and are likely to be either a magnetization acquired in the drilling environment, or a viscous remanent magnetization (VRM) acquired in situ in the Earth's present-day field (present-day field inclination at the sampling site = +80°). In some cases (e.g., Fig. 17), the low coercivity remanence demagnetized between 10 mT and 30 mT was nearly perpendicular to the core axis and was likely acquired at some time

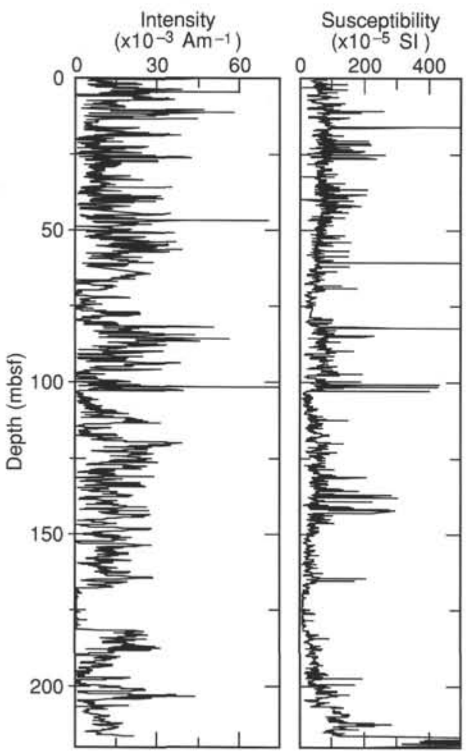

Figure 14. Profiles of NRM_{30} intensity and whole-core magnetic susceptibility vs. depth at Hole 907A.

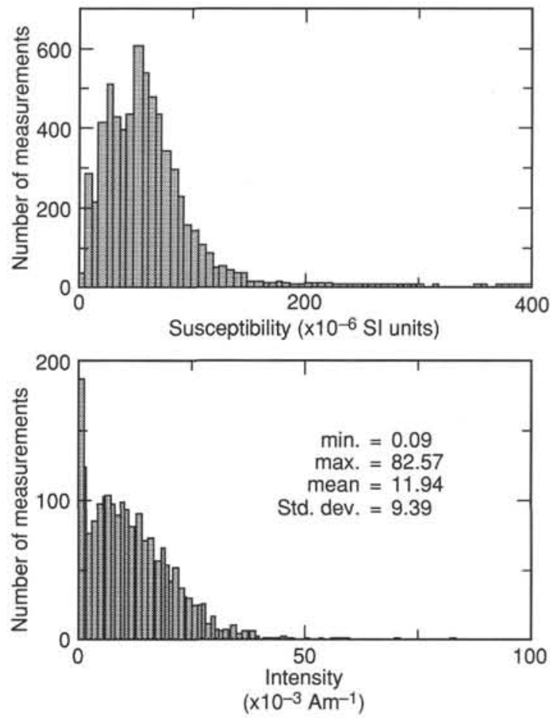

Figure 15. Distributions of NRM_{30} intensity and whole-core magnetic susceptibility values at Hole 907A.

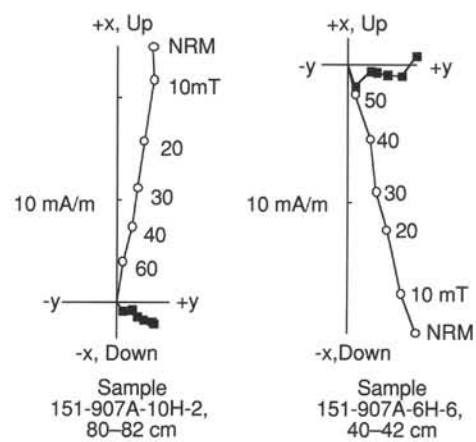

Figure 16. AF demagnetization diagrams for two discrete samples from Cores 151-907A-10H and 151-907A-6H. Solid squares = projection onto the horizontal plane; open circles = projection onto the vertical plane parallel to the split face of the core.

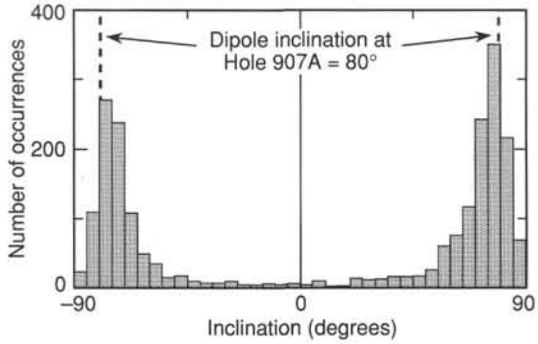

Figure 17. Distribution of inclination values after 30-mT demagnetization treatment at Hole 907A. Dashed lines indicate the expected inclination of the geomagnetic field at the sampling site.

during the shipboard processing of the core. Whatever the source of these spurious magnetizations, a 30-mT demagnetization treatment was effective in isolating a characteristic remanent magnetization, and the magnetic polarity stratigraphy of the Hole 907A cores from 0 to 215 mbsf was interpreted from the inclination of the NRM after a 30-mT treatment.

The NRM_{30} inclination measured on the Hole 907A cores is highly bimodal in distribution, with two rather strong peaks centered between plus and minus 75° to 80° and few shallow inclinations recorded. We interpret these two populations of NRM_{30} inclinations as characteristic remanent magnetizations of normal and reversed polarity. The two populations are skewed slightly to lower inclinations, suggesting the imperfect removal of spurious shallow magnetizations or perhaps a slight sedimentary inclination error. The marked symmetry of the means of the two distributions, with a lack of preferential shallowing of the reversed polarity inclinations relative to the normal polarity inclinations, indicates that the 30-mT demagnetization treatment has effectively mitigated the effects of drilling-induced remagnetizations for most of these sediments.

Magnetic Polarity Stratigraphy

Identification of Magnetozones

The steep upward and downward characteristic magnetization inclinations yield a coherent pattern of reversed and normal magnetozones in cores from Hole 907A (Fig. 18). Identification of magnetozones in Hole 907A was based entirely on inclination data. Because of the high latitude of this site and the expectation that the magnetic declination record would contain little information, the core orientation tool was not deployed. The NRM_{30} inclinations yield a crisp magnetostratigraphic signal with few zones of indeterminate polarity. Minor perturbations to the inclination record occur in the vicinity of core breaks (see for example the top of Core 151-907A-7H or the top of Core 151-907A-20H, Fig. 18), but these are very thin (~10–20 cm). Thicker disturbed zones were observed in Core 151-907A-2H, which was troubled by flow-in in Sections 151-907A-2H-1 and -2H-5. Thus, most of the inclination variation in that core is probably not related to geomagnetic field behavior. Sporadic large dropstones were observed in the split cores; if these were large enough and free of the core matrix, they were temporarily removed from the core during pass-through measurements. Some spikes observed in the inclination record are likely the result of undetected dropstones within the core.

Magnetozones were identified on the basis of a coherent sequence of steep (>+60°) positive (normal polarity) or steep (<–60°) negative (reversed polarity) inclinations that spanned more than 20 cm (two independent pass-through measurements) of the core. Several thin intervals with complicated inclination signals are identified in Figure 18 by gray zones in the polarity column. These are potentially useful correlation markers, but their proximity to core breaks in some cases and their overall thin character lead us to look for their independent confirmation in other nearby cores before identifying them as bona fide short subchrons. We have identified these as inclination perturbations in Figure 18, but they are not used as chronostratigraphic calibration points in any subsequent analysis.

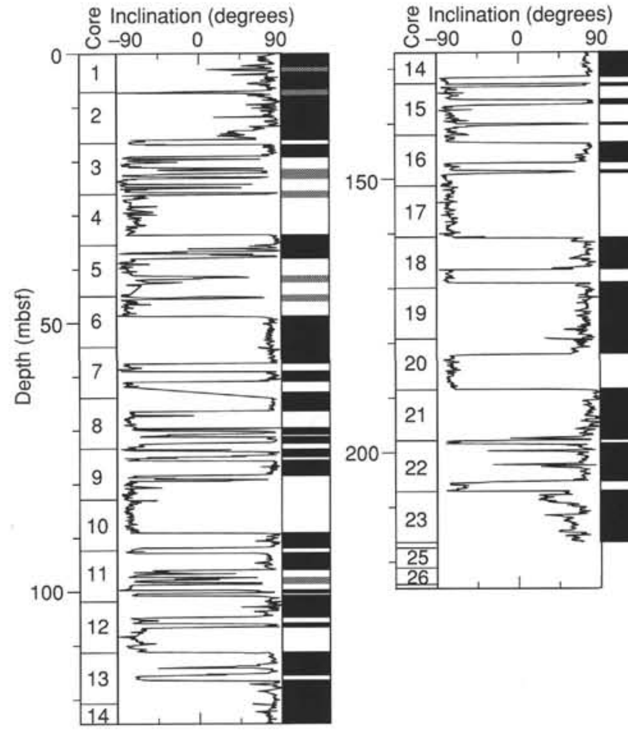

Figure 18. Inclination of the characteristic magnetization after 30-mT demagnetization treatment. Core boundaries are indicated on the left, and the interpreted magnetozone boundaries are indicated on the right.

Correlation with Geomagnetic Polarity Time Scale

In Figure 19 we have proposed a set of correlations between the magnetozones identified in Hole 907A and the geomagnetic polarity time scale (GPTS) of Cande and Kent (1992). Down to 95 mbsf the match is excellent, with only one of Cande and Kent's (1992) chrons missing (C2r1n). The predicted position of this chron is near disturbed zones in Cores 151-907A-5H and -6H, so it is not surprising that it fails to appear in the polarity record. Below 95 mbsf the correlation to the GPTS is considerably less clear. We have chosen to correlate the normal polarity zone between 101.3 and 105.2 mbsf with C4n2, and thus we suggest that most of C3B is missing in the Hole 907A record because of a hiatus between the termination of C4n1n and the onset of C3Ar. This assertion receives some independent support in the observation that the *Coscinodiscus marginatus* diatom zone is very thin in Core 151-907A-12H (see "Biostratigraphy" section, this chapter). Further down the core, we encounter another mismatch between 105 and 112 mbsf, where C4A apparently is missing from the record between the termination of C5n.1n and the onset of C4Ar.1n. We have correlated the thick normal magnetozone between 112 and 129 mbsf with the long C5n, but just below this zone another temporal discontinuity is suggested by the absence of the many short normal chrons of C5An in the Hole 907A record. Between 140 and 195 mbsf the magnetic polarity signal from Hole 907A is well defined; however, it is difficult to match this pattern of polarity zones

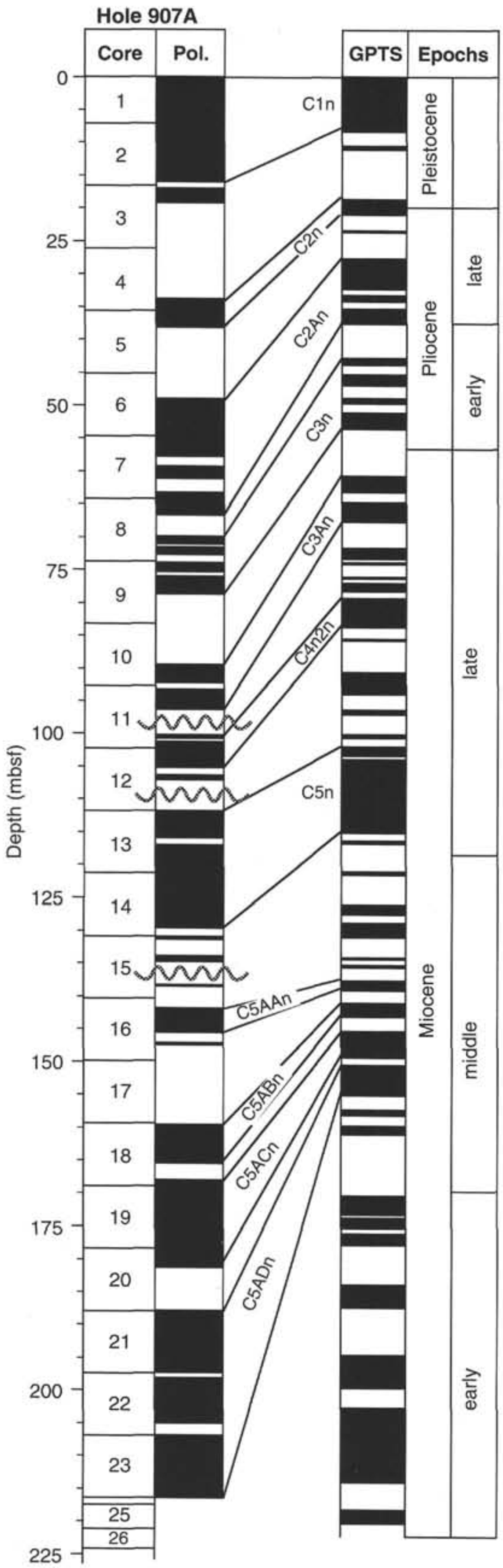

Figure 19. Correlation of the magnetostratigraphy of Hole 907A to the geomagnetic polarity time scale (GPTS) of Cande and Kent (1992).

with the GPTS. We suggest that this part of the stratigraphic section is greatly expanded and correlate the four normal polarity zones observed in this interval to C5AD to C5AA.

In summary, the paleomagnetic analysis of cores from Hole 907A yields good temporal control from 0 to 95 mbsf, with an excellent match to the GPTS. In the interval between 95 and 140 mbsf, the correlations are less complete, and therefore the temporal control is more speculative. Below 140 mbsf the thick magnetozones suggest a higher sedimentation rate. The preferred correlation to the GPTS suggested in Figure 19 requires the least amount of hiatus, but this correlation is by no means unique. Without independent chronological control, the temporal correlation suggested for this interval should be considered tentative at best.

Sedimentation Rates and Their Implications

Taking at face value the age vs. depth model implied by the correlations in Figure 19, we obtain average sedimentation rates of about 20 m/m.y. for the upper 65 m of core (Fig. 20, Table 5). Between 65 and 150 m, the sedimentation rate often decreases to less than 10 m/m.y., and below 150 m the age model suggests rapid deposition rates on the order of 25 to >40 m/m.y. Preliminary diatom biostratigraphy provides some independent tests of the age model portrayed in Figure 20. The temporal ranges of *Cymatosira biharensis*, *C. marginatus*, and *Thalassiosira kryophila* (Baldauf, 1984) are consistent with their depths of occurrences and implied magnetostratigraphic ages in Hole 907A; however, the *Thalassiosira oestrupii* and *Proboscia barboi* diatom zones extend to much older strata in Hole 907A than Baldauf (1984) indicates. This inconsistency occurs during the well-defined portion of the magnetostratigraphy and leads us to suggest that *T. oestrupii* and *P. barboi* have a wider range than suggested by Baldauf (1984).

Conclusion

Paleomagnetic analysis of Hole 907A yields a well-defined polarity stratigraphy. The magnetostratigraphy of the upper 100 m of the core correlates well to the GPTS and yields precise age control for this interval. Down to 150 mbsf the magnetostratigraphy is interrupted by several significant hiatuses that limit the successful correlation of the magnetozones to the GPTS. However, the age model proposed is consistent with the diatom biostratigraphy of this interval. Below 140 mbsf the accumulation rate apparently was quite rapid, but the correlation to the GPTS is more uncertain and needs further study.

IGNEOUS PETROLOGY

General Description

Basalt at Site 907 was penetrated at about 217 mbsf. Almost 8 m of basalt was cored and 4.9 m was recovered. At 216.8 mbsf fragmental and vesicular basalt was found in a light-green, clay-rich mud. The basalt fragments are angular to well-rounded. Lower in Section 151-907A-24X-CC at 20–53 cm, the mud is a darker green, and at least one microbreccia is present (at 22–27 cm, Fig. 21). It is difficult to determine if the breccias and rubble in Core 151-907A-24X were formed by explosive activity when the basaltic magma extruded into cold seawater or if the breccia is an artifact of drilling. The upper green mud was analyzed by X-ray diffraction and contains quartz, feldspar, and a clay that is possibly celadonite and/or glauconite. A thin section was made from a small rock fragment (Sample 151-907A-24X-CC, 15–20 cm): basaltic glass is in direct contact with an overlying felsic volcaniclastic, and although most of the basaltic glass is altered, fresh glass remains.

The three cores with basalt (Sections 151-907A-24X-CC, 151-907A-25X-1, -2, -3, and 907A-26X-1, -2) are divided into 12 cooling

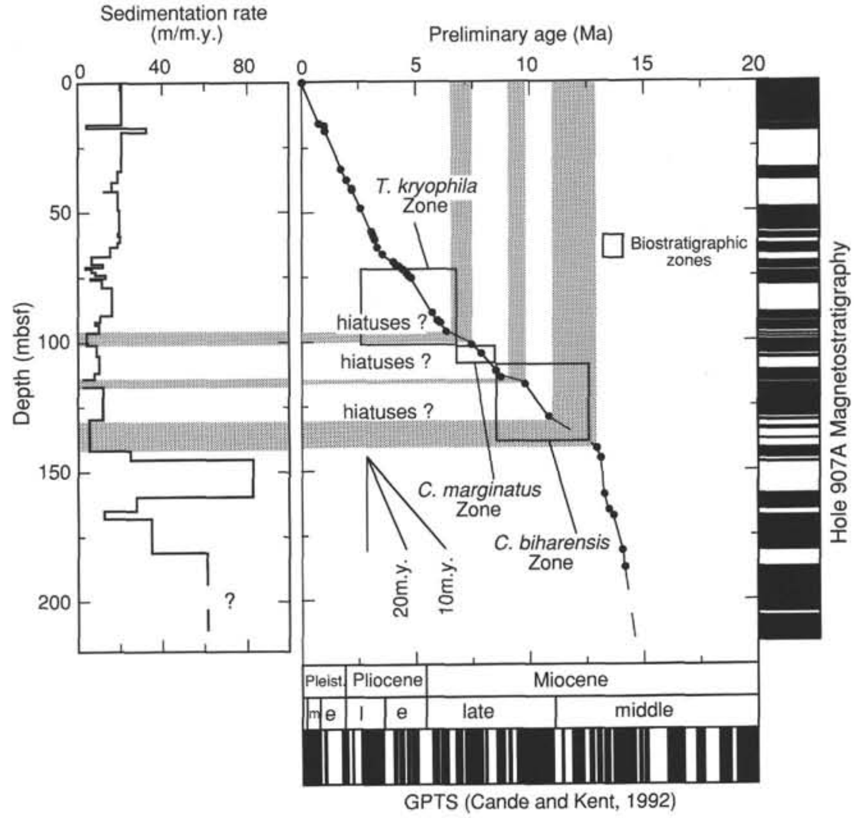

Figure 20. Time-depth diagram of Hole 907A. Biostratigraphic calibration age ranges are indicated by squares.

Table 5. Depth in Hole 907A and preliminary ages deduced from the magnetostratigraphy.

Depth (mbsf)	Age (Ma)	Chron	Depth (mbsf)	Age (Ma)	Chron
0	0		76.05	4.812	
		C1n			C3n.4n
16.15	0.780		78.75	5.046	
17.05	0.984		89.55	5.705	
		C1r.1n			C3An.1n
19.15	1.049		92.25	5.946	
33.85	1.757		93.35	6.078	
		C2n			C3An.2n
38.15	1.983		96.45	6.376	
41.55	2.197		101.35	7.464	
		C2r.1n			C4n.2n
41.95	2.229		105.25	7.892	
49.05	2.600		111.85	8.529	
		C2An.1n			C4An
57.95	3.054		114.55	8.861	
59.35	3.127		117.05	9.777	
		C2An.2n			C5n.2n
61.25	3.221		129.75	10.834	
63.25	3.325		141.85	12.941	
		C2An.3n			C5AAn
66.85	3.553		145.65	13.094	
69.95	4.033		159.65	13.263	
		C3n.1n			C5ABn
71.15	4.134		165.55	13.476	
71.65	4.265		168.05	13.674	
		C3n.2n			C5ACn
72.75	4.432		181.45	14.059	
74.25	4.611		187.85	14.164	
		C3n.3n			C5ADn
75.35	4.694				

units distinguished by glassy, vesicle-, and amygdule-rich rinds. No sedimentary material is interspersed with the basalt, aside from at the top of Core 151-907A-24X-CC, and some pieces of core have glassy sides. In general, glassy rinds grade into very fine-grained chill zones approximately 1–2 cm thick, which then grade into massive and aphyric centers where microphenocrysts of plagioclase, clinopyroxene, and sometimes altered olivine are present. Vesicles and amygdules are found on either side of the glassy portions and generally increase in abundance toward the glass. Figure 22 shows one of the better-developed, glassy chill zones with a fingering of coarser, darker material and amygdules toward the glass on either side. Lineation of tabular plagioclase microphenocrysts is not observed, with the exception of local trachytic patches in Unit 5 (thin section only). Based on the above observations, the cooling units are individual basalt pillows, with tops, bottoms, and sides defined by glassy, vesicle-rich chill zones.

The alteration of these basalts is essentially restricted to the glassy mesostasis, olivine, and some plumose clinopyroxene. However, the deepest core at Hole 907A contains pyrite- and chalcopyrite-bearing veinlets and amygdules. Some of the pyrite-bearing amygdules are filled with quenched glass, skeletal plagioclase, and skeletal iron oxide minerals enclosing large pyrite grains (Fig. 23). These may represent an immiscible sulfide melt fraction. Only one carbonate vein is present, and no carbonate was identified in thin section.

Petrography

Using the classification scheme presented in Williams et al. (1982, p. 96), in particular the textural and mineralogical characteristics, the basalts from Hole 907A can be classified as olivine tholeiites/tholeiitic olivine basalts. Polished thin sections from all units except Unit 8 were examined and described. Macroscopically, the pillows are similar, differing only in diameter and amount of vesicles or amygdules. The rocks are aphyric, but do contain plagioclase, altered olivine, and clinopyroxene microphenocrysts.

Most sections are from pillow centers, but the glassy rinds of some pillows also were examined. Microscopically, the pillows differ in degree of alteration and texture, ranging from vitrophyric to subophitic, with amygdules and glomerocrysts (Fig. 23). Almost all glassy mesostasis has been replaced by brown fibrous material

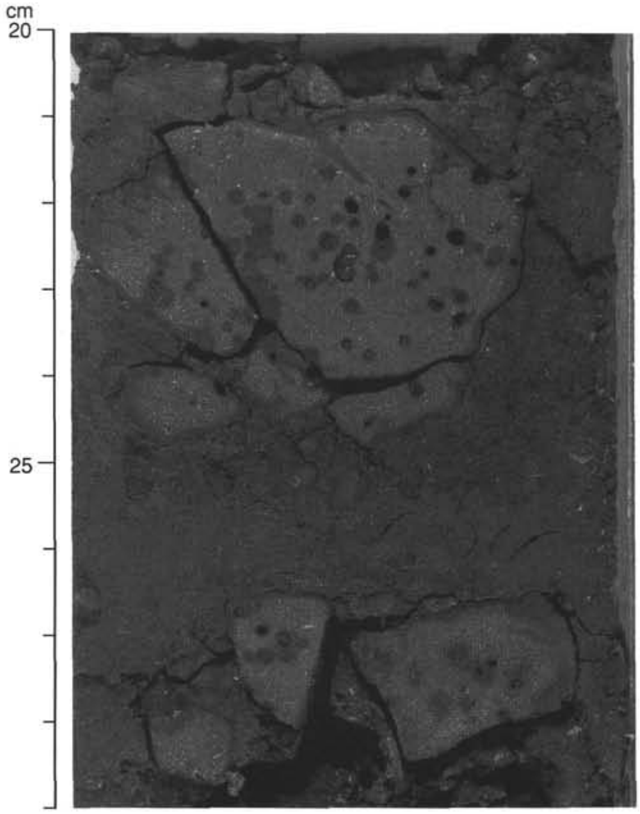

Figure 21. Fragmented and brecciated basalt in Section 151-907A-24X-CC, at 20–29 cm.

(palagonite). In general, the grain size remains the same throughout the 12 units, with microphenocrysts rarely exceeding 1.5 mm in length. The abundance of plagioclase microphenocrysts ranges from <1% to 12% (volume %), whereas clinopyroxene ranges from <1% to 5%, and the abundance of altered olivine microphenocrysts remains constant and <1%. Olivine microphenocrysts are not always present. Glomeroporphs of plagioclase and clinopyroxene ± altered olivine are not uncommon, and in Sample 151-907A-26X-1, 85–89 cm, the pyroxene and plagioclase glomeroporphs appear xenolithic, although they are perhaps cognate.

Groundmass varies considerably throughout the 12 pillows. Aside from the vitrophyres, the amount of glass ranges from 5% to 35%, and plagioclase ranges from 5% to 40%. The amount of clinopyroxene ranges from 15% to 50%, but this is complicated by the apparent alteration of pyroxene to a fine-grained material that may be pyroxene or amphibole. Iron oxide minerals are present in the groundmass of all the pillows. Based solely on habit, magnetite and ilmenite are present in most of the samples; however, the more altered rocks appear to have less ilmenite in that the skeletal iron oxide grains are distinctly less abundant. Identification of groundmass constituents and estimation of relative abundances were difficult in part because of the variolitic texture with accompanying alteration, and in part because of the inability to obtain good interference figures on small anhedral grains using the microscopes available on board ship. Only one pyroxene was identified, but it occurs in two different habits within the groundmass—small, equant, euhedral grains, and plumose radiating sheaves. Therefore, possibly two pyroxenes are present. The altered olivine is difficult to distinguish from altered intersertal glass, but some altered olivine retains a euhedral outline, and circular or oval grains, completely altered to brown fibrous clay with a dark rim, are interpreted to be groundmass olivine.

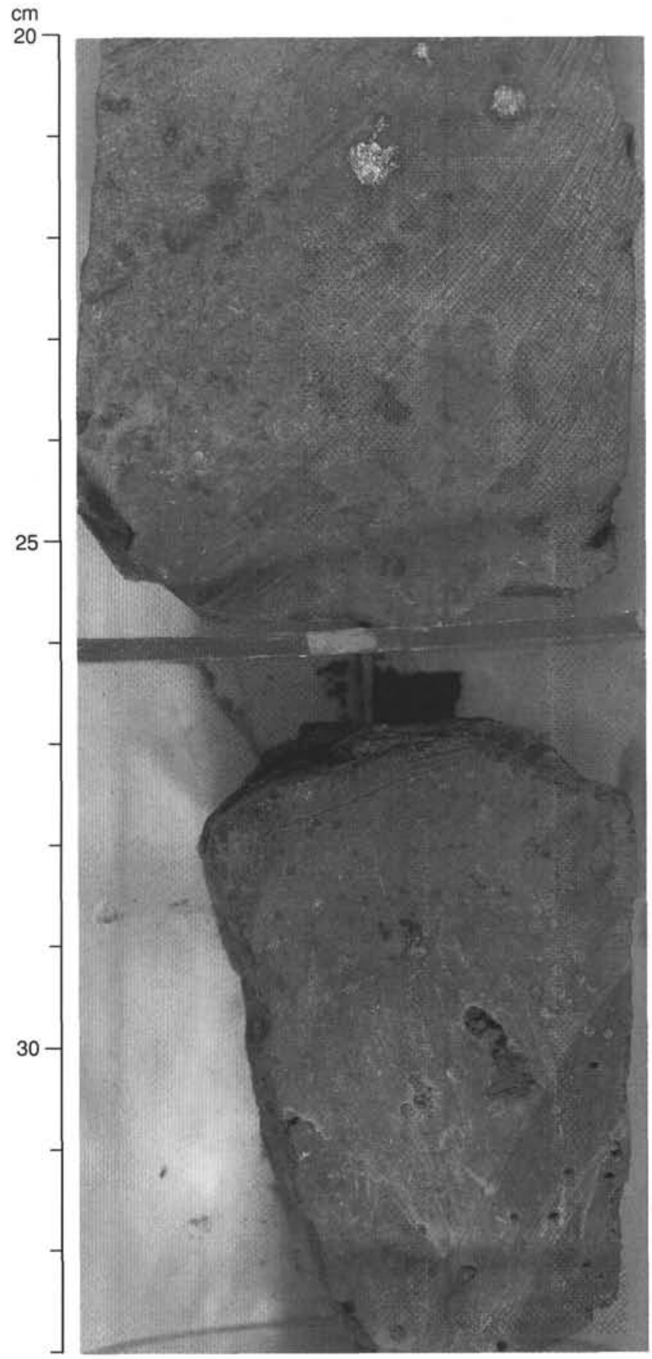

Figure 22. Photograph of the glassy, vesicle- and amygdule-rich rinds of two pillow basalts, interval 151-907A-25X-1, 20–33 cm. Note the change in color and grain size, and note the "fingering" of one zone into the next at about 27–30 cm.

Geochemistry

The chemical compositions of the pillows cored at Site 907 (Table 6) fall within the basalt field of Cox et al. (1979), with SiO_2 content from about 49 to 52 wt%, and Mg from 48 to 52 wt% (Mg = bulk rock $100[Mg/(Mg + Fe^{2+})]$). The basalt compositions also fall well within the tholeiitic basalt field defined by Macdonald and Katsura (1964) (Fig. 24). The rocks contain between 0.4 and 5.0 wt% normative quartz, 26 to 30 wt% normative hypersthene.

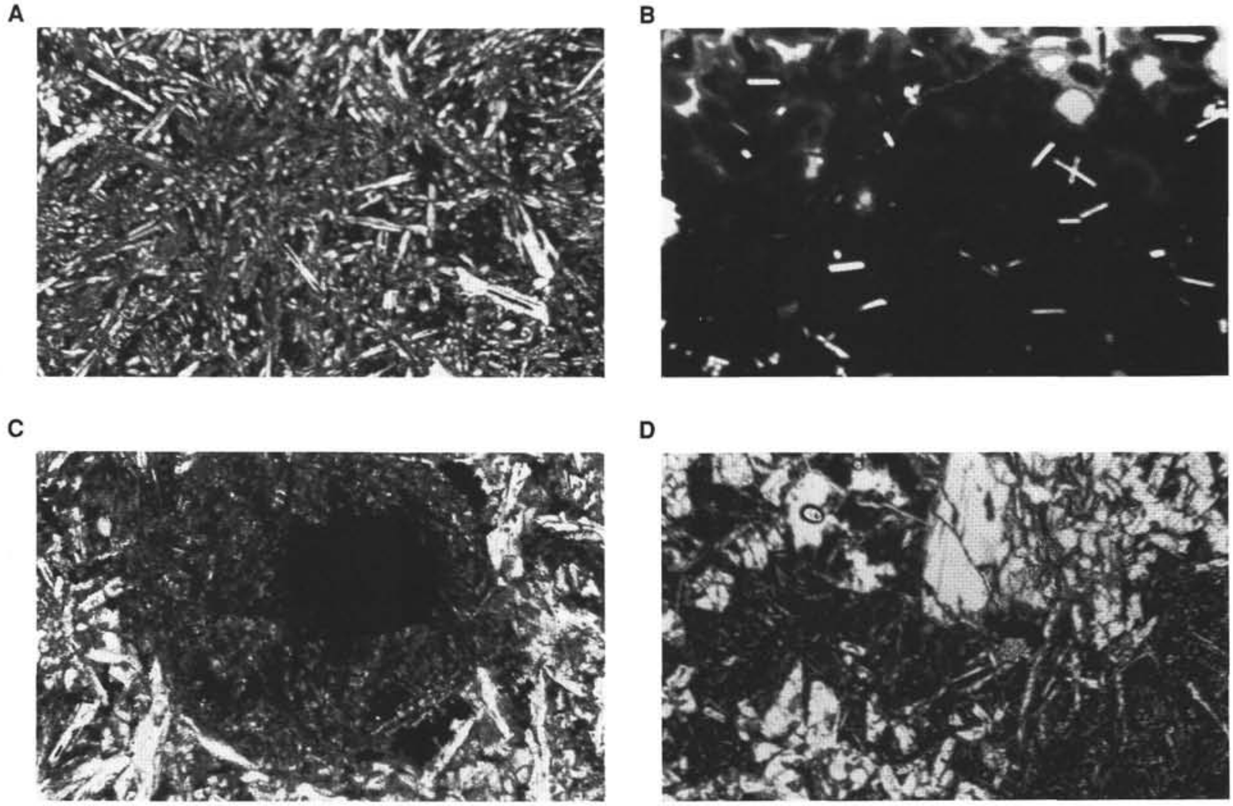

Figure 23. Photomicrographs of basalt textures. **A.** Subophitic, with radiating sheaves of plagioclase and clinopyroxene; Sample 151-907A-25X-2, 73–77 cm, Piece 7B. **B.** Vitrophyric, with glass, spherulites, and plagioclase microphenocrysts; Sample 151-907A-24X-CC, 15–20 cm, Piece 1. **C.** Pyrite in a round amygdule with quenched feldspar and an iron oxide mineral; Sample 151-907A-25X-2, 73–77 cm, Piece 7B. **D.** Clinopyroxene and plagioclase poikilitically intergrown and glomerocrysts of plagioclase and clinopyroxene; Sample 151-907A-25X-2, 142–145 cm, Piece 13. Scale: field of view for (A) and (D) is about 2.5 mm; field for (B) is about 6 mm; field for (C) is about 1.5 mm.

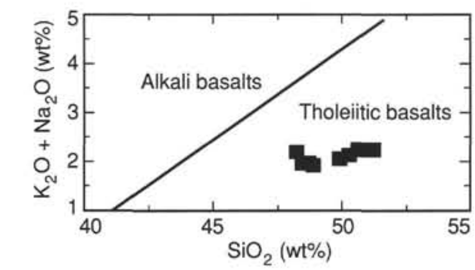

Figure 24. Composition of Site 907 basalts compared with tholeiitic and alkali basalt fields defined by Macdonald and Katsura (1964).

Even though the range in SiO_2 content is small, the pillow basalts show coherent trends in variation diagrams (Fig. 25). Samples 151-907A-26X-1, 35–38 cm, and -26X-2, 6–11 cm, are different in K_2O content from the rest of the samples, and one of these two is quite different with respect to CaO, and P_2O_5 (Table 6, Fig. 25).

Ratios of some of the more incompatible elements with respect to melting of mantle material are nearly constant for the samples analyzed, with the exception of Sample 151-907A-26X-2, 6–11 cm (Table 6). The ratio Na/Ti is about 0.75, Na/P ranges from 21.5 to 23.2, and P/Ti is 0.03 to 0.04. Sample 151-907A-26X-2, 6–11 cm, is the exception with distinctly lower Na/Ti and Na/P.

Summary

The crystalline rocks recovered from Site 907 are quenched pillow basalts and can be classified mineralogically, texturally, and compositionally as tholeiitic basalts to tholeiitic olivine basalts. The quenched glass and skeletal crystals indicate that the basalt was extruded into cold water. The presence of vesicles suggests a water depth of less than 500 mbsl, but this is a very rough estimate based on Moore (1970) and Moore and Schilling (1973) as discussed by Fisher and Schmincke (1984, pp. 38–43). Trace element and isotopic data are needed to fully evaluate the petrogenesis of these rocks and the nature of their mantle sources. They are similar to normal and plume mid-ocean-ridge basalts (N-MORBs and P-MORBs), but the extremely low K_2O contents are most similar to N-MORB (Schilling et al., 1983). The Al_2O_3 contents of the Iceland Plateau pillow basalts are distinctly lower, and the TiO_2 contents are significantly higher than in MORB; Al_2O_3 and TiO_2 are more similar to ocean island basalts (Basaltic Volcanism Study Project, 1981), indicating a component of mantle plume material in the source regions of the Iceland Plateau basalts.

INORGANIC GEOCHEMISTRY

Interstitial Water

Table 7 gives the results of interstitial water analyses in Hole 907A. Cation values show clear trends, with potassium and magnesium decreasing and calcium increasing with depth (Fig. 26). These are typical profiles indicating that the entire pore-water column is in diffusive contact with the volcanic rocks at the bottom of Hole 907A. The basalts take up potassium and magnesium and release calcium during alteration. Ammonia shows a maximum at 60 to 90 mbsf (Fig. 26) and indicates that the diagenesis of organic matter has consumed oxygen and released ammonia, which is diffusing downward proba-

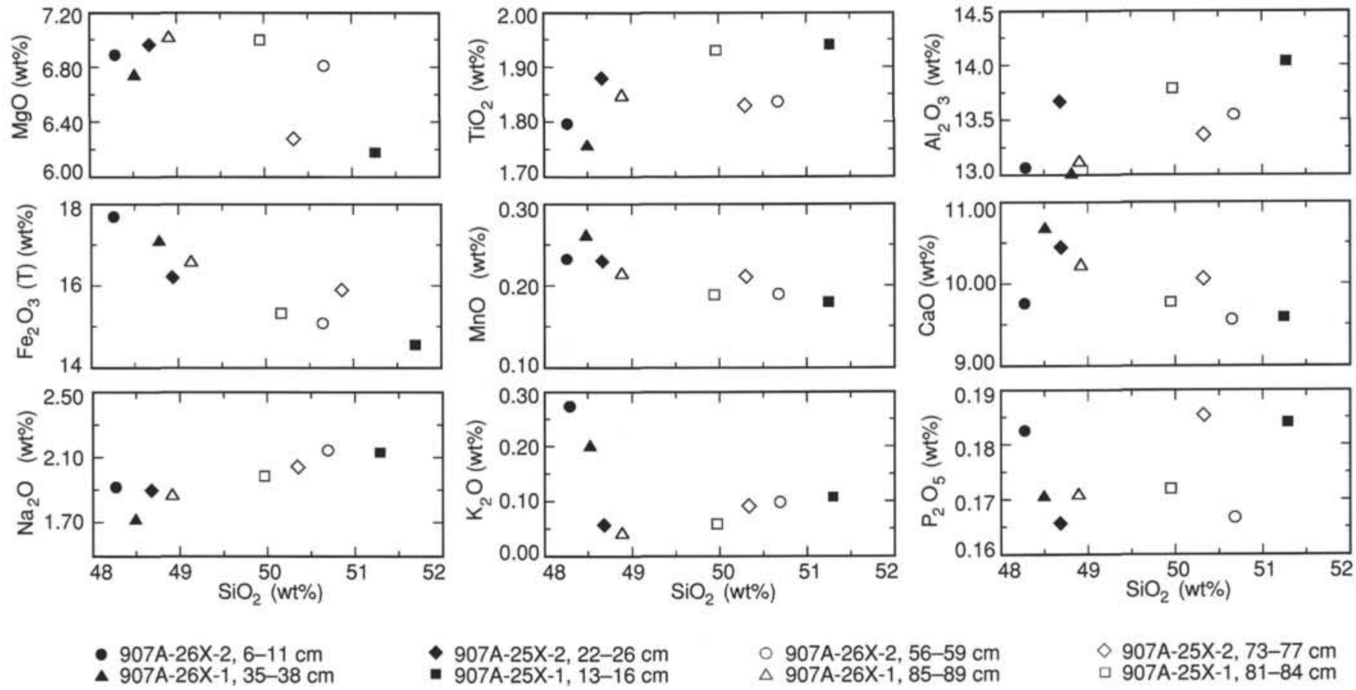

Figure 25. Harker variation diagrams illustrating compositional changes within the analyzed pillow basalts. Analyses are normalized to 100 on a volatile-free basis.

Table 6. Whole-rock analyses of pillow basalts at Site 907.

Sample:	25X-1, 13–16 cm	25X-1, 81–84 cm	25X-2, 22–26 cm	25X-2, 73–77 cm	26X-1, 35–38 cm	26X-1, 85–89 cm	26X-2, 6–11 cm	26X-2, 56–59 cm
SiO_2	51.7	50.2	49.0	50.9	48.8	49.2	48.7	50.8
TiO_2	1.96	1.94	1.89	1.85	1.77	1.86	1.81	1.84
Al_2O_3	14.2	13.9	13.8	13.5	13.0	13.2	13.2	13.6
Fe_2O_3(T)	14.6	15.3	16.2	15.8	17.1	16.6	17.8	15.1
MnO	0.18	0.19	0.23	0.21	0.26	0.22	0.23	0.19
MgO	6.22	7.01	7.00	6.34	6.81	7.07	6.94	6.82
CaO	9.66	9.80	10.5	10.1	10.7	10.3	9.83	9.56
Na_2O	2.14	1.99	1.92	2.06	1.76	1.90	1.93	2.15
K_2O	0.11	0.06	0.05	0.09	0.20	0.04	0.27	0.10
P_2O_5	0.19	0.17	0.17	0.19	0.17	0.17	0.18	0.17
Total	100.96	100.56	100.76	101.04	100.67	100.56	100.89	100.33
LOI	0.62	0.52	0.59	0.31	0.19	0.35	0.46	0.56
Recalculated								
FeO	11.1	11.7	12.4	12.1	13.1	12.7	13.6	11.5
Fe_2O_3	1.97	2.06	2.18	2.14	2.31	2.24	2.40	2.03
Total with LOI	99.99	99.5	99.6	99.9	99.1	99.2	99.5	99.3
mbsf	217.43	218.11	218.90	219.41	221.35	221.85	222.50	223.00
Na/Ti	0.76	0.73	0.75	0.79	0.78	0.76	0.66	0.72
Na/P	22.1	22.6	23.2	21.5	22.1	22.6	17.9	21.8
P/Ti	0.03	0.03	0.03	0.04	0.04	0.03	0.04	0.03
mg	50	52	50	48	48	50	48	51

Notes: Major elements determined by XRF on fused glass disks. Na_2O also obtained from non-ignited pressed-powder pellets. Sample preparation and analytical techniques are discussed in the "Explanatory Notes" chapter, this volume. Analysts: W. Autio and K. Kuroki. Fe_2O_3 is calculated as 0.15^* FeO (Total) following Basaltic Volcanism Study Project (1981). Precision based upon the standard deviation of replicate analyses of International Standard BIR is as follows: SiO_2, 0.02; TiO_2 and Al_2O_3, 0.01; Fe_2O_3, 0.06; MgO and CaO, 0.04 and 0.06; MnO, K_2O, Na_2O, and P_2O_5 are 0.00. The SiO_2 content is consistently 0.4 wt% lower than the accepted value for Standard BIR. LOI = loss on ignition.

Table 7. Composition of interstitial waters in Hole 907A.

Core, section, interval (cm)	Depth (mbsf)	Sodium (mmol/L)	Potassium (mmol/L)	Magnesium (mmol/L)	Calcium (mmol/L)	Chloride (mmol/L)	Sulfate (mmol/L)	Silica (μmol/L)	Ammonia (μmol/L)	pH	Alkalinity (meq/L)
151-907A-											
1H-2, 145–150	2.95	495	11.87	48.7	12.9	544	28.6	209	22.3	7.46	2.883
4H-4, 145–150	32.25	498	10.78	34.1	31.8	553	24.2	215	74.6	7.70	2.577
7H-5, 145–150	62.25	438	10.23	24.5	38.4	551	24.3	535	83.8	8.02	2.107
10H-5, 145–150	90.75	529	10.85	22.2	43.7	554	26.6	622	84.5	8.07	2.079
13H-5, 145–150	119.25	491	9.09	19.7	48.9	553	31.1	755	75.7	7.44	1.818
16H-5, 145–150	147.75	461	9.15	16.8	51.7	552	24.7	927	70.4	7.83	1.441
19H-5, 145–150	176.25	482	7.91	16.0	58.5	555	24.5	1099	55.9	7.33	1.213
22H-5, 145–150	204.75	532	7.15	14.1	60.3	558	22.1	255	52.1	7.81	1.105

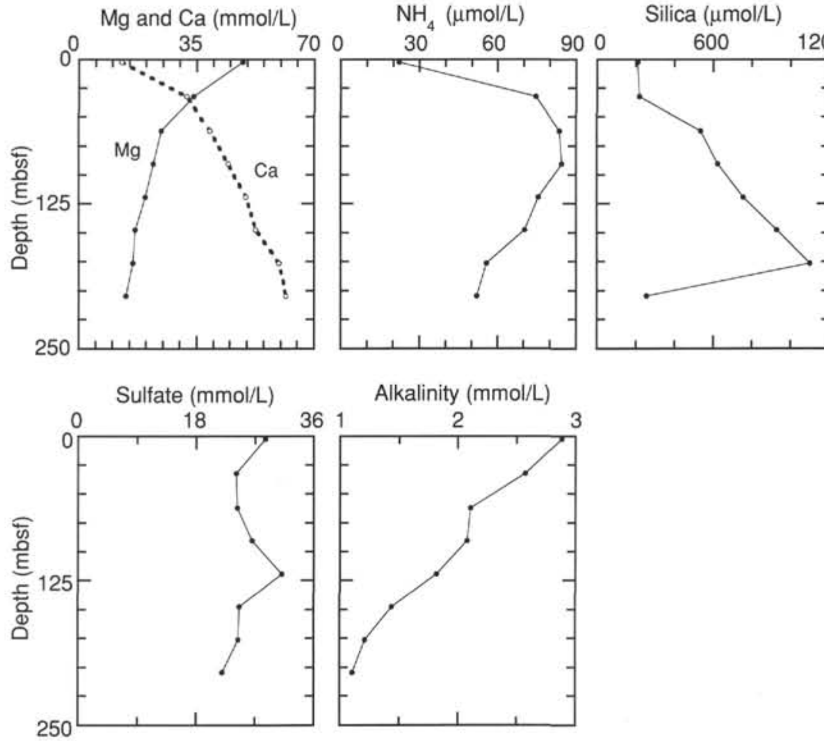

Figure 26. Interstitial water compositions at Site 907.

bly into interlayer sites in clays and upward to the sediment-water interface where it reacts with oxygen.

Chloride shows little variation with depth, but silica (Fig. 26) increases from 209 µmol/L at 2.95 mbsf to 1099 µmol/L at 176.25 mbsf, then decreases sharply to 255 µmol/L in the lowest sample (Core 22H at 204.5 mbsf). The high silica levels are probably caused by the dissolution of the abundant siliceous fossils in the middle-lower parts of the hole.

Sulfate (Fig. 26) shows anomalous behavior. The abundance of ammonia clearly shows the lack of oxygen in these pore waters. Organic matter in these cores appears to be sufficient to support sulfate reduction (see "Organic Geochemistry" section, this chapter), but sulfate is not diminished and, in fact, reaches a modest maximum in Core 13H at 119.25 mbsf. This phenomenon is unexplained but may indicate supply of sulfate from below associated with the high geothermal gradient measured in the hole (see "Physical Properties" and "Downhole Measurements" sections, this chapter).

Alkalinity shows an interesting distribution (Fig. 26), decreasing steadily with depth in what appears to be a diffusive profile indicating steady uptake of alkalinity by the basalts in the bottom of the hole. (It should be noted that alkalinity does not diffuse; bicarbonate and carbonate ions do. Because the alkalinity is dominated by bicarbonate ions at these pHs, it is only mildly inaccurate to discuss the diffusion of alkalinity). An alternative explanation is that this represents equilibrium with calcium carbonate minerals and is imposed by the distribution of calcium. A preliminary calculation of the ion molal product (IMP) of calcium and carbonate indicates a near constancy of IMP with depth. On the other hand, any significant sink of alkalinity within the column should cause a more pronounced curvature of the alkalinity profile. In addition, carbonate measurements on the sediments in Hole 907A (see Fig. 28 and Table 8) show no evidence for substantial precipitation of carbonate.

Sediment Geochemistry

The carbonate concentrations in sediments from Hole 907A are shown in Table 8 and Figure 28. Major element abundances are shown in Table 9. Major elements behave in predictable ways in these sediments. CaO is variable and represents variations in calcium carbonate abundances (Fig. 27, compare with Fig. 28). Similarly, the sum of the oxides is generally less than 100%, and the deficiency varies with the CaO content, reflecting the inability of the X-ray fluorescence (XRF) to detect either C or O in carbonates. K_2O/Al_2O_3 and Al_2O_3/SiO_2 ratios are nearly constant throughout (Fig. 27), indicating that the detrital fraction varies little in composition and that illite (or mica)/quartz and K-feldspar/quartz ratios are constant or compensating.

Iron and manganese show a double trend (Fig. 27). In some samples MnO increases independently of iron (total iron is reported here as Fe_2O_3), which remains nearly constant indicating the precipitation of hydrogenous manganese oxides (probably as micronodules). In other samples, iron varies independently of MnO and shows a trend toward the composition of basalts from Core 151-907A-25X, suggesting the admixture of volcanic ash or glass. No attempt has been made here to compare the Fe_2O_3 abundance to ash abundance data.

Magnesium and calcium concentrations fall in the range 2%–4% MgO and 2%–10% CaO (Fig. 27). Basalts contain a relatively constant 10% CaO and MgO varying from about 6% to 7.5%. The trend toward basaltic values noted above for iron does not appear in these data. Phosphorus shows a clear trend increasing with MnO content (Fig. 27).

In general, the compositions of these sediments reflect the dominance of the clastic component. Some variations are a result of calcium carbonate variations, hydrogenous manganese oxide precipitation, and the admixture of volcanic ash or glass. No compositional gradients occur to suggest substantial chemical exchange with the basalts at the bottom of Hole 907A.

Discussion

The composition of sediments in Hole 907A varies little except for carbonate content. The clastic source for these sediments is clearly continental, with K_2O contents above 2% throughout and silica well above 50% in noncarbonate sediments. Although ash and glass are described in Hole 907A (see "Lithostratigraphy" section, this chapter), they do not appear to have much effect on major element

Table 8. Summary of geochemical analyses of sediments in Hole 907A.

Core, section, interval top (cm)	Depth (mbsf)	IC (%)	$CaCO_3$ (%)	TC (%)	TOC (%)	HI (mgHC/gC)	TN (%)	TS (%)	C/N	C/S
1H-1, 27	0.27	1.83	15.20	2.10	0.27	37	0.00	0.01		
1H-1, 100	1.00	0.89	7.40	1.02	0.13		0.00	0.05		2.6
1H-2, 18	1.68	1.77	14.70	2.04	0.27	33	0.00	0.00		
1H-2, 100	2.50	0.06	0.50	0.20	0.14		0.00	0.00		
1H-3, 21	3.21	2.36	19.70	2.45	0.09		0.00	0.00		
1H-3, 99	3.99	2.07	17.20	2.15	0.08					
1H-4, 25	4.75	1.38	11.50	1.41	0.03					
1H-4, 102	5.52	0.12	1.00	0.33	0.21					
1H-5, 26	6.26	1.18	9.80	1.41	0.23	22				
1H-5, 86	6.86	0.18	1.50	0.21	0.03					
2H-1, 24	7.54	0.21	1.70	0.63	0.42	102				
2H-1, 99	8.29	0.07	0.60	0.57	0.50	94				
2H-2, 24	9.04	1.62	13.50	1.66	0.04					
2H-2, 99	9.79	0.18	1.50	0.39	0.21					
2H-3, 24	10.54	2.21	18.40	2.46	0.25	32				
2H-3, 99	11.29	0.10	0.80	0.00	0.00					
2H-4, 24	12.04	0.46	3.80	0.58	0.12					
2H-4, 99	12.79	0.36	3.00	0.62	0.26	150				
2H-5, 24	13.54	1.63	13.60	1.76	0.13					
2H-5, 99	14.29	0.16	1.30	0.41	0.25	212				
2H-6, 24	15.04	0.85	7.10	0.96	0.11					
2H-6, 99	15.79	1.14	9.50	1.31	0.17					
2H-7, 24	16.54	1.47	12.20	1.66	0.19					
3H-1, 25	17.05	0.04	0.30	0.12	0.08					
3H-1, 98	17.78	0.05	0.40							
3H-2, 25	18.55	0.11	0.90	0.31	0.20					
3H-2, 98	19.28	0.21	1.70							
3H-3, 25	20.05	0.16	1.30	0.35	0.19					
3H-3, 72	20.52	0.12	1.00	0.38	0.26	246				
3H-3, 97	20.77	0.09	0.70							
3H-4, 25	21.55	0.03	0.20	0.31	0.28	154				
3H-4, 97	22.27	0.07	0.60							
3H-5, 25	23.05	0.02	0.20	0.36	0.34		0.00	0.00		
3H-5, 97	23.77	0.08	0.70							
3H-6, 25	24.55	0.03	0.20	0.15	0.12		0.00	0.00		
3H-6, 70	25.00	0.08	0.70	0.53	0.45		0.07	0.00	6.4	
3H-6, 97	25.27	0.12	1.00							
3H-7, 25	26.05	0.03	0.20	0.35	0.32		0.00	0.00		
4H-1, 53	26.83	0.07	0.60	0.19	0.12		0.00	0.00		
4H-1, 101	27.31	0.02	0.20							
4H-2, 102	28.82	0.02	0.20	0.20	0.18		0.00	0.00		
4H-3, 77	30.07	0.02	0.20	0.23	0.21		0.00	0.00		
4H-4, 77	31.57	0.02	0.20	0.36	0.34		0.08	0.00	4.2	
4H-5, 77	33.07	0.02	0.20	0.23	0.21		0.07	0.00	3.0	
4H-6, 78	34.58	0.02	0.20	0.23	0.21		0.00	0.00		
5H-1, 27	36.07	0.02	0.20	0.26	0.24		0.07	0.14	3.4	1.7
5H-2, 27	37.57	0.02	0.20	0.24	0.22		0.00	0.00		
5H-3, 27	39.07	0.01	0.10	0.18	0.17		0.00	0.00		
5H-4, 21	40.51	0.02	0.20	0.37	0.35		0.00	0.00		
5H-5, 24	42.04	0.02	0.20							
5H-6, 23	43.53	0.01	0.10	0.41	0.40		0.07	0.13	5.7	3.1
5H-7, 18	44.98	0.02	0.20							
6H-1, 27	45.57	0.02	0.20	0.73	0.71		0.07	0.07	10.1	10.1
6H-2, 24	47.04	0.21	1.70							
6H-3, 25	48.55	0.03	0.20							
6H-3, 102	49.32	0.06	0.50	0.42	0.36		0.07	0.10	5.1	3.6
6H-4, 23	50.03	0.01	0.10							
6H-5, 28	51.58	0.06	0.50	0.37	0.31	216	0.06	0.00	5.2	
6H-6, 24	53.04	0.02	0.20							
6H-7, 24	54.54	0.02	0.20	0.35	0.33		0.07	0.08	4.7	4.1
7H-1, 24	55.04	0.05	0.40							
7H-2, 23	56.53	0.04	0.30	0.70	0.66		0.00	0.00		
7H-2, 99	57.29	0.02	0.20							
7H-3, 25	58.05	0.06	0.50							
7H-3, 101	58.81	0.12	1.00							
7H-4, 25	59.55	0.02	0.20	0.26	0.24		0.00	0.00		
7H-5, 102	61.82	0.03	0.20							
7H-6, 26	62.56	0.03	0.20	0.31	0.28		0.06	0.10	4.7	2.8
7H-6, 93	63.23	4.03	33.60							
8H-1, 27	64.57	7.44	62.00	7.64	0.20		0.00	0.07		2.9
8H-2, 19	65.99	0.07	0.60	0.21	0.14		0.00	0.00		
8H-3, 20	67.50	0.03	0.20							
8H-4, 21	69.01									
8H-5, 23	70.53	0.03	0.20	0.23	0.20		0.00	0.15		1.3
8H-6, 24	72.04									
8H-7, 26	73.56	0.04	0.30							
9H-1, 25	74.05	0.02	0.20	0.94	0.92	109	0.09	0.80	10.2	1.1
9H-2, 25	75.55									
9H-3, 25	77.05	0.02	0.20	0.31	0.29	221	0.00	0.32		0.9
9H-4, 26	78.56									
9H-5, 26	80.06	0.02	0.20	0.24	0.22		0.00	0.13		1.7
9H-6, 100	82.30	0.02	0.20							
9H-7, 26	83.06									
10H-1, 99	84.29	0.02	0.20	0.42	0.40		0.07	0.10	5.7	4.0
10H-2, 98	85.78									
10H-3, 24	85.54	0.02	0.20	0.79	0.77	110	0.07	0.15	11.0	5.1
10H-4, 22	88.02									
10H-5, 46	89.76	0.03	0.20	0.72	0.69		0.00	0.13		5.3

Table 8 (continued).

Core, section, interval top (cm)	Depth (mbsf)	IC (%)	$CaCO_3$ (%)	TC (%)	TOC (%)	HI (mgHC/gC)	TN (%)	TS (%)	C/N	C/S
10H-6, 23	91.03									
10H-6, 97	91.77	0.03	0.20							
11H-1, 22	93.02	0.03	0.20	0.19	0.16		0.00	0.18		0.9
11H-2, 17	94.47	3.13	26.10							
11H-3, 22	96.02	0.04	0.30	0.31	0.27		0.00	0.15		1.8
11H-4, 20	97.50	0.03	0.20							
11H-5, 123	100.03	0.04	0.30	0.13	0.09		0.00	0.09		1.0
11H-6, 116	101.46	0.03	0.20							
12H-1, 28	102.58	0.03	0.20	0.28	0.25		0.07	0.12	3.6	2.1
12H-2, 28	104.08	0.02	0.20							
12H-3, 27	105.57	0.04	0.30	0.71	0.67	242	0.10	0.31	6.7	2.2
12H-4, 27	107.07	0.02	0.20							
12H-5, 28	108.58	0.03	0.20	0.55	0.52		0.09	7.30	5.8	0.1
13H-1, 26	112.06	0.03	0.20	0.21	0.18		0.00	0.00		
13H-3, 84	115.64	0.02	0.20	0.54	0.52	294	0.08	0.40	6.5	1.3
13H-4, 25	116.55	0.02	0.20							
13H-5, 111	118.91	0.02	0.20	0.24	0.22		0.00	0.20		1.1
13H-6, 26	119.56	0.02	0.20							
13H-7, 26	121.06	0.03	0.20	0.23	0.20		0.00	0.56		0.4
14H-1, 26	121.57	0.02	0.20	0.21	0.19		0.00	0.40		0.5
14H-3, 26	124.56	0.03	0.20	1.08	1.05	116		0.79		1.3
14H-5, 125	128.55	0.02	0.20	0.67	0.65		0.09	0.37	7.2	1.8
15H-1, 27	132.04	0.02	0.20	0.37	0.35		0.06	0.44	5.8	0.8
15H-3, 24	134.04	0.02	0.20	0.35	0.33	418	0.06	0.36	5.5	0.9
16H-1, 22	140.52	0.02	0.20	0.16	0.14		0.00	0.37		0.4
16H-3, 22	143.52	0.02	0.20	0.23	0.21		0.00	0.60		0.3
17H-1, 27	150.07	0.02	0.20	0.30	0.28		0.00	0.78		0.4
17H-4, 27	154.57	0.02	0.20	0.42	0.40		0.07	0.70	5.7	0.6
18H-1, 27	159.57	0.02	0.20	0.32	0.30		0.00	0.53		0.6
18H-3, 25	162.55	0.02	0.20	0.19	0.17		0.00	0.20		0.9
19H-2, 26	170.56	0.02	0.20	0.71	0.69		0.08	0.95	8.6	0.7
19H-4, 26	173.56	0.02	0.20	1.29	1.27	98	0.09	1.82	14.1	0.7
19H-6, 103	177.33	0.02	0.20	0.96	0.94	207	0.11	2.75	8.5	0.3
20H-1, 25	178.55		0.20	1.82	1.80		0.13	2.48	13.8	0.7
20H-3, 26	181.56	0.03	0.20	0.68	0.65	183	0.08	0.86	8.1	0.8
20H-6, 27	186.07	0.03	0.20	0.60	0.57	230	0.07	0.76	8.1	0.8
21H-1, 25	188.05	0.02	0.20							
21H-3, 25	191.05	0.02	0.20	0.60	0.58	259		1.10		0.5
21H-5, 25	194.05	0.02	0.20	0.65	0.63		0.07	0.85	9.0	0.7
22H-1, 26	197.56	0.02	0.20	0.53	0.51			0.43		1.2
22H-3, 26	200.56	0.02	0.20	0.81	0.79	111	0.07	0.86	11.3	0.9
22H-5, 27	203.57	0.02	0.20	0.86	0.84		0.07	0.27	12.0	3.1
22H-7, 25	206.55	0.02	0.20	0.84	0.82	118	0.07	0.94	11.7	0.9
23H-1, 27	207.07	0.02	0.20	0.68	0.66		0.06	0.43	11.0	1.5
23H-3, 27	210.07	0.03	0.20	0.67	0.64	127	0.07	0.94	9.1	0.7
23H-5, 27	213.07	0.04	0.30	0.89	0.85	94	0.09	1.82	9.4	0.5
23H-6, 27	214.57	0.02	0.20	0.57	0.55	129		0.72		0.8

Notes: IC = inorganic carbon; $CaCO_3$ = carbonate; TC = total carbon; TOC = total organic carbon; HI = hydrogen index values; TN = total nitrogen, TS = total sulfur; C/N = total organic carbon/total nitrogen ratios; C/S = total organic carbon/total sulfur ratios.

distribution patterns except perhaps for iron. Manganese is mobile in these cores, migrating to redox fronts and coprecipitating with P_2O_5.

Although the sediment composition shows little variation, the interstitial-water chemistry suggests an active process in Hole 907A. Both the calcium and the magnesium profiles show substantial concave downward curvature (Fig. 26), suggesting that either the diffusivity is increasing downward (requiring, as a consequence, steeper profiles near the top of the hole where the diffusivity is low) or the pore waters in Hole 907A are advecting upward. Similarly, the ammonia profile demonstrates the lack of oxygen in the sediments, but the continued existence of sulfate in the hole suggests a source from below. In addition, temperature gradients are anomalously high and appear to be higher in the upper part of Hole 907A than in the lower part; this also suggests upward advection.

The meaning of the alkalinity profile in Hole 907A is uncertain. If the pore waters at this site are not advecting, then alkalinity is clearly diffusing into the basalts. More likely, pore waters are advecting upward and the alkalinity of this water has been reduced by reaction with basalts.

ORGANIC GEOCHEMISTRY

The shipboard organic geochemistry program at Site 907 consisted of analyses of volatile hydrocarbons; determinations of inorganic carbon, total nitrogen, total carbon, and total sulfur; and pyrolysis measurements (for methods see "Explanatory Notes" chapter, this volume).

Volatile Hydrocarbons

As part of the shipboard safety and pollution monitoring program, concentrations of methane (C_1) and ethane (C_2) gases were monitored every core using standard ODP headspace-sampling technique. Throughout the entire sediment sequence of Site 907, the methane content remained constantly low (4–5 ppm). Ethane was not detected.

Carbon, Nitrogen, and Sulfur Concentrations

The results of determinations of inorganic carbon, carbonate, total carbon, total nitrogen, and total sulfur are summarized in Table 8 and presented in Figures 28 and 29.

According to the carbonate data (calculated from the inorganic carbon content assuming that all carbonate occurs as calcite), the sediment sequence of Site 907 can be divided into two intervals (Fig. 28). The upper interval (0–16.8 mbsf; Holocene to middle Pleistocene age), which corresponds to lithologic Unit I, is characterized by variations of carbonate percentages ranging between 1% and 20%. These short-term, high-amplitude variations are similar to those re-

Table 9. Major element composition of sediments in Hole 907A.

Core, section	Depth (mbsf)	SiO_2 (wt%)	TiO_2 (wt%)	Al_2O_3 (wt%)	Fe_2O_3 (wt%)	MnO (wt%)	MgO (wt%)	CaO (wt%)	Na_2O (wt%)	K_2O (wt%)	P_2O_5 (wt%)	Total (wt%)
151-907A-												
1H-1	0.25	52.69	1.06	12.63	7.01	0.17	3.36	7.01	3.24	2.44	0.23	89.86
1H-2	1.67	53.37	1.03	14.46	7.21	0.23	3.45	6.14	2.50	2.82	0.26	91.47
1H-3	3.20	54.27	0.87	13.93	6.31	0.20	3.10	6.64	2.53	2.74	0.21	90.79
1H-4	4.74	55.52	0.89	14.16	6.85	0.27	3.50	5.14	2.33	2.97	0.21	91.83
1H-5	6.24	56.93	0.92	13.61	7.00	0.09	3.21	4.95	2.46	2.90	0.30	92.36
2H-1	7.56	60.28	0.92	15.00	6.67	0.10	3.14	2.44	2.43	2.95	0.21	94.14
2H-3	10.54	50.50	1.04	14.12	6.70	0.18	3.17	7.96	2.90	2.80	0.19	89.56
2H-5	13.54	54.30	0.94	14.24	6.59	0.13	2.95	5.05	2.84	3.01	0.18	90.23
2H-7	16.54	48.69	1.27	13.87	7.77	0.15	3.14	7.08	3.16	2.60	0.23	87.95
3H-1	17.04	60.49	0.93	14.57	7.53	0.09	3.33	1.96	2.50	3.01	0.17	94.57
3H-3	20.04	61.46	0.95	15.42	6.66	0.21	2.98	2.10	2.72	3.29	0.17	95.96
3H-5	23.04	65.52	0.80	13.86	5.75	0.05	2.11	1.72	2.31	2.89	0.24	95.25
3H-4	26.04	57.72	1.05	15.22	8.67	0.08	3.11	2.06	2.62	3.51	0.20	94.24
4H-1	26.83	62.53	0.92	14.45	6.54	0.08	2.97	1.96	2.53	3.25	0.16	95.39
4H-3	29.52	61.07	0.93	16.42	6.67	0.07	2.96	1.90	2.67	3.40	0.13	96.22
4H-5	32.52	61.47	0.90	13.67	6.56	1.57	2.91	2.16	2.23	3.16	0.15	94.78
4H-7	35.75	62.60	0.91	16.03	6.48	0.05	2.72	1.86	2.86	3.20	0.14	96.85
5H-1	36.05	60.10	0.93	15.55	8.41	0.07	2.99	1.93	2.56	3.34	0.14	96.01
5H-3	39.04	61.35	0.88	15.95	7.55	0.06	2.88	1.84	2.39	3.49	0.14	96.54
5H-5	42.03	60.63	1.00	17.17	7.40	0.06	2.94	1.96	2.41	3.40	0.12	97.10
5H-7	44.97	56.72	1.46	17.16	8.67	0.09	3.26	2.87	3.33	2.96	0.15	96.68
6H-1	45.57	61.56	0.90	15.55	7.63	0.06	2.74	1.87	2.36	3.45	0.15	96.26
6H-3	48.55	59.68	1.17	16.71	7.79	0.07	3.03	2.24	2.88	3.12	0.13	96.82
6H-5	51.54	61.26	0.93	16.56	7.03	0.06	2.95	1.94	2.60	3.22	0.14	96.69
6H-7	54.55	59.31	1.08	16.63	7.93	0.07	2.99	2.14	2.78	3.09	0.12	96.15
7H-1	55.04	58.67	1.17	16.21	7.49	0.08	3.24	2.79	3.37	2.85	0.15	96.02
7H-3	58.04	57.38	1.15	16.22	8.05	0.08	3.15	2.39	2.98	2.91	0.13	94.43
7H-5	61.05	54.13	1.42	13.84	10.00	0.13	3.55	3.15	3.74	2.73	0.18	92.87
7H-7	64.05	49.47	1.05	11.01	6.73	0.12	2.35	9.62	2.87	2.39	0.14	85.75
8H-1	64.58	23.79	0.44	4.49	3.89	0.23	0.66	34.43	1.13	1.17	0.54	70.76
8H-3	67.50	55.15	1.24	11.58	11.31	0.08	3.53	2.56	3.36	2.61	0.15	91.59
8H-5	70.54	53.34	1.36	13.41	10.55	0.06	3.38	2.72	3.54	2.67	0.15	91.18
8H-7	73.57	54.19	1.38	13.51	10.92	0.06	3.18	2.70	3.10	2.81	0.17	92.01
9H-1	74.05	53.58	1.17	13.53	10.06	0.06	3.01	2.50	2.95	2.65	0.14	89.64
9H-3	77.05	56.28	1.47	14.79	9.08	0.09	3.14	3.72	3.33	2.45	0.13	94.48
9H-5	80.30	56.51	1.31	16.11	8.93	0.07	3.31	2.70	3.06	2.88	0.14	95.02
9H-7	83.05	54.06	1.35	12.23	10.88	0.10	3.21	2.91	3.17	2.77	0.17	90.83
10H-1	83.55	54.78	1.32	14.40	9.05	0.08	3.26	2.84	3.99	2.57	0.16	92.47
10H-3	86.55	54.07	1.35	16.45	8.30	0.07	3.21	2.87	3.70	2.65	0.17	92.86
10H-7	92.70	51.91	1.43	16.76	8.17	0.07	3.43	2.97	4.21	2.45	0.15	91.55
11H-1	93.06	55.83	1.22	14.50	9.19	0.11	3.32	2.65	4.29	2.62	0.16	93.88
11H-3	96.04	56.31	1.38	17.73	8.26	0.08	3.33	2.87	4.01	2.57	0.14	96.69
11H-5	99.03	55.57	1.49	14.97	9.37	0.10	3.33	3.29	4.35	2.28	0.14	94.88
11H-7	101.90	57.65	0.97	15.24	7.98	0.09	3.34	2.48	4.68	2.60	0.14	95.16
12H-1	102.60	56.43	1.28	15.91	8.86	0.07	3.61	2.75	4.01	2.54	0.13	95.60
12H-3	105.60	57.85	1.32	16.18	8.26	0.06	3.24	2.53	3.54	2.48	0.10	95.56
12H-5	108.60	58.02	1.23	16.32	8.72	0.05	3.06	2.40	3.62	2.45	0.10	95.98
12H-7	111.50	55.59	1.65	15.88	10.03	0.08	3.22	3.25	3.79	2.31	0.14	95.95
13H-1	112.00	63.30	1.07	13.13	7.40	0.10	2.40	2.71	4.45	2.87	0.17	97.61
13H-3	115.00	55.36	1.57	14.74	9.84	0.11	3.56	4.20	4.06	1.86	0.14	95.44
13H-5	118.00	58.66	1.62	13.98	9.86	0.09	2.90	3.62	3.89	2.29	0.16	97.06
13H-7	121.00	59.24	1.63	13.61	8.98	0.09	3.15	3.80	4.43	1.95	0.16	97.05
14H-3	124.50	61.34	1.52	12.29	8.77	0.07	2.85	3.25	3.56	2.09	0.13	95.87
15H-3	134.00	58.92	1.08	13.88	8.87	0.06	3.00	2.42	3.00	2.73	0.12	94.08
16H-3	143.50	64.82	1.08	11.04	7.79	0.08	2.45	2.83	3.53	2.59	0.16	96.37
17H-3	153.10	62.55	0.94	15.57	6.92	0.04	2.98	2.20	2.63	2.58	0.07	96.46
18H-3	162.60	64.35	1.23	13.38	7.36	0.06	2.94	2.93	3.31	2.43	0.14	98.13
19H-3	172.10	66.24	0.98	11.70	7.46	0.05	2.70	2.47	3.09	2.23	0.11	97.05
20H-3	181.50	60.93	1.13	13.20	7.98	0.06	3.13	2.70	3.01	2.38	0.13	94.65
21H-3	191.10	60.84	1.09	13.18	7.99	0.08	3.33	2.89	3.12	2.53	0.13	95.19
22H-3	200.60	59.63	1.11	13.76	8.01	0.05	4.23	2.30	2.63	2.96	0.11	94.77
23H-3	210.10	58.90	1.19	15.43	7.70	0.04	3.67	2.20	2.56	3.01	0.06	94.74

corded and described in detail in gravity cores from the Norwegian-Greenland Sea (e.g., Henrich et al., 1989a; Nam et al., in press); they probably reflect glacial/interglacial fluctuations. In the lower interval (16.8–214.6 mbsf; early Pleistocene to middle Miocene age), carbonate is nearly absent throughout, with two distinct exceptions. In Sections 151-907A-7H-6 through -8H-1 and Section 151-907A-11H-2, carbonate contents reach maximum values of 34%–62% and 26%, respectively (Fig. 28).

The total organic carbon (TOC) contents vary between 0.05% and 1.80% (Fig. 28). Low values of <0.3% are dominant in the upper 45 mbsf (i.e., the last 2.5 m.y.) and between 130 and 170 mbsf (i.e., about 12 to 13.5 Ma). In the interval between 45 and 130 mbsf, TOC values range from 0.1% to 1%. Maximum TOC values of 0.5% to 1.8% occur in the lowermost part of the sedimentary record of Hole 907A (170–214.6 mbsf; 13.5 to 14.5 Ma).

The total nitrogen contents are generally very low (Table 8, 0% to 0.13%). In the organic-carbon-lean intervals nitrogen values are below the detection threshold of the shipboard CNS analyzer. The total sulfur values vary between 0% and 2.75%; the higher values of >0.8% are dominantly in the lower organic-carbon-rich interval (Fig. 28). Extraordinarily high sulfur contents of about 2.5% occur in Sections 151-907A-19H-6 through -20H-1. The sulfur is probably pyritic sulfur as supported by the occurrence of significant amounts of pyrite grains (see "Lithostratigraphy" section, this chapter).

Composition of Organic Matter

The type of organic matter in the sediments of Hole 907A has been characterized using organic carbon/nitrogen (C/N) ratios and pyrolysis data. The average C/N ratios of marine zoo- and phy-

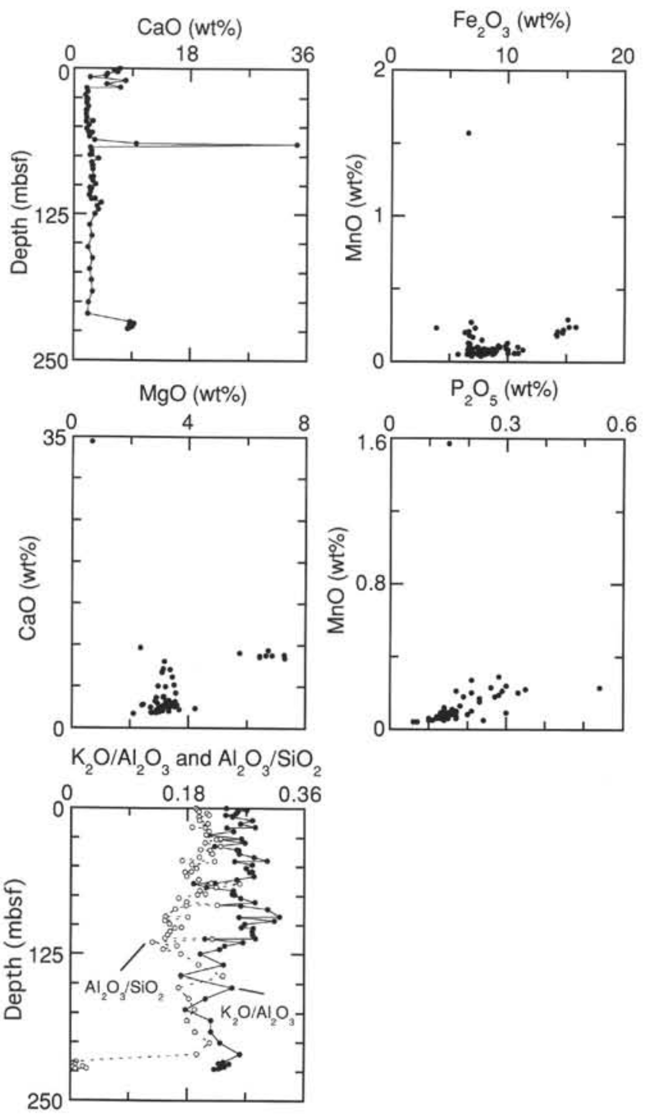

Figure 27. Sediment compositions at Site 907.

toplankton are between 5 and 8, whereas higher land plants have ratios between 20 and 200 (Bordowskiy, 1965; Emerson and Hedges, 1988). When using C/N ratios as source indicator, however, it has to be taken into account that in organic-carbon-poor sediments the amount of inorganic nitrogen (fixed as ammonium ions in the interlayers of clay minerals) may become a major portion of the total nitrogen (Müller, 1977), causing (too) low C/N ratios. A second organic-carbon-type indicator, hydrogen index (HI) values derived from pyrolysis analysis, has been used (Éspitalié et al., 1977). In immature sediments, organic matter dominated by marine components has HI values of 200 to 400 mgHC/gC, whereas terrigenous organic matter has HI values of 100 mgHC/gC or less (e.g., Stein, 1991a). The pyrolysis methods also have their limits in organic-carbon-lean sediments (Katz, 1983; Peters, 1986). Thus, in intervals with TOC values <0.5%, the C/N ratios as well as the pyrolysis data should be interpreted cautiously and supported by other methods (e.g., Stein, 1991a).

C/N ratios vary between 4 and 14 in the sediments of Site 907, indicating a mixture between marine and terrigenous organic carbon, probably with a dominance of the marine material (Fig. 29, Table 8). The hydrogen index values corroborate this (Fig. 28, Table 8). Furthermore, most of the Rock-Eval pyrograms show a distinct bimodal S2 peak, which also may suggest the occurrence of a more immature type of (marine) organic matter and a more oxidized, mature type of (terrigenous) organic matter (cf., Peters, 1986). This first interpretation, however, has to be confirmed by microscopy for maceral composition and vitrinite reflectance.

Based on (a still limited number of) C/N ratios and hydrogen index values, intervals with increased deposition of terrigenous organic carbon occur in the lowermost organic-carbon-rich interval (170 to 180 mbsf and below 195 mbsf), between 70 and 100 mbsf, and above 15 mbsf (Fig. 28). During this time, the supply of siliciclastic material was increased as based on smear-slide estimates (see "Lithostratigraphy" section, this chapter). Increased amounts of marine organic matter, on the other hand, have been preserved in the intervals between 180 and 195 mbsf and between 100 and 160 mbsf (Fig. 28). This late-middle Miocene enrichment of marine organic matter in the sediments coincides with increased abundances of biogenic opal (see "Lithostratigraphy" section, this chapter), suggesting increased surface-water productivity at that time.

Flux of Organic Matter

As changes in organic carbon concentrations can result from changes in both mineral components and organic carbon content, the percentage values were transformed into mass accumulation rates, following van Andel et al. (1975):

$$MARTOC = TOC/100 \cdot LSR \cdot DD,$$

where MARTOC = mass accumulation rates of total organic carbon (g/cm^2/k.y.), LSR = linear sedimentation rates (cm/k.y.), and DD = dry density (g/cm^3).

In general, the average mass accumulation rates of total organic carbon are low, varying between 0.004 and 0.030 (g/cm^2/k.y.) (Table 10). The minimum values occur in the upper Miocene to Quaternary intervals, with values similar to those observed in modern open-ocean oxic (low-productivity) environments (0.001 to 0.007 g/cm^2/k.y.; e.g., Stein, 1991a). In the middle Miocene, accumulation rates of organic carbon increased to about 0.020 to 0.030 g/cm^2/k.y. In the intervals dominated by marine organic matter, this might indicate some increased surface-water productivity at that time. However, further qualitative and quantitative organic geochemical data (such as detailed records of flux rates of terrigenous and marine organic carbon as well as biomarker data) are required before a more detailed paleoceanographic interpretation of the organic carbon data can be done.

PHYSICAL PROPERTIES

Introduction

The shipboard physical properties program at Site 907 included nondestructive measurements of bulk density, bulk magnetic susceptibility, compressional-wave velocity, and total natural gamma activity on whole sections of core using the multi-sensor track (MST), as well as discrete measurements of thermal conductivity, compressional-wave velocity, shear strength, and index properties. Methodology is discussed in the "Explanatory Notes" chapter (this volume).

Whole-core Measurements

Multi-sensor Track

Whole-core magnetic susceptibility at 3- to 5-cm intervals and GRAPE density at 1-cm intervals were measured on all 26 cores ob-

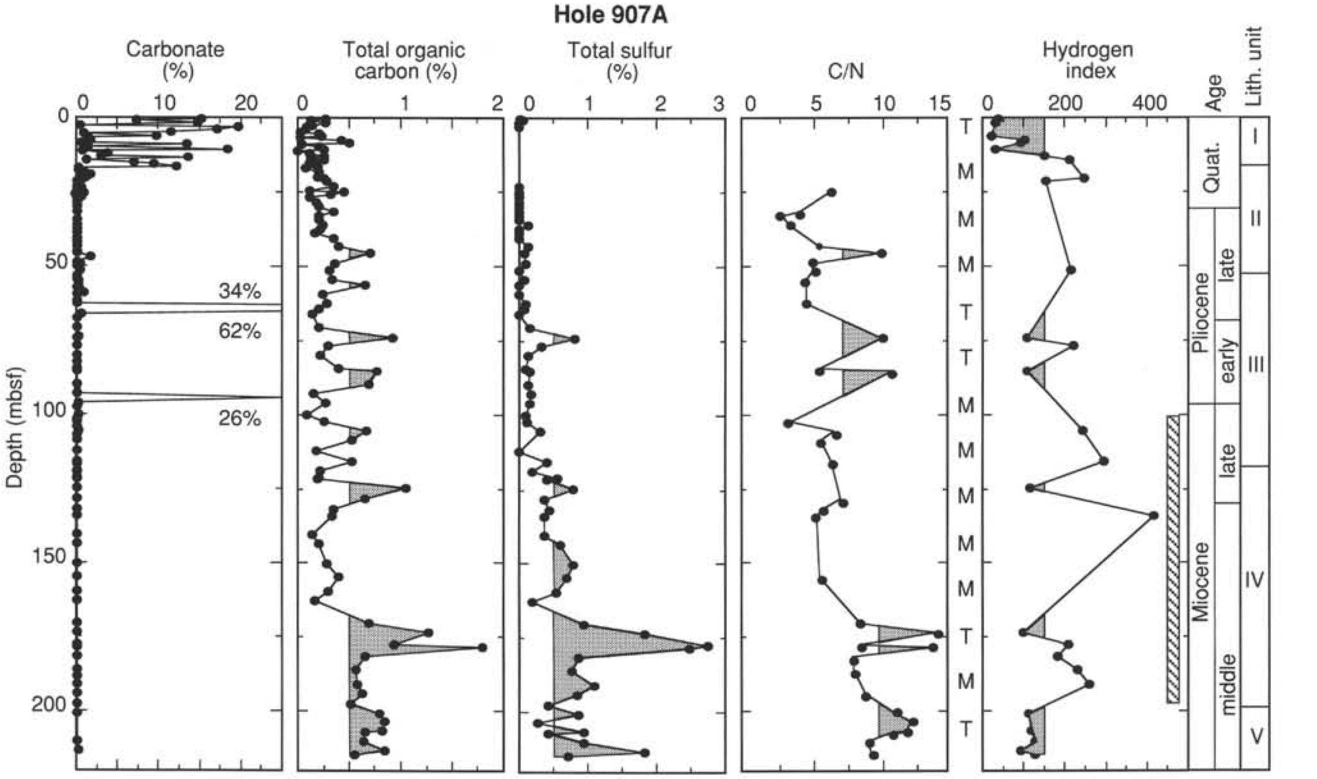

Figure 28. Carbonate contents, total organic carbon contents, total sulfur contents, organic carbon/total nitrogen (C/N) ratios, and hydrogen index values (mgHC/gC) in sediments at Site 907. "T" indicates intervals with increased amounts of terrigenous organic carbon; "M" indicates intervals with increased amounts of marine organic carbon. The hatched bar marks interval of major occurrence of biogenic silica (see "Lithostratigraphy" section, this chapter).

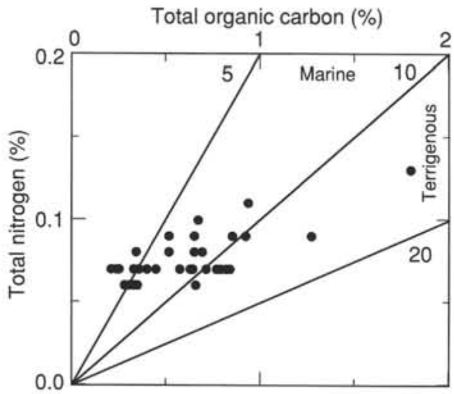

Figure 29. Total organic carbon vs. total nitrogen diagram. Lines of C/N ratios of 5, 10, and 20 are indicated. C/N ratios of <10 suggest major proportions of marine organic matter; C/N ratios of >10 suggest major proportions of terrigenous organic matter. Data points with nitrogen values of zero (determined on organic-carbon-lean samples) were not included in the diagram.

Table 10. Average mass accumulation rates of total organic carbon (MARTOC) for different time intervals.

Depth (mbsf)	Age (Ma)	LSR (cm/k.y.)	DD (g/cm^3)	TOC (%)	MARTOC ($g/cm^2/k.y.$)
0–45	0–2.5	2.0	1.1	0.20	0.004
45–135	2.5–12	1.0	0.6	0.45	0.003
135–170	12–13.5	4.0	0.6	0.30	0.008
170–197	13.5–14.0	4.0	0.6	0.75	0.018
197–214	14.0–14.5	4.0	1.0	0.75	0.030

Notes: The sedimentation rates (LSR in $cm/k.y.^{1}$) are average values based on paleomagnetic stratigraphy (see "Sedimentation Rates and Their Implications" section, this chapter). Average dry density values (DD in g/cm^3) were taken from the "Physical Properties" section, this chapter.

tained at Site 907. Because of equipment problems, natural gamma activity and velocity were measured only on a few cores near the top of Hole 907A. A preliminary chronology based on the geomagnetic reversal stratigraphy of Site 907 (see "Paleomagnetics" section, this chapter) was used to generate time series for each parameter. The low-pass filtered GRAPE density and magnetic susceptibility data (to highlight gross trends) are displayed vs. depth and as time series in Figures 30 and 31, respectively. Velocity (Fig. 32) shows a pattern of high frequency variations similar to those evident in the GRAPE density and magnetic susceptibility records (see below). High velocities were observed to correspond to high GRAPE densities. The coherent pattern of variations in natural gamma activity (Fig. 33) suggests that this is a worthwhile addition to the MST system.

A notable feature of the GRAPE density record (Fig. 30) is the significant increase up-core in bulk density, from about 1.5 g/cm^3 to about 1.75 g/cm^3, over the interval from 55 to 45 mbsf (ca. 2.7–2.5 Ma). The density increase occurs approximately at the base of lithostratigraphic Unit II (see "Lithostratigraphy" section, this chapter) and coincident with the initiation of major Northern Hemisphere glaciation (e.g., Shackleton et al., 1984). The susceptibility record (Fig. 31) averages around 50–100 uncorrected cgs units, with significant minima at 168–182 mbsf (ca. 13.7–14.1 Ma), 105–115 mbsf (ca. 7.5–8.5 Ma), and 70–80 mbsf (ca. 4.9 Ma). These intervals are also characterized by relatively high proportions of biosiliceous material, where the detrital flux of magnetic material may have been diluted by high biogenic sedimentation; alternatively, or in addition, a significant proportion of the magnetic material may have been destroyed by reductive diagenesis.

Both the susceptibility and GRAPE records show a pattern of high frequency fluctuations, typically on a scale of one or more cycles per meter, which are superimposed on the general trends shown in Figures 30A and 31A. Usually the two records show a consistent inverse relationship—susceptibility maxima corresponding to GRAPE density minima (see Fig. 34A). In the case of the numerous volcanic ash layers (see "Lithostratigraphy" section, this chapter), a direct relationship between these two parameters is observed (see Fig. 34B). To determine if the high frequency fluctuations are in the Milankovitch band, discrete 0.5-m.y. intervals of the GRAPE density time series were analyzed using a standard fast Fourier transform routine (Fig. 35). The GRAPE fluctuations are clearly in the Milankovitch frequency band, although spectral variance peaks do not align consistently with Earth orbital periodicities. The periodogram for the interval 1.0–1.5 Ma is an exception—almost all of the variance in the GRAPE density record for this interval is very close to the 41-k.y. obliquity periodicity. For this time interval, we used an inverse correlation method (Martinson et al., 1982) to tune the GRAPE record to the calculated obliquity record for the same time interval (Fig. 36). The results of spectral analysis of the magnetic susceptibility record were inconclusive, probably because many of the peaks correspond to tephra layers; however, one interval that worked well is shown in Figure 37.

Comparisons of GRAPE Density and Log Density

The deployment of the high-temperature lithodensity tool (HLDT) enabled us to directly compare core and log estimates of sediment density (see "Downhole Measurements" section, this chapter). Figure 38 shows the results of inverse correlation of the two records over the interval from ~83 to 187 mbsf. The records are similar, with a virtual peak-for-peak match over the entire record. The final correlation coefficient was 0.73. On average, the depth of the GRAPE record was shifted upward by ~2 m, presumably reflecting the effect of rebound causing a vertical expansion of the sediment core record.

Thermal Conductivity

Thermal conductivities measured at Site 907 are given in Table 11 and are illustrated in Figure 39 together with downhole trends in laboratory values of bulk density and water content. Measurements were typically made at about 75 cm in four whole-round core sections from each core and using a black rubber standard (conductivity = 0.54 ± 0.02 W/m·K) each time to evaluate the degree of error in the measurements. The red rubber standard was used to compare with the first three cores measured, but its use was discontinued after a high degree of error was encountered.

The conductivities measured in the upper portion of Hole 907A, from the seafloor to 58 mbsf, range from 0.8 to 1.3 W/m·K. The measured conductivities decrease and become relatively constant (0.8–0.9 W/m·K) in the central portion of the hole (58–190 mbsf), which corresponds to lithostratigraphic Units III and IV (see "Lithostratigraphy" section, this chapter), before beginning to increase again in lithologic Unit V (below ~190 mbsf). The decrease in thermal conductivity in the central portion of the hole is associated with high measured values of porosity and water content, especially in lithologic Unit IV. The lower conductivity in Unit IV is likely associated with the presence of increased amounts of high-porosity, biosiliceous components.

In Cores 151-907A-24X and -25X, the basaltic material was too lithified to insert the full-space conductivity probes, so half-space measurements were performed instead (see "Explanatory Notes" chapter, this volume). These measurements had a high degree of error and high temperature drift rates during testing; therefore, they are considered unreliable.

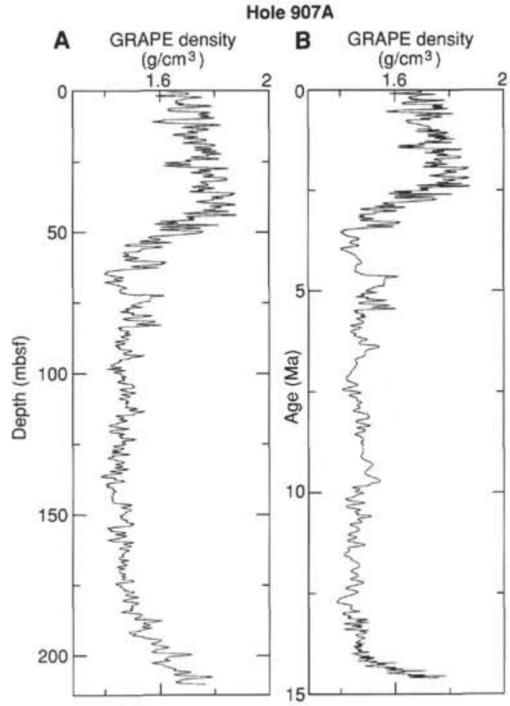

Figure 30. **A.** Downhole GRAPE density, low-pass filtered. **B.** GRAPE density time series.

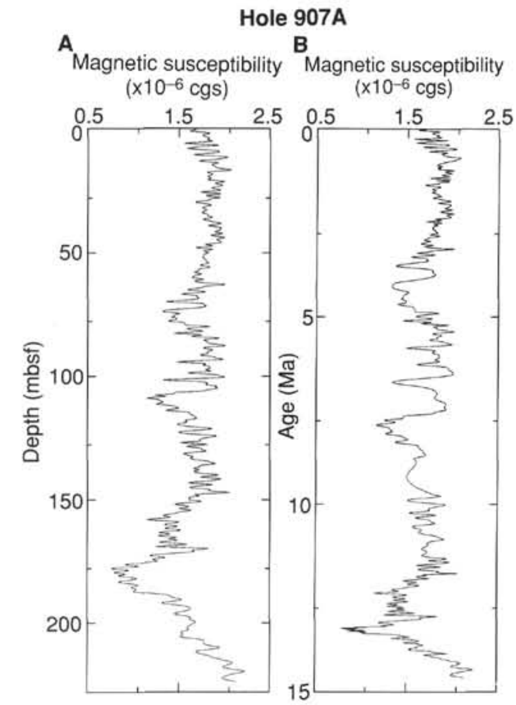

Figure 31. **A.** Downhole magnetic susceptibility, low-pass filtered. Units are logarithmic uncorrected cgs Bartington meter units. **B.** Magnetic susceptibility time series.

Split-core Measurements

Compressional Velocity

The digital sound velocimeter (DSV) and the Hamilton Frame apparatus were used to measure compressional velocity in the sediment

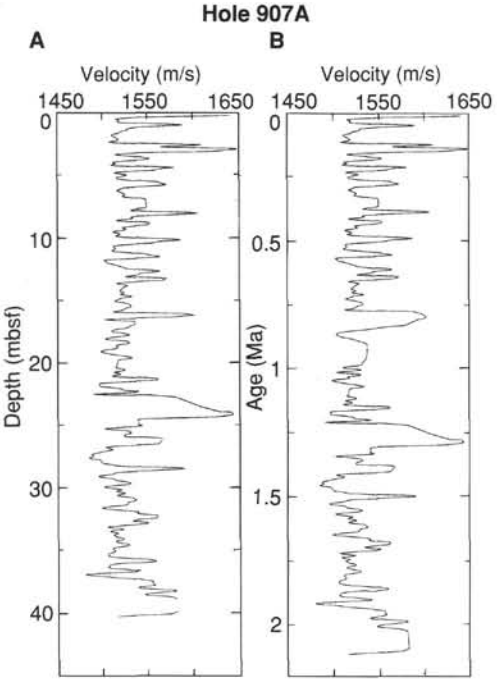

Figure 32. **A.** Downhole velocity. **B.** Velocity time series.

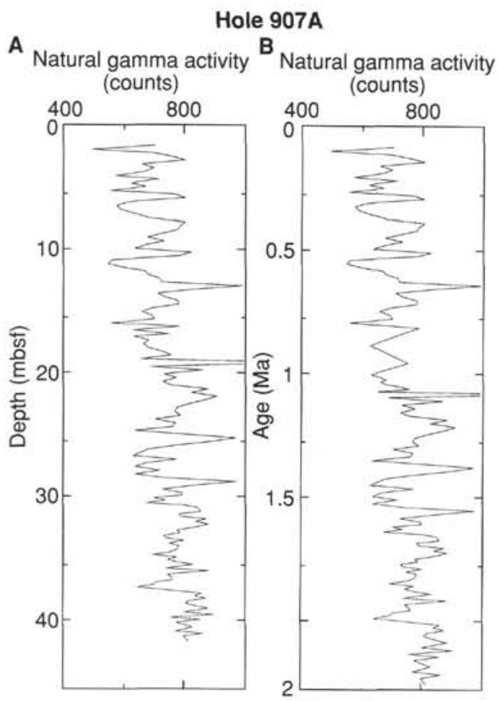

Figure 33. **A.** Downhole total natural gamma activity. Units are arbitrary but are based on total gamma counts recorded by a detector. **B.** Total natural gamma time series.

from Hole 907A. The DSV measured longitudinal velocity, parallel to the along-core axis, in Cores 151-907A-1H through -6H at the rate of one measurement per core section. When it became impossible to insert the sonic transducers into the sediment without cracking, then measurements were continued using the Hamilton Frame in Core 151-907A-8H (below 64.3 mbsf). Because the transducers on the Hamilton Frame are mounted on a vertical press, these measurements were taken perpendicular to the split-surface of the core, and corrections were made for the core liner thickness and traveltime. The data

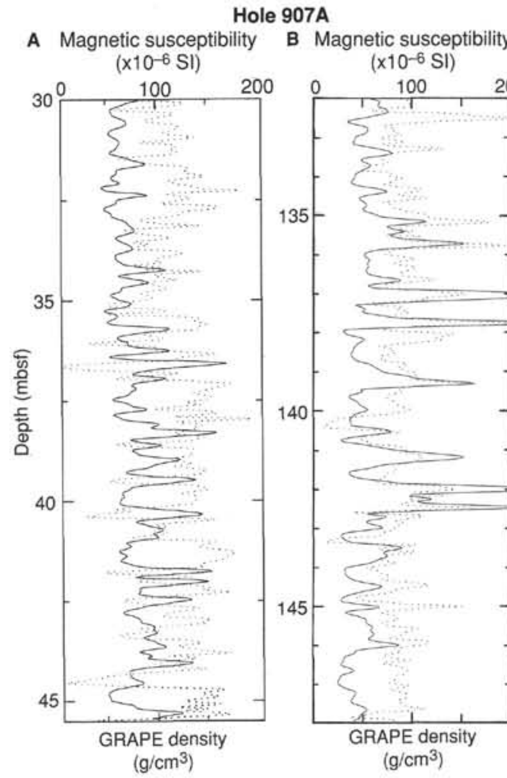

Figure 34. **A.** Example of the inverse relationship between magnetic susceptibility (solid curve) and GRAPE density (broken curve). **B.** Example of a direct relationship between magnetic susceptibility (solid curve) and GRAPE density (broken curve).

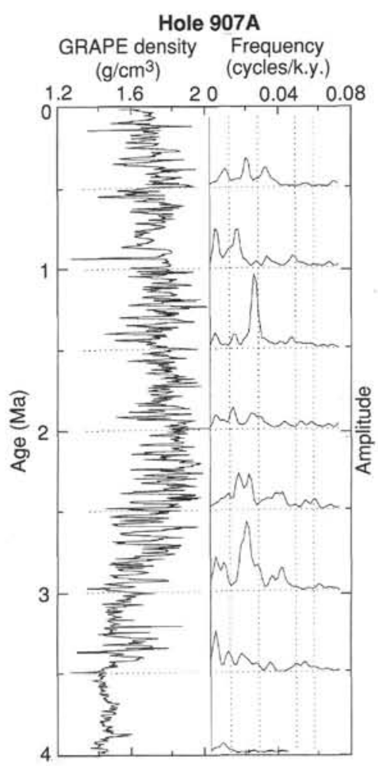

Figure 35. Results of evolutive spectral analysis of 0.5-m.y. intervals from 0 to 4 Ma of the GRAPE density time series. Vertical broken lines on the periodograms correspond to 100, 41, 23, and 19 k.y. periodicities (k.y. = thousand years).

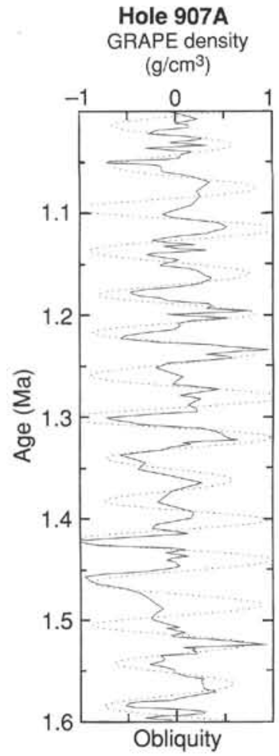

Figure 36. Results of tuning the GRAPE density record (continuous curve) for the interval 1.0–1.6 Ma to calculate Earth orbital obliquity (broken curve) for the same time interval. The two curves were matched using an inverse correlation method (Martinson et al., 1982).

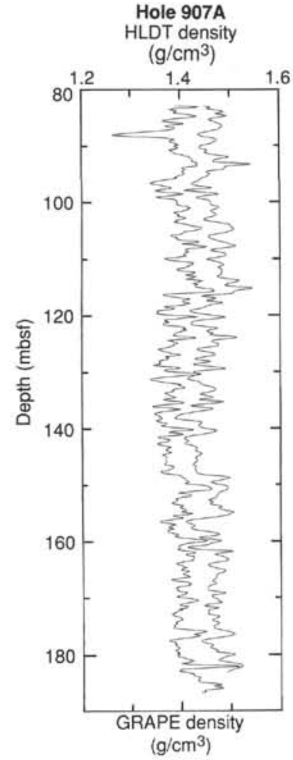

Figure 38. Comparison of sediment density determined by the HLDT (curve on the left) and by GRAPE measurement (curve on the right). The GRAPE curve has been low-pass filtered. The two curves were matched using an inverse correlation method (Martinson et al., 1982).

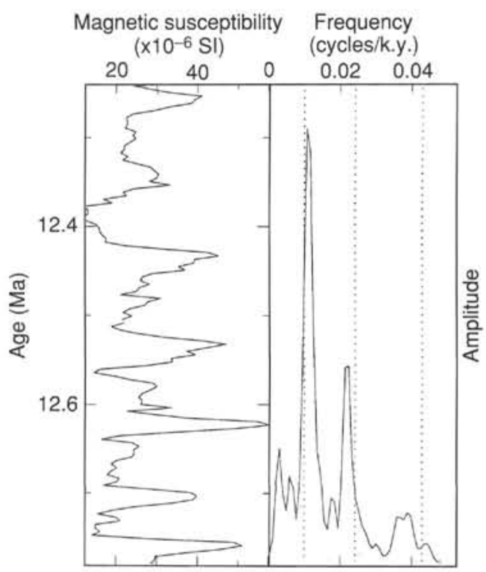

Figure 37. Results of evolutive spectral analysis for the interval 12.3–12.7 Ma of the magnetic susceptibility time series. Vertical broken lines on the periodograms correspond to 100, 41, 23, and 19 k.y. periodicities.

from these velocity measurements are given in Table 12 and are illustrated in Figure 40 with comparisons to laboratory bulk density and porosity data.

The velocities in the upper part of Hole 907A are fractionally above those measured for seawater. The scatter in the data is attributed to the variability of index properties in the sedimentary deposits recovered; however, an examination of Figure 40 indicates that the average velocity increases slightly downhole. A low-velocity interval is observed from ~80 to 120 mbsf; this interval also is observed in the sonic log (see "Downhole Measurements" section, this chapter). The measured velocities become more consistent below ~120 mbsf, where both the bulk density and porosity of the sediment become relatively constant (see Fig. 40).

Shear Strength

Shear strength measurements were made routinely in the sediment from split half-cores using the mechanical vane shear device in sediment from the seafloor to ~55 mbsf, and using a hand-held penetrometer below this level as the sediment became too firm to test with the vane apparatus. The results of the vane and penetrometer strength measurements are given in Table 13 and are illustrated in Figure 41 with plots of index properties. The peak shear strengths using the vane varied from 8.7 to 115.8 kPa. The peak strengths reported for the penetrometer are actually the average of two to three measurements made at each depth.

Index Properties

Determinations of index properties were made for 295 samples in Hole 907A at the rate of about 2 samples/core section (see Table 14). The data are internally consistent, with the exception of grain density determinations, which seem to be in error by a fair margin. The generally high water content of the sediment may be responsible for some of the scatter in grain density because the volume of dry solids in the sample container after drying is small relative to the total volume of the container.

Table 11. Thermal conductivity measurements from Hole 907A.

Core, section, interval top (cm)	Depth (mbsf)	M	P #	TC_{corr} (W/m·K)	Std dev (W/m·K)	Drift (°C/min)
151-907A-						
1H-2, 75	2.25	F	319	1.089	0.00309	0.009
1H-3, 81	3.81	F	325	1.249	0.00394	0.014
1H-4, 75	5.25	F	338	0.818	0.00407	0.009
1H-5, 75	6.75	F	339	0.998	0.01370	0.057
2H-2, 75	9.55	F	332	1.039	0.00339	−0.011
2H-3, 75	11.05	F	325	0.952	0.00285	0.019
2H-5, 75	14.05	F	338	0.992	0.00873	0.022
2H-6, 75	15.55	F	339	1.182	0.00229	0.020
3H-2, 75	19.05	F	332	0.907	0.00282	0.020
3H-3, 75	20.55	F	325	1.158	0.00302	0.021
3H-5, 75	23.55	F	338	1.041	0.00333	0.022
3H-6, 75	25.05	F	339	1.170	0.00323	0.025
4H-1, 75	27.05	F	332	1.106	0.00359	0.018
4H-3, 75	30.05	F	325	1.276	0.00233	0.015
4H-5, 75	33.05	F	338	1.066	0.00243	0.001
4H-6, 75	34.55	F	339	1.039	0.00193	0.022
4H-1, 75	27.05	F	332	1.430	0.00276	0.016
4H-2, 75	28.55	F	325	1.216	0.00299	0.005
4H-3, 75	30.05	F	338	1.050	0.00615	−0.003
4H-4, 75	31.55	F	339	1.164	0.00289	−0.007
4H-5, 75	33.05	F	340	0.621	0.01320	0.016
6H-2, 75	47.55	F	332	1.019	0.00259	0.017
6H-3,75	49.05	F	325	1.580	0.00354	0.025
6H-4, 75	50.55	F	338	1.017	0.00354	0.030
6H-5, 75	52.05	F	339	1.059	0.00236	0.022
7H-2, 75	57.05	F	332	1.029	0.00075	0.010
7H-3, 75	58.55	F	325	0.919	0.00330	0.039
7H-4, 75	60.05	F	338	0.813	0.00438	0.061
7H-5, 75	61.55	F	339	0.867	0.00264	0.025
8H-2, 75	66.55	F	332	0.836	0.00371	0.035
8H-3,75	68.05	F	325	0.905	0.00294	0.021
8H-5, 75	71.05	F	338	0.780	0.00203	0.068
8H-6, 75	72.55	F	339	0.747	0.00312	0.002
9H-2, 75	76.05	F	332	0.933	0.00281	0.015
9H-3, 75	77.55	F	325	0.894	0.00220	−0.005
9H-5, 75	80.55	F	338	0.760	0.00357	0.029
9H-6, 75	82.05	F	339	0.882	0.00297	−0.001
10H-2, 75	85.55	F	332	1.095	0.00329	0.021
10H-3, 75	87.05	F	325	0.905	0.00300	0.006
10H-5, 75	90.05	F	338	0.905	0.00361	0.050
10H-6, 75	91.55	F	339	0.782	0.00281	0.015
11H-2, 75	95.05	F	332	0.829	0.00292	0.030
11H-3, 75	96.55	F	325	0.925	0.00277	0.028
11H-5, 75	99.55	F	338	0.828	0.00723	0.062
11H-6, 75	101.05	F	339	0.822	0.00536	0.022
12H-3, 75	106.05	F	325	0.888	0.00237	0.013
12H-5, 75	109.05	F	338	0.760	0.00597	0.024
12H-6, 75	110.55	F	339	0.835	0.00383	0.033
12H-2, 75	104.55	F	340	0.914	0.00346	0.024
12H-5, 75	109.05	F	338	0.752	0.00476	0.020
14H-2, 75	123.55	F	325	0.882	0.00204	0.016
14H-3, 75	125.05	F	338	0.764	0.00335	0.028
14H-5, 75	128.05	F	339	0.885	0.00347	0.022
14H-6, 75	129.55	F	340	0.867	0.00253	0.026
13H-2, 75	114.05	F	325	0.865	0.00264	0.012
13H-3, 75	115.55	F	338	0.773	0.00289	0.018
13H-5, 75	118.55	F	339	0.784	0.00148	0.031
13H-6, 75	120.05	F	340	0.802	0.00399	0.009
15H-2, 75	133.05	F	325	0.933	0.00366	0.024
15H-4, 75	136.05	F	339	0.853	0.00462	0.021
15H-5, 75	137.55	F	340	0.851	0.00352	0.013
16H-2, 80	142.60	F	325	0.903	0.00257	0.016
16H-3, 80	144.10	F	338	0.901	0.00386	0.019
16H-4, 80	145.60	F	339	0.784	0.00278	0.022
16H-5, 80	147.10	F	340	0.807	0.00274	0.029
17H-2, 75	152.05	F	325	0.925	0.00219	0.003
17H-3, 75	153.55	F	338	0.798	0.00546	0.019
17H-4, 75	155.05	F	339	0.770	0.00361	0.004
17H-5, 75	156.55	F	340	0.877	0.00322	0.006
18H-2, 75	161.55	F	325	0.914	0.00264	0.039
18H-3, 75	163.05	F	338	0.700	0.00664	−0.033
18H-4, 75	164.55	F	339	0.863	0.00265	0.014
18H-5, 75	166.05	F	340	0.839	0.00327	0.010
18H-2, 75	161.55	F	332	0.858	0.00350	0.010
18H-3, 75	163.05	F	338	0.871	0.00230	0.033
18H-5, 75	166.05	F	339	0.809	0.00367	0.007
18H-6, 75	167.55	F	340	0.862	0.00223	0.016
19H-3, 75	172.55	F	338	0.815	0.00212	0.028
19H-5, 75	175.55	F	339	0.936	0.00274	0.030
19H-6, 75	177.05	F	340	0.898	0.00276	0.025
19H-2, 75	171.05	F	332	0.840	0.00241	0.008
21H-2, 70	190.00	F	332	0.866	0.00412	0.015
21H-3, 70	191.50	F	338	0.846	0.00257	0.023
21H-5, 70	194.50	F	339	0.942	0.00278	0.024
21H-6, 70	196.00	F	340	0.981	0.00302	0.026
22H-2, 75	199.55	F	332	0.934	0.00156	0.005
22H-2, 75	199.55	F	332	0.964	0.00393	0.030
22H-3, 75	201.05	F	338	1.052	0.00413	0.035
22H-5, 75	204.05	F	339	0.885	0.00456	0.015
22H-6, 75	205.55	F	340	1.067	0.00348	−0.002
23H-2, 75	209.05	F	332	1.044	0.00273	0.016
23H-3, 75	210.55	F	338	0.982	0.00205	0.010
23H-5, 75	213.55	F	339	1.227	0.00321	−0.016
23H-6, 75	215.05	F	340	1.049	0.00243	0.018
25X-1, 90	218.20	H	322	0.938	0.02750	−0.271
25X-2, 82	219.50	H	337	0.853	0.00306	−0.077
25X-2, 90	219.58	H	322	1.792	0.01400	0.038
26X-1, 76	221.76	H	337	0.758	0.00394	−0.112

Notes: M = method used, either F = full-space or H = half-space; P # = probe number used for test; TC_{corr} = thermal conductivity corrected for drift; Std dev = standard deviation of the measurement.

Geotechnical Units

Statistical data abstracted from the index properties were used to construct a series of units with respect to geotechnical properties. Four geotechnical units were identified in Hole 907A. The characteristic values for index properties in each lithostratigraphic unit defined by the sedimentologists (see "Lithostratigraphy" section, this chapter) and for each of the four geotechnical units are given in Table 15. Plots of selected index properties vs. depth are shown in Figures 39 through 41.

Hole 907A was divided into an upper zone of highly variable but generally high bulk density, low porosity, silty clay and clayey silt from the seafloor to ~45 mbsf (geotechnical Unit G-I); a transitional zone between 45 and 75 mbsf, which exhibited a decreasing bulk-density trend and increasing trends in water content and porosity (geotechnical Unit G-II); a central zone from 75 to ~197 mbsf having relatively constant index properties (geotechnical Unit G-III); and a lower zone from ~197 mbsf to the contact with igneous rocks (geotechnical Unit G-IV), which exhibited an increasing bulk-density trend and decreasing trends in water content and porosity.

The geotechnical units described in this section are based on downhole trends in measured sediment index properties and an analysis of the higher resolution data provided by sensors on the MST. Lithostratigraphic unit boundaries are based on a somewhat different set of criteria, although the two methods seem to complement each other in describing the nature of the stratigraphic column at Site 907. For example, the lithostratigraphic unit classification, based on textural and compositional information from smear slides and visual core descriptions, divides a comparatively homogeneous unit in terms of geotechnical variation between 75 and 195 mbsf (geotechnical Unit G-III) into three sub-sections (lower lithologic Unit IIIA to the base of Unit IV; see "Lithostratigraphy" section, this chapter).

The interbedded upper sediment layers between the mud line and 45 mbsf encompass lithologic Unit I and the upper part of Unit II, but are nearly indistinguishable in terms of their bulk physical properties. The sediment between 45 and 75 mbsf represents a transition between the upper and lower sedimentary regimes in Hole 907A, characterized by high reversed gradients in physical property trends relative to the upper geotechnical unit. The mean water content (% wet sample weight) increases by about 12% and wet-bulk density decreases by ~7% across this interval. The effects of overburden and compaction are of secondary importance in this unit, whereas changes in sediment texture seem to dominate. This is especially evident in Core 151-907A-6H where alternating layers of silt and clay-sized

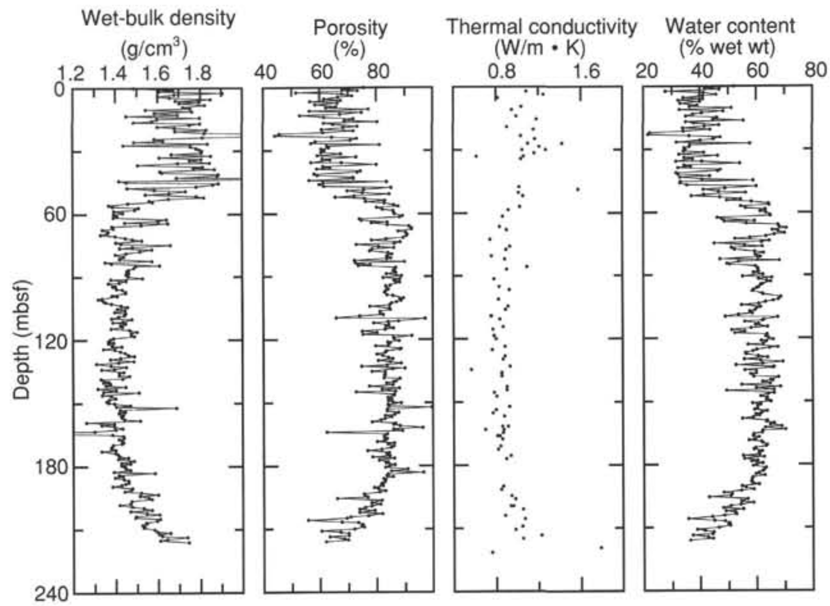

Figure 39. Comparisons of laboratory index property measurements and thermal conductivity vs. depth in Hole 907A.

material are exhibited as sharp changes in bulk density, both in discrete measurements and in the GRAPE density log (Fig. 42). A comparison between laboratory bulk-density measurements and GRAPE density measured on the whole-round cores (Fig. 43) indicates that the laboratory values and the data collected by the GRAPE sensor can be used to extract high-resolution records of other index properties at the same resolution as the GRAPE data.

DOWNHOLE MEASUREMENTS

Logging Operations and Log Quality

A full suite of four Schlumberger tool strings was run at Hole 907A: the seismic stratigraphic, lithoporosity, Formation MicroScanner, and geochemical combinations. The wireline heave compensator (WHC) was used to counter the mild ship heave (0.2–0.4 m heave). The base of the drill pipe was set at 83 mbsf. A summary of the logging tool strings used during Leg 151 is found in the "Explanatory Notes" chapter (this volume). A summary of the logging operations at Hole 907A is given in Table 16.

The seismic stratigraphic tool string comprising sonic (DSI), induction (DIT), and natural gamma-ray (NGT) tools, along with the Lamont-Doherty temperature tool (TLT), was run first. Total penetration in Hole 907A was 224.1 mbsf; however, hole fill or possibly a bridge prevented the tool string from going below 198.4 mbsf. Data were recorded at a logging speed of 600 ft/hr from this depth to the mud line with pipe being pulled to 63 mbsf. Within the pipe section the sonic and induction data are invalid and the natural gamma-ray data are highly attenuated. The open hole natural gamma-ray data are displayed in Figure 44, and the resistivity and sonic velocity data in Figure 45.

The lithodensity tool string, consisting of natural gamma-ray (NGT), density (HLDT), and neutron porosity (CNT) tools together with the TLT was run second. Two passes were completed at a logging speed of 900 ft/hr, and the main log was recorded over the interval from 192.4 mbsf to the end of pipe (pulled to 63 mbsf). The HLDT was run in the high-resolution mode, recording data at 1.2 in. increments. The data recorded are generally of high quality, although the density data are not reliable for the interval where the eccentralizing caliper arm was retracted, between 83.4 and 63 mbsf (Fig. 45).

The Formation MicroScanner (FMS) with an NGT tool was run third at 900 ft/hr from 192.4 mbsf to the end of pipe at 63 mbsf. A repeat section was run in the upper portion of the hole from 134 to 63 mbsf at a logging speed of 1600 ft/hr. The orthogonal calipers of the FMS (Fig. 45) are shown to be at their maximum (>16 in.) in large portions of the lower section of the hole. Over these intervals the contact between the FMS pads and the borehole wall is poor, resulting in unreliable microresistivity images.

The final tool string run was the geochemical combination consisting of an NGT, the aluminum activation clay tool (AACT), and the gamma-ray spectrometry tool (GST) along with the TLT. Data were recorded from 189.3 mbsf to 74.5 mbsf where the log was prematurely ended by difficulties entering the end of the drill pipe. After many unsuccessful attempts to enter, tool rescue operations began. A Kinley crimper-cutter device was deployed down the pipe. This device first crimps to the wireline in the bottom hole assembly (BHA), attaching the tool to the BHA, before cutting the wireline. The logging cable was spooled in, and the drill pipe was then tripped to the surface where the logging tool was recovered hanging immediately below the drill bit.

Results

Borehole Temperature

The Lamont-Doherty temperature tool (TLT) was deployed on three of the four tool strings in Hole 907A. The temperature data from the seismic stratigraphic string are shown in Figure 46. During the process of drilling, cold seawater is circulated in the hole cooling down the formation surrounding the borehole. Once drilling ceases, the temperature of the formation gradually rebounds to its equilibrium temperature. As three readings of bottom-hole temperature were obtained over a period of 11 hr by the TLT, it is possible to apply the relationship of Lachenbruch and Brewer (1959), by which the temperature evolution with time is extrapolated to calculate the initial or "virgin" formation temperature. The virgin formation temperature by this method is 11.69°C at 200 mbsf. With a mud-line temperature of −1.64°C, the thermal gradient is 66.7°C/km. This is low compared to the Adara results of 120.7°C/km; the discrepancy may be because of the downward mixing of cold water during logging operations. Alternatively, the Adara readings, measured only in the upper portion of the hole, could indicate a nonlinear temperature gradient caused by thermal conductivity variations with depth or by the possible upward migration of warm fluids.

Table 12. Compressional-wave velocity measurements from Hole 907A.

Core, section, interval (cm)	Depth (mbsf)	Tool	Velocity (m/s)	
			Perp	Par
151-907A-				
1H-1, 26–33	0.00	dsv	1534	
1H-2, 20–27	1.70	dsv	1527	
1H-3, 20–27	3.20	dsv	1534	
1H-4, 20–27	4.42	dsv	1527	
1H-5, 22–29	6.22	dsv	1517	
2H-1, 38–45	7.69	dsv	1548	
2H-2, 20–27	9.00	dsv	1517	
2H-2, 20–27	9.00	dsv	1534	
2H-3, 25–32	10.55	dsv	1507	
2H-4, 28–35	12.08	dsv	1430	
2H-5, 19–26	13.49	dsv	1432	
2H-6, 20–27	15.00	dsv	1489	
3H-1, 17–34	16.97	dsv	1470	
3H-2, 30–37	18.60	dsv	1509	
3H-3, 15–22	19.95	dsv	1509	
3H-4, 20–27	21.50	dsv	1507	
3H-5, 17–24	22.97	dsv	1494	
3H-5, 17–24	22.97	dsv	1512	
3H-6, 20–27	24.50	dsv	1642	
4H-2, 18–25	27.98	dsv	1638	
4H-3, 19–26	29.49	dsv	1480	
4H-4, 19–26	30.99	dsv	1480	
4H-5, 19–26	32.49	dsv	1524	
4H-6, 21–28	34.01	dsv	1521	
4H-7, 10–17	35.40	dsv	1538	
5H-1, 21–28	36.01	dsv	1493	
5H-2, 21–29	37.51	dsv	1499	
5H-3, 31–38	38.91	dsv	1473	
5H-4, 43–50	40.73	dsv	n.m.	
5H-5, 21–28	42.01	dsv	1545	
5H-6, 21–28	43.51	dsv	n.m.	
6H-1, 21–28	45.55	dsv	1531	
6H-2, 23–30	47.03	dsv	1521	
6H-3, 90–97	49.20	dsv	1521	
6H-4, 20–27	50.00	dsv	1546	
6H-5, 21–28	51.50	dsv	n.m.	
6H-6, 19–26	53.00	dsv	n.m.	
8H-1, 25–27	64.55	ham		1541
8H-1, 15–17	64.45	ham		1530
8H-3, 30–32	67.60	ham		1464
8H-5, 20–22	70.60	ham		n.m.
8H-5, 40–42	70.70	ham		1447
8H-7, 10–12	73.30	ham		1520
9H-1, 105–107	74.85	ham		1536
9H-2, 120–122	76.50	ham		1450
9H-3, 120–122	78.00	ham		1596
9H-4, 120–122	79.50	ham		1492
9H-5, 120–122	81.00	ham		1501
9H-6, 125–127	82.55	ham		1494
10H-1, 125–127	84.55	ham		1481
10H-2, 125–127	86.05	ham		1432
10H-3, 125–127	87.55	ham		1503
10H-4, 125–127	89.05	ham		1446
10H-5, 125–127	90.55	ham		1500
11H-2, 125–127	95.55	ham		1473
11H-3, 125–127	97.05	ham		1451
11H-4, 125–127	98.55	ham		1530
11H-6, 115–117	101.45	ham		n.m.
11H-7, 12–14	102.49	ham		1434
12H-1, 125–127	103.55	ham		1496
12H-2, 125–127	105.05	ham		1509
12H-3, 113–115	106.43	ham		1511
12H-4, 128–130	108.08	ham		1433
12H-5, 120–122	109.50	ham		1496
12H-6, 120–122	111.00	ham		1477
12H-7, 15–17	111.45	ham		1506
13H-1, 125–127	113.05	ham		1486
13H-2, 135–137	114.66	ham		n.m.
13H-3, 125–127	116.00	ham		n.m.
13H-4, 125–127	117.55	ham		1428
13H-5, 125–127	119.05	ham		1473
13H-6, 125–127	120.55	ham		1487
13H-7, 24–26	121.04	ham		1527
14H-1, 125–127	122.55	ham		1490
14H-2, 120–122	124.00	ham		1531
14H-3, 125–127	125.55	ham		1536
14H-4, 120–122	127.00	ham		1547
14H-5, 117–119	128.47	ham		1532
14H-6, 125–127	128.55	ham		1544
14H-7, 42–44	130.05	ham		1513
15H-1, 125–127	132.05	ham		1519
15H-2, 120–122	133.50	ham		n.m.
15H-3, 125–127	135.55	ham		1536
15H-4, 125–127	136.55	ham		1520
15H-5, 125–127	138.05	ham		1524
15H-6, 125–127	139.55	ham		1513
15H-7, 13–14	139.93	ham		1504
16H-1, 135–137	141.55	ham		1519
16H-2, 132–134	143.12	ham		1520
16H-3, 125–127	144.55	ham		1529
16H-4, 125–127	146.05	ham		1533
16H-5, 125–127	147.55	ham		1495
16H-6, 125–127	149.05	ham		1510
16H-7, 39–41	149.69	ham		1516
17H-1, 117–119	150.97	ham		1536
17H-2, 125–127	152.55	ham		n.m.
17H-4, 125–127	155.55	ham		1508
17H-5, 125–127	157.05	ham		1539
17H-6, 125–127	158.55	ham		1520
18H-1, 125–127	160.55	ham		1523
18H-2, 125–127	162.05	ham		1514
18H-3, 125–127	163.55	ham		1529
18H-4, 125–127	165.05	ham		1513
18H-5, 125–127	166.55	ham		1535
18H-6, 125–127	168.05	ham		1523
19H-1, 125–127	170.05	ham		1552
19H-2, 125–127	171.55	ham		1525
19H-3, 125–127	173.05	ham		1514
19H-4, 125–127	174.55	ham		n.m.
19H-5, 125–127	176.05	ham		1573
19H-6, 125–127	177.55	ham		1518
20H-1, 125–127	179.55	ham		1511
20H-2, 125–127	181.05	ham		1504
20H-3, 40–42	181.70	ham		1524
20H-4, 125–127	184.05	ham		1528
20H-5, 125–127	185.55	ham		n.m.
20H-6, 135–137	187.15	ham		1532
21H-1, 125–127	189.05	ham		1518
21H-3, 125–127	192.05	ham		1511
21H-4, 136–138	193.66	ham		1497
21H-5, 125–127	195.05	ham		1519
21H-6, 110–112	196.40	ham		1536
22H-1, 125–127	198.55	ham		1535
22H-2, 125–127	200.05	ham		1579
22H-2, 125–127	200.05	ham		1537
22H-3, 125–127	201.55	ham		1585
22H-4, 125–127	203.05	ham		1567
22H-5, 125–127	204.55	ham		1586
22H-6, 125–127	206.05	ham		n.m.
22H-6, 125–127	206.05	ham		n.m.
22H-6, 102–104	205.82	ham		1515
23H-1, 125–127	208.05	ham		1597
23H-2, 125–127	209.55	ham		1540
23H-3, 125–127	211.05	ham		1539
23H-4, 125–127	212.55	ham		1547
23H-5, 125–127	214.05	ham		1542
23H-6, 125–127	215.55	ham		1493

Note: Tool = device used for measurement, either dsv = digital sound velocimeter or ham = Hamilton Frame. Perp = perpendicular; Par = parallel. n.m. = not measured.

Correlation of Logs to the Sediment Section

The interval logged in Hole 907A (83–198 mbsf) is relatively uniform, but features can be recognized that correlate with sedimentological descriptions of the recovered cores (see "Lithostratigraphy" section, this chapter). The logs covered sedimentary Units III and IV, and all logs begin deeper than the prominent transition in the lower Pliocene that marks the base of sedimentary Unit II (Fig. 47).

Sedimentary Unit IV is distinguished by a significant siliceous biofossil component in the sediments. Typically, such opal-rich sediments have lower bulk densities and lower resistivities than other pelagic sequences. Opal, with a grain density of about 2.2 g/cm^3, is less dense than carbonates (2.7 g/cm^3), clays (2.3–2.7 g/cm^3), or quartz (2.65 g/cm^3). The open structure of siliceous skeletons and water bound by opal helps to retain water in the buried sediment and lower the sediment's electrical resistivity. Conductive seawater replaces more resistive aluminosilicates. In Figure 47, Unit IV can be identified by the significantly lower resistivities measured during logging and also by lower bulk density.

If the opal (and its associated water) replaced clays on a one-to-one basis in the sediments, natural gamma-ray activity in the high opal section also should decrease. In Figure 47 the computed gamma

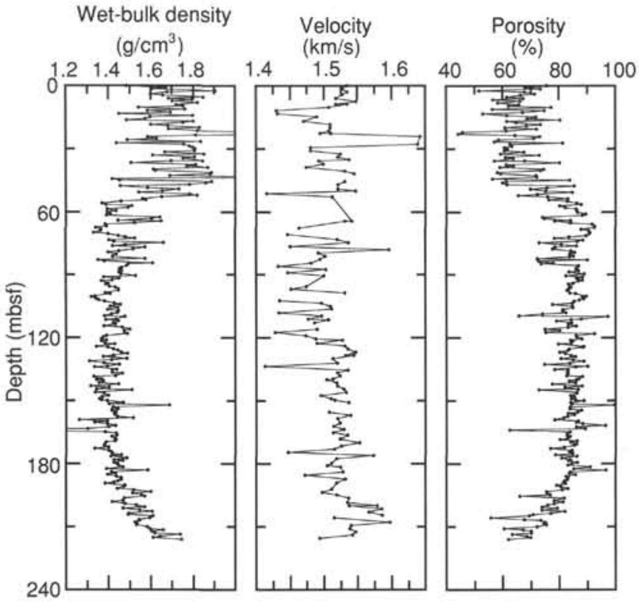

Figure 40. Comparisons among laboratory velocity measurements and measurements of bulk density and porosity vs. depth in Hole 907A.

ray (CGR) log represents the gamma-ray activity from Th and K, the component of natural gamma radiation associated with clays and feldspars. It is apparent that there is not a simple correspondence between natural gamma-ray activity and changes in opal content, as interpreted from the resistivity log. Thus there may be significant periodic variations of aluminosilicate composition through the section in addition to the change in opal contents.

Formation MicroScanner

The orthogonal calipers from the FMS (Fig. 45) show the large and elliptical nature of the borehole throughout the logged section. As a result of the large borehole diameter, the contact of the FMS pads with the borehole wall was often poor, resulting in poor quality images in sections of the borehole. The raw images nevertheless are seen to exhibit numerous, more highly resistive bands, particularly in the interval 90–140 mbsf, that correlate well with ash layers identified in the recovered cores (see "Lithostratigraphy" section, this chapter). Post-cruise processing of the raw images should significantly enhance the definition of these layers.

Porosity Estimates from the Density and Resistivity Logs

Both the resistivity and bulk-density logs respond strongly to changes in porosity of the sediment, because strong density and resistivity contrasts exist between pore waters and the aluminosilicate matrix. Porosity can be estimated either from the resistivity log via Archie's law (Archie, 1942) or from the wet-bulk density log by rearranging the equation defining wet-bulk density to solve for ϕ (see "Explanatory Notes" chapter, this volume). Figure 48 illustrates the results of these different methods to estimate porosity. We used an exponent of 2.4 in the Archie equation, and assumed a grain density of 2.8 g/cm^3 and a water density of 1.025 g/cm^3 in the wet-bulk density equation.

The resistivity- and density-derived estimates of porosity are offset from each other. If the porosity in the opal-rich section below 118 mbsf is matched between the two records, the resistivity estimate of porosity in the unit above is less than that estimated by density. No better match between the two porosity estimates could be achieved by varying the exponent in the Archie equation. We think that the resis-

Table 13. Shear strength measurements from Hole 907A.

Core, section, interval (cm)	Depth (mbsf)	SN	Vane (kPa)	Res (kPa)	Pen (kPa)
151-907A-					
1H-1, 32–33	0.32	3	13	10	
1H-2, 25–26	1.75	3	9	4	
1H-3, 25–26	3.25	3	9	5	
1H-4, 25–26	4.75	3	10	6	
1H-5, 40–41	6.40	3	11	6	
2H-1, 42–43	7.72	3	13	9	
2H-1, 102–103	8.32	3	20	11	
2H-2, 25–26	9.05	3	15	8	
2H-3, 25–26	10.60	3	15	9	
2H-4, 32–33	12.10	3	19	9	
2H-4, 102–103	12.80	3	15	9	
2H-5, 24–25	13.50	3	17	9	
2H-6, 25–26	15.10	3	12	9	
2H-7, 25–26	16.60	3	21	10	
3H-1, 26–27	17.10	3	22	12	
3H-2, 33–34	18.60	3	21	11	
3H-3, 19–20	20.00	3	27	15	
3H-4, 25–26	21.60	3	28	14	
3H-5, 20–21	23.00	3	45	26	
3H-5, 103–104	23.80	3	29	18	
3H-6, 23–24	24.50	3	54		
4H-1, 100–101	27.30	3	32	10	
4H-3, 79–80	30.10	3	35	21	
4H-4, 78–79	31.60	3	42	22	
4H-5, 79–80	33.10	3	62	25	
4H-6, 80–81	34.60	3	41	21	
4H-7, 47–48	35.80	3	45	23	
5H-2, 104–105	38.30	3	51	30	
5H-3, 92–93	39.70	3	46	24	
5H-5, 115–116	43.00	4	73	27	
5H-6, 100–101	44.30	4	83	34	
5H-7, 57–58	45.40	4	67	38	
6H-1, 25–26	45.60	4	27	61	
6H-2, 27–28	47.10	4	79	32	
6H-3, 99–100	49.30	4	66	27	
6H-3, 25–26	48.60	4	69	23	
6H-4, 25–26	50.10	4	80	26	
6H-5, 25–26	51.60	4	69	22	
6H-5, 103–104	52.30	4	116	36	
6H-5, 105–106	52.40				74
6H-6, 24–23	53.00	4	92	32	
6H-6, 22–23	53.00				71
6H-7, 22–23	54.50	4	191	32	
6H-7, 20–211	54.50				65
6H-7, 60–61	54.90				79
7H-1, 15–16	55.00				59
7H-1, 60–61	55.40				58
7H-1, 110–111	55.90				76
7H-2, 15–16	56.50				101
7H-2, 60–61	56.90				113
7H-2, 110–111	57.40				93
7H-3, 15–16	58.00				81
7H-3, 60–61	58.40				81
7H-3, 110–111	58.90				69
7H-4, 15–16	59.50				105
7H-4, 110–111	60.40				88
7H-5, 15–16	61.00				81
7H-6, 15–16	62.50				98
7H-6, 110–111	63.40				113
7H-7, 50–51	64.30				98
8H-1, 25–26	64.60				61
8H-2, 25–26	66.10				60
8H-3, 25–26	67.60				98
8H-4, 25–26	69.10				94
8H-5, 25–26	70.60				101
8H-6, 25–26	72.10				93
8H-7, 25–26	73.60				78
9H-1, 25–26	74.10				69
9H-2, 25–26	75.60				86
9H-3, 25–26	77.10				66
9H-4, 25–26	78.60				83
9H-5, 25–26	80.10				93
9H-6, 25–26	81.60				105
9H-7, 25–26	83.10				80
10H-1, 25–26	83.60				74
10H-2, 25–26	85.10				78
10H-3, 25–26	86.60				91
10H-6, 25–26	91.10				101
10H-7, 25–26	92.60				93
11H-1, 25–26	93.10				92
11H-2, 20–21	94.50				98
11H-3, 25–26	96.10				86
11H-4, 25–26	97.60				129
11H-5, 35–36	99.20				110
11H-6, 25–26	101.00				80
11H-7, 76–77	103.00				67
12H-1, 25–26	103.00				65
12H-2, 25–26	104.00				91

Table 13 (continued).

Core, section, interval (cm)	Depth (mbsf)	SN	Vane (kPa)	Res (kPa)	Pen (kPa)
12H-3, 25–26	106.00				86
12H-4, 25–26	107.00				88
12H-5, 25–26	109.00				101
12H-6, 20–21	110.00				66
12H-7, 20–21	112.00				78
13H-1, 25–26	112.00				71
13H-2, 25–26	114.00				105
13H-3, 25–26	115.00				110
13H-4, 33–34	117.00				140
13H-5, 25–26	118.00				103
13H-6, 25–26	120.00				134
13H-7, 30–31	121.00				126
14H-1, 25–26	122.00				88
14H-2, 20–21	123.00				105
14H-3, 25–26	125.00				154
14H-4, 25–26	126.00				130
14H-5, 25–26	128.00				172
14H-6, 25–26	129.00				129
14H-7, 20–21	131.00				105
15H-1, 25–26	131.00				40
15H-2, 46–47	133.00				88
15H-3, 25–26	134.00				120
15H-4, 25–26	136.00				116
15H-5, 22–23	137.00				147
15H-6, 30–31	139.00				154
15H-7, 29–30	140.00				110
16H-1, 19–20	140.00				71
16H-2, 19–20	142.00				49
16H-3, 25–26	144.00				91
16H-4, 25–26	145.00				115
16H-5, 25–26	147.00				145
16H-6, 25–26	148.00				148
16H-7, 25–26	150.00				75
17H-1, 30–31	150.00				152
17H-2, 30–31	152.00				186
17H-3, 30–31	153.00				145
17H-4, 30–31	155.00				145
17H-5, 30–31	156.00				174
17H-6, 30–31	158.00				162
18H-1, 25–26	160.00				93
18H-2, 25–26	161.00				150
18H-3, 25–26	163.00				103
18H-4, 25–26	164.00				159
18H-5, 25–26	166.00				162
18H-6, 25–26	167.00				179
18H-7, 25–26	169.00				123
19H-1, 100–101	170.00				132
19H-2, 20–21	171.00				159
19H-3, 20–21	172.00				108
19H-4, 20–21	174.00				132
19H-5, 20–21	175.00				191
19H-6, 23–24	177.00				159
19H-7, 23–24	178.00				179
20H-1, 27–28	179.00				145
20H-2, 39–40	180.00				167
20H-3, 36–37	182.00				186
20H-4, 36–37	183.00				199
20H-5, 36–37	185.00				196
20H-6, 60–61	186.00				221
20H-7, 39–40	188.00				221
22H-1, 25–26	198.00				147
22H-1, 100–101	198.00				152
22H-2, 25–26	199.00				221
22H-3, 25–26	201.00				221
22H-4, 25–26	202.00				203
22H-6, 25–26	205.00				221
23H-1, 25–26	207.00				211
23H-1, 100–101	208.00				64
23H-2, 25–26	209.00				74
23H-2, 100–101	209.00				83
23H-3, 25–26	210.00				83
23H-3, 100–101	211.00				98
23H-4, 25–26	212.00				88
23H-4, 100–101	212.00				88
23H-5, 25–26	213.00				88
23H-5, 100–101	214.00				78
23H-6, 25–26	215.00				78
23H-6, 100–101	215.00				74
23H-7, 25–26	216.00				74

Notes: SN = numbered spring used to make the measurement. Vane = undrained shear strength; Res = residual shear strength; Pen = unconfined shear strength as measured by the penetrometer.

tivity log is more sensitive to the presence of opal than simple changes in water content would predict. The reason for the response is unclear, but it implies that anomalous resistivity changes could predict the presence of opal in Leg 151 sediments. Fine structure of the porosity profiles matches in both profiles, however, even though the peaks and troughs may be displaced from one another. The secondary variations in bulk density and resistivity must be controlled by periodic variations in porosity.

SEISMIC STRATIGRAPHY

Introduction

At Site 907 a synthetic seismogram was generated from the velocity and density profiles to correlate reflectors in the seismic section to stratigraphic changes. The acoustic impedance profile (the product of density and velocity) and the profile of reflection coefficients (the rate of change of acoustic impedance) were determined both as a function of depth and of two-way acoustic traveltime (TWT). Convolution of the reflection coefficient profile with an assumed source acoustic wavelet resulted in a synthetic seismogram to compare with the measured seismic section.

The seismic section used for correlation is the line ICEP1-89 Segment A, collected by the University of Bergen in July 1989, a single channel seismic record using a 300-in.^{3} air-gun seismic source.

Acoustic Wavelet

We did not have a record of the acoustic wavelet from the ICEP-1 line and, therefore, created a wavelet based upon the strong doublet exhibited at the seafloor. The wavelet used has a 20-ms period with an e-folding attenuation of 14 ms.

Reflection Coefficients

Discrete measurements of density and compressional velocity on the recovered cores (see "Physical Properties" section, this chapter) were combined with logging data to form a profile of reflection coefficients for Hole 907A. In addition, a density of 2.9 g/cm^3 and a velocity of 2.5 km/s were assumed for the basalt penetrated at 216.3 mbsf. The logs provided detailed data on the interval between 83 and 180 mbsf, and a smaller set of discrete shipboard measurements above and below this depth completed the data set. Within the interval common to both logs and shipboard physical properties measurements, we compared the two data sets to assure that they were in agreement. The discrete and logging data matched well over the common interval. Because laboratory- and logging-derived velocities were similar, no adjustment was made to compensate the laboratory data set for changes from in-situ conditions.

The reflection coefficient profile along with the sedimentological units (see "Lithostratigraphy" section, this chapter) is shown in Fig. 49. By far, the strongest reflection coefficients are found at the seafloor and the basalt, with the basalt reflection coefficient being about 40% stronger than that of the seafloor (R_c = 0.46). The upper part of the sediment section (lithostratigraphic Units I to IIIb), which represents the transition from the Miocene biosiliceous section to sediment accumulation under glacial conditions is marked by several relatively strong reflection coefficients.

Synthetic Seismogram

Figure 50 shows the synthetic seismogram resulting from the convolution of the seismic wavelet with the reflection coefficient profile, whereas Figure 51 compares the synthetic seismogram with the recorded seismic section around Site 907. Also shown in Figure 50 are the lithologic unit boundaries translated from depth into equivalent TWT.

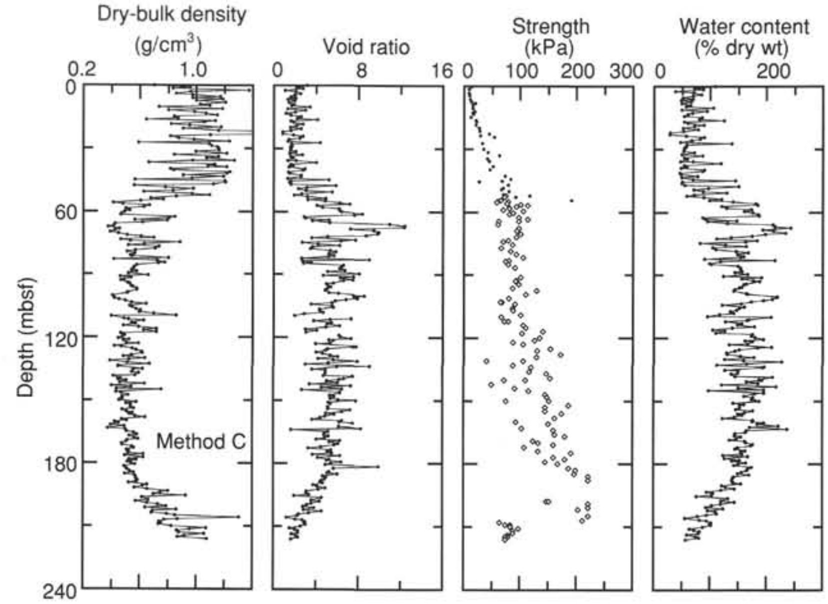

Figure 41. Comparisons of laboratory index property measurements and shear strength vs. depth in Hole 907A. Strength was measured using the mechanical vane (filled circles) above 55 mbsf and using the hand-held penetrometer (open diamonds) below this depth.

A series of acoustic reflectors is found in the upper sediment section (reflectors A–D) and a reflector (E) roughly at the Unit III/IV boundary. Within Unit IV only subdued seismic reflections are produced, until near the Unit IV/V boundary where the sediment loses its biosiliceous component.

Comparison of the synthetic seismogram with the seismic section (Fig. 51) shows that the velocity profile must be nearly correct. The traveltime from seafloor to basalt is predicted well. Reflector E proves to be a boundary in the seismic section between an upper sediment column having a number of coherent reflectors and a lower more transparent sediment column. Tracing this horizon should delineate the top of the upper/middle Miocene biosiliceous sediments on the Iceland Plateau.

Ms 151IR-105

NOTE: For all sites drilled, core-description forms ("barrel sheets") and core photographs can be found in Section 6, beginning on page 465. Forms containing smear-slide data can be found in Section 7, beginning on page 849. Thin-section descriptions are given in Section 8, beginning on page 885, and sediment thin sections in Section 9, beginning on page 895. Dropstone descriptions are included in Section 10, beginning on page 903.

Table 14. Index property measurements from Hole 907A.

Core, section, interval (cm)	Depth (mbsf)	WC-d (%)	WC-w (%)	WBD[a] (g/cm^3)	WBD[b] (g/cm^3)	GD[a] (g/cm^3)	GD[b] (g/cm^3)	DBD[a] (g/cm^3)	DBD[b] (g/cm^3)	Por[a] (%)	Por[b] (%)	VR[a]	VR[b]
151-907A-													
1H-1, 24–26	0.24	108.97	52.15	1.49	1.47	2.92	2.80	0.71	0.70	75.60	74.87	3.10	2.98
1H-1, 99–101	0.99	71.49	41.69	1.67	1.63	3.06	2.84	0.98	0.95	68.04	66.42	2.13	1.98
1H-2, 17–19	1.67	87.99	46.81	1.61	1.57	3.21	2.92	0.85	0.83	73.35	71.49	2.75	2.51
1H-2, 99–101	2.49	38.47	27.78	1.91	1.90	2.85	2.83	1.38	1.37	51.69	51.52	1.07	1.06
1H-3, 20–22	3.20	70.66	41.40	1.68	1.64	3.05	2.83	0.98	0.96	67.74	66.11	2.10	1.95
1H-3, 99–101	3.99	84.17	45.70	1.60	1.58	3.05	2.88	0.87	0.86	71.43	70.26	2.50	2.36
1H-4, 24–26	4.74	69.64	41.05	1.66	1.65	2.92	2.86	0.98	0.97	66.44	66.02	1.98	1.94
1H-4, 102–104	5.52	51.68	34.07	1.85	1.77	3.17	2.84	1.22	1.17	61.50	58.90	1.60	1.43
1H-5, 24–26	6.24	69.48	40.99	1.68	1.65	3.05	2.85	0.99	0.97	67.34	65.87	2.06	1.93
1H-5, 86–88	6.86	47.80	32.34	1.80	1.75	2.80	2.66	1.21	1.19	56.65	55.35	1.31	1.24
2H-1, 25–27	7.55	66.31	39.87	1.70	1.66	3.04	2.83	1.02	1.00	66.27	64.67	1.96	1.83
2H-1, 99–101	8.29	49.00	32.89	1.82	1.79	2.95	2.83	1.22	1.20	58.47	57.53	1.41	1.36
2H-2, 24–26	9.04	64.31	39.14	1.72	1.69	3.06	2.89	1.05	1.03	65.71	64.45	1.92	1.81
2H-2, 99–101	9.79	57.19	36.38	1.75	1.72	2.95	2.81	1.12	1.09	62.21	61.05	1.65	1.57
2H-3, 24–26	10.54	105.20	51.27	1.54	1.51	3.31	3.00	0.75	0.74	77.23	75.50	3.39	3.08
2H-3, 99–101	11.29	48.78	32.79	1.76	1.76	2.72	2.70	1.19	1.18	56.42	56.26	1.29	1.29
2H-4, 24–26	12.04	93.74	48.38	1.59	1.55	3.26	2.97	0.82	0.80	74.87	73.09	2.98	2.72
2H-4, 99–101	12.79	68.39	40.61	1.69	1.66	3.06	2.86	1.01	0.98	67.11	65.64	2.04	1.91
2H-5, 24–26	13.54	59.94	37.48	1.45	1.71	1.93	2.85	0.91	1.07	53.04	62.52	1.13	1.67
2H-5, 99–101	14.29	53.93	35.03	1.80	1.76	3.03	2.89	1.17	1.15	61.44	60.32	1.59	1.52
2H-6, 24–26	15.04	85.26	46.02	1.60	1.56	3.06	2.79	0.86	0.84	71.76	69.85	2.54	2.32
2H-6, 99–101	15.79	80.74	44.67	1.57	1.57	2.78	2.74	0.87	0.87	68.63	68.34	2.19	2.16
2H-7, 24–26	16.54	124.31	55.42	1.49	1.45	3.40	2.98	0.66	0.65	80.47	78.32	4.12	3.61
3H-1, 24–26	17.04	53.70	34.94	1.80	1.74	3.04	2.80	1.17	1.14	61.43	59.49	1.59	1.47
3H-1, 98–100	17.78	60.89	37.85	1.75	1.69	3.10	2.80	1.09	1.05	64.79	62.49	1.84	1.67
3H-2, 24–26	18.54	88.75	47.02	1.60	1.55	3.20	2.82	0.85	0.82	73.46	70.93	2.77	2.44
3H-2, 98–100	19.28	71.62	41.73	1.68	1.63	3.12	2.82	0.98	0.95	68.52	66.35	2.18	1.97
3H-3, 24–26	20.04	51.71	34.09	1.83	1.78	3.09	2.88	1.21	1.17	60.88	59.20	1.56	1.45
3H-3, 98–100	20.78	77.89	43.78	1.69	1.61	3.39	2.88	0.95	0.90	72.03	68.61	2.57	2.19
3H-4, 24–26	21.54	52.51	34.43	1.82	1.76	3.09	2.83	1.20	1.16	61.26	59.17	1.58	1.45
3H-4, 98–100	22.28	28.92	22.43	2.09	1.99	2.99	2.73	1.62	1.54	45.77	43.54	0.84	0.77
3H-5, 24–26	23.04	27.74	21.71	2.09	2.01	2.93	2.75	1.64	1.58	44.25	42.69	0.79	0.75
3H-5, 98–100	23.78	57.31	36.43	1.81	1.73	3.24	2.84	1.15	1.10	64.43	61.39	1.81	1.59
3H-6, 24–26	24.54	89.66	47.27	1.59	1.54	3.12	2.81	0.84	0.81	73.18	71.12	2.73	2.46
3H-6, 98–100	25.28	81.10	44.78	1.63	1.58	3.10	2.84	0.90	0.87	71.03	69.16	2.45	2.24
3H-7, 24–26	26.04	67.33	40.24	1.49	1.64	2.15	2.78	0.89	0.98	58.51	64.58	1.41	1.82
4H-1, 53–55	26.83	46.56	31.77	1.84	1.81	2.91	2.81	1.25	1.24	56.91	56.11	1.32	1.28
4H-1, 99–101	27.29	137.58	57.91	1.44	1.40	3.23	2.86	0.61	0.59	81.22	79.31	4.33	3.84
4H-2, 22–24	28.02	57.69	36.58	1.76	1.72	2.99	2.82	1.11	1.09	62.73	61.37	1.68	1.59
4H-2, 99–101	28.79	57.02	36.31	1.78	1.74	3.09	2.87	1.14	1.11	63.19	61.51	1.72	1.60
4H-3, 23–25	29.53	52.95	34.62	1.80	1.75	3.00	2.81	1.18	1.15	60.76	59.23	1.55	1.45
4H-3, 78–80	30.08	53.73	34.95	1.81	1.77	3.08	2.92	1.18	1.15	61.72	60.52	1.61	1.53
4H-4, 22–24	31.02	52.36	34.37	1.81	1.77	3.02	2.86	1.19	1.16	60.63	59.37	1.54	1.46
4H-4, 78–80	31.58	71.23	41.60	1.67	1.71	3.01	3.24	0.97	1.00	67.63	69.25	2.09	2.25
4H-5, 22–24	32.52	48.82	32.80	1.85	1.81	3.06	2.88	1.24	1.21	59.29	57.85	1.46	1.37
4H-5, 78–80	33.08	86.62	46.41	1.61	1.57	3.19	2.90	0.86	0.84	72.90	71.03	2.69	2.45
4H-6, 24–26	34.04	53.01	34.65	1.81	1.77	3.04	2.87	1.18	1.16	61.11	59.76	1.57	1.49
4H-6, 80–82	34.60	59.67	37.37	1.75	1.71	3.04	2.84	1.10	1.07	63.88	62.31	1.77	1.65
4H-7, 46–48	35.76	46.36	31.67	1.85	1.86	2.94	2.99	1.26	1.27	57.03	57.45	1.33	1.35
5H-1, 25–27	36.05	69.33	40.95	1.70	1.64	3.11	2.83	1.00	0.97	67.79	65.68	2.10	1.91
5H-1, 101–103	36.81	119.35	54.41	1.51	1.45	3.46	2.87	0.69	0.66	80.08	76.94	4.02	3.34
5H-2, 25–27	37.55	53.01	34.65	1.81	1.73	3.07	2.72	1.19	1.13	61.33	58.44	1.59	1.41
5H-2, 104–106	38.34	58.28	36.82	1.77	1.71	3.09	2.81	1.12	1.08	63.69	61.47	1.75	1.60
5H-3, 24–26	39.04	47.80	32.34	1.87	1.80	3.09	2.81	1.26	1.22	58.99	56.71	1.44	1.31
5H-3, 102–104	39.82	89.98	47.36	1.61	1.54	3.34	2.83	0.85	0.81	74.51	71.31	2.92	2.49
5H-4, 19–21	40.49	86.42	46.36	1.62	1.56	3.27	2.82	0.87	0.83	73.38	70.39	2.76	2.38
5H-4, 100–102	41.30	46.12	31.56	1.89	1.81	3.09	2.79	1.29	1.24	58.17	55.65	1.39	1.26
5H-5, 23–25	42.03	47.68	32.29	1.88	1.79	3.14	2.79	1.28	1.21	59.31	56.45	1.46	1.30
5H-5, 115–117	42.95	77.08	43.53	1.69	1.60	3.38	2.83	0.95	0.90	71.76	68.00	2.54	2.13
5H-6, 22–24	43.52	49.32	33.03	2.23	1.78	5.35	2.81	1.50	1.19	72.01	57.45	2.57	1.35
5H-6, 99–101	44.29	68.89	40.79	1.42	1.63	1.93	2.76	0.84	0.97	56.40	64.95	1.29	1.85
5H-7, 17–19	44.97	144.39	59.08	1.45	1.37	3.70	2.70	0.60	0.56	83.86	79.20	5.19	3.81
6H-1, 27–29	45.57	49.77	33.23	1.89	1.80	3.26	2.88	1.26	1.20	61.25	58.28	1.58	1.40
6H-1, 100–102	46.30	49.27	33.01	1.86	1.80	3.11	2.88	1.25	1.21	59.91	58.04	1.49	1.38
6H-2, 24–26	47.04	54.75	35.38	1.78	1.74	3.00	2.80	1.15	1.12	61.53	59.92	1.60	1.50
6H-2, 99–101	47.79	150.77	60.12	1.46	1.40	3.99	3.09	0.58	0.56	85.40	81.97	5.85	4.55
6H-3, 25–27	48.55	95.87	48.94	1.59	1.53	3.34	2.90	0.81	0.78	75.71	73.05	3.12	2.71
6H-3, 101–103	49.31	70.22	41.25	1.73	1.66	3.37	2.96	1.02	0.98	69.74	66.96	2.30	2.03
6H-4, 24–26	50.04	87.53	46.68	1.65	1.56	3.58	2.89	0.88	0.83	75.33	71.17	3.05	2.47
6H-4, 99–101	50.79	128.61	56.26	1.54	1.43	4.42	2.94	0.67	0.63	84.69	78.65	5.53	3.69
6H-5, 24–26	51.54	71.07	41.55	1.78	1.66	3.77	2.96	1.04	0.97	72.32	67.21	2.61	2.05
6H-5, 99–101	52.29	58.46	36.89	1.82	1.73	3.33	2.91	1.15	1.09	65.48	62.41	1.90	1.66
6H-6, 22–24	53.02	88.97	47.08	1.65	1.61	3.64	3.29	0.87	0.85	75.92	74.06	3.15	2.86
6H-6, 99–101	53.79	120.16	54.58	1.56	1.48	4.21	3.20	0.71	0.67	83.13	78.97	4.93	3.76
6H-7, 25–27	54.55	98.54	49.63	1.58	1.52	3.36	2.90	0.79	0.77	76.35	73.60	3.23	2.79
7H-1, 24–26	55.04	139.71	58.28	1.46	1.45	3.57	3.39	0.61	0.60	82.92	82.20	4.85	4.62
7H-1, 100–102	55.80	181.03	64.42	1.37	1.15	3.54	1.49	0.49	0.41	86.18	72.53	6.24	2.64
7H-2, 24–26	56.54	184.05	64.80	1.39	1.35	4.00	3.28	0.49	0.48	87.74	85.47	7.16	5.88
7H-2, 99–101	57.29	119.55	54.45	1.51	1.46	3.49	3.00	0.69	0.67	80.23	77.78	4.06	3.50
7H-3, 24–26	58.04	129.53	56.43	1.49	1.43	3.65	2.94	0.65	0.62	82.15	78.76	4.60	3.71
7H-3, 102–104	58.82	172.11	63.25	1.39	1.36	3.67	3.14	0.51	0.50	86.01	84.06	6.15	5.28
7H-4, 24–26	59.54	160.07	61.55	1.43	1.37	4.00	3.01	0.55	0.53	86.16	82.45	6.23	4.70
7H-4, 99–101	60.29	174.46	63.56	1.40	1.35	3.79	2.97	0.51	0.49	86.53	83.46	6.42	5.05
7H-5, 25–27	61.05	185.43	64.96	1.41	1.34	4.64	3.05	0.49	0.47	89.30	84.67	8.35	5.52
7H-5, 99–101	61.79	186.58	65.11	1.39	1.33	4.18	3.07	0.49	0.47	88.34	84.83	7.57	5.59
7H-6, 24–26	62.54	86.04	46.25	1.64	1.57	3.42	2.92	0.88	0.85	74.13	71.00	2.87	2.45
7H-6, 90–92	63.20	91.40	47.75	1.60	1.54	3.33	2.88	0.84	0.81	74.77	71.94	2.96	2.57
7H-7, 25–27	64.05	146.94	59.51	1.45	1.39	3.64	2.90	0.59	0.56	83.90	80.61	5.21	4.16

Table 14 (continued).

Core, section, interval (cm)	Depth (mbsf)	WC-d (%)	WC-w (%)	WBD[a] (g/cm^3)	WBD[b] (g/cm^3)	GD[a] (g/cm^3)	GD[b] (g/cm^3)	DBD[a] (g/cm^3)	DBD[b] (g/cm^3)	Por[a] (%)	Por[b] (%)	VR[a]	VR[b]
8H-1, 28–30	64.58	95.03	48.73	1.65	1.54	3.92	2.95	0.85	0.79	78.38	73.20	3.62	2.73
8H-1, 101–103	65.31	130.43	56.60	1.52	1.42	4.61	2.88	0.66	0.62	84.07	78.56	5.28	3.67
8H-2, 20–22	66.00	211.08	67.85	1.38	1.32	5.34	3.41	0.44	0.43	91.63	87.55	10.94	7.04
8H-2, 99–101	66.79	214.78	68.23	1.39	1.30	5.94	3.16	0.44	0.41	92.52	86.89	12.37	6.63
8H-3, 20–22	67.50	242.10	70.77	1.34	1.29	5.25	3.40	0.39	0.38	92.50	88.91	12.33	8.02
8H-3, 99–101	68.29	193.18	65.89	1.37	1.34	3.87	3.26	0.47	0.46	87.90	85.99	7.26	6.14
8H-4, 21–23	69.01	211.64	67.91	1.37	1.31	4.61	3.23	0.44	0.42	90.44	86.97	9.47	6.68
8H-4, 99–101	69.79	233.44	70.01	1.33	1.29	4.39	3.35	0.40	0.39	90.87	88.40	9.95	7.62
8H-5, 24–26	70.54	197.64	66.40	1.40	1.33	5.12	3.16	0.47	0.45	90.77	85.92	9.83	6.10
8H-5, 99–101	71.29	174.04	63.51	1.45	1.39	5.16	3.70	0.53	0.51	89.72	86.26	8.73	6.28
8H-6, 21–23	72.01	137.27	57.85	1.48	1.44	3.80	3.29	0.62	0.61	83.53	81.50	5.07	4.41
8H-6, 99–101	72.79	110.68	52.54	1.53	1.47	3.34	2.82	0.72	0.70	78.29	75.25	3.61	3.04
8H-7, 27–29	73.57	182.63	64.62	1.40	1.31	4.35	2.71	0.50	0.46	88.53	82.82	7.72	4.82
9H-1, 25–27	74.05	162.96	61.97	1.43	1.40	3.99	3.40	0.54	0.53	86.35	84.40	6.33	5.41
9H-1, 99–101	74.79	82.23	45.12	1.66	1.61	3.39	3.03	0.91	0.88	73.06	70.82	2.71	2.43
9H-2, 25–27	75.55	126.59	55.87	1.48	1.43	3.41	2.85	0.65	0.63	80.76	77.85	4.20	3.52
9H-2, 99–101	76.29	163.88	62.10	1.42	1.37	3.91	3.05	0.54	0.52	86.16	82.99	6.23	4.88
9H-3, 25–27	77.05	104.78	51.17	1.57	1.50	3.59	2.94	0.77	0.73	78.54	75.06	3.66	3.01
9H-3, 99–101	77.79	110.06	52.39	1.52	1.49	3.23	2.94	0.72	0.71	77.57	75.97	3.46	3.16
9H-4, 25–27	78.55	146.30	59.40	1.45	1.39	3.73	2.95	0.59	0.57	84.14	80.81	5.30	4.21
9H-4, 99–101	79.29	167.55	62.62	1.40	1.36	3.61	2.97	0.52	0.51	85.49	82.91	5.89	4.85
9H-5, 49–51	80.29	148.13	59.70	1.44	1.39	3.58	2.97	0.58	0.56	83.77	81.10	5.16	4.29
9H-5, 123–125	81.03	159.00	61.39	1.42	1.38	3.68	3.04	0.55	0.53	85.07	82.49	5.70	4.71
9H-6, 25–27	81.55	153.37	60.53	1.42	1.38	3.48	2.99	0.56	0.55	83.84	81.74	5.19	4.48
9H-6, 99–101	82.29	89.21	47.15	1.57	1.52	3.02	2.66	0.83	0.80	72.41	69.84	2.62	2.32
9H-7, 25–27	83.05	214.37	68.19	1.35	1.30	4.35	3.13	0.43	0.41	90.05	86.74	9.05	6.54
10H-1, 25–27	83.55	117.43	54.01	1.38	1.56	2.35	4.07	0.64	0.72	72.85	82.35	2.68	4.67
10H-1, 99–101	84.29	98.55	49.64	1.61	1.54	3.69	3.03	0.81	0.77	77.99	74.45	3.54	2.92
10H-2, 8–10	84.88	101.84	50.46	1.50	1.47	2.82	2.64	0.74	0.73	73.65	72.43	2.80	2.63
10H-2, 99–101	85.79	148.76	59.80	1.49	1.43	4.56	3.49	0.60	0.58	86.82	83.51	6.59	5.07
10H-3, 24–26	86.54	154.07	60.64	1.46	1.42	4.27	3.48	0.58	0.56	86.48	83.96	6.40	5.24
10H-3, 99–101	87.29	154.11	60.65	1.46	1.41	4.13	3.36	0.57	0.56	86.10	83.49	6.19	5.06
10H-4, 24–26	88.04	156.07	60.95	1.46	1.39	4.40	3.10	0.57	0.54	86.98	82.50	6.68	4.72
10H-4, 103–105	88.83	143.84	58.99	1.45	1.41	3.61	3.03	0.59	0.58	83.49	80.96	5.06	4.25
10H-5, 47–49	89.77	166.01	62.41	1.46	1.38	5.01	3.19	0.55	0.52	88.99	83.78	8.08	5.17
10H-5, 123–125	90.53	123.40	55.24	1.53	1.47	3.89	3.13	0.68	0.66	82.37	79.01	4.67	3.77
10H-6, 24–26	91.04	191.18	65.66	1.38	1.34	4.06	3.27	0.47	0.46	88.29	85.92	7.54	6.10
10H-6, 99–101	91.79	155.90	60.92	1.45	1.37	4.14	2.93	0.57	0.54	86.26	81.65	6.28	4.45
10H-7, 40–42	92.70	176.23	63.80	1.42	1.34	4.35	2.96	0.51	0.49	88.17	83.59	7.45	5.09
11H-1, 26–28	93.06	187.03	65.16	1.37	1.33	3.63	2.97	0.48	0.46	86.83	84.42	6.59	5.42
11H-1, 127–129	94.07	164.17	62.15	1.40	1.36	3.51	2.97	0.53	0.52	84.85	82.62	5.60	4.76
11H-2, 24–26	94.54	159.38	61.45	1.39	1.37	3.19	2.90	0.54	0.53	83.20	81.86	4.95	4.52
11H-2, 125–127	95.55	156.27	60.98	1.41	1.37	3.38	2.90	0.55	0.54	83.71	81.57	5.14	4.43
11H-3, 24–26	96.04	151.56	60.25	1.43	1.39	3.64	2.98	0.57	0.55	84.30	81.50	5.37	4.41
11H-3, 127–129	97.07	143.79	58.98	1.45	1.40	3.58	3.01	0.59	0.58	83.38	80.87	5.02	4.23
11H-4, 24–26	97.54	141.94	58.67	1.45	1.39	3.51	2.85	0.60	0.58	82.92	79.79	4.85	3.95
11H-4, 127–129	98.57	163.67	62.07	1.38	1.36	3.26	2.89	0.53	0.51	83.84	82.20	5.19	4.62
11H-5, 23–25	99.03	166.45	62.47	1.41	1.36	3.77	2.98	0.53	0.51	85.93	82.85	6.11	4.83
11H-5, 127–129	100.07	218.96	68.65	1.34	1.29	4.02	3.04	0.42	0.41	89.52	86.67	8.54	6.50
11H-6, 23–25	100.53	217.87	68.54	1.32	1.30	3.55	3.08	0.42	0.41	88.27	86.75	7.52	6.55
11H-6, 113–115	101.43	210.18	67.76	1.34	1.30	3.86	3.00	0.43	0.42	88.74	86.01	7.88	6.15
11H-7, 11–13	101.91	194.45	66.04	1.35	1.33	3.62	3.11	0.46	0.45	87.24	85.52	6.84	5.91
12H-1, 28–30	102.58	172.30	63.28	1.38	1.35	3.46	2.98	0.51	0.50	85.28	83.37	5.79	5.02
12H-1, 124–126	103.54	155.00	60.78	1.43	1.38	3.64	3.00	0.56	0.54	84.59	81.96	5.49	4.55
12H-2, 28–30	104.08	120.80	54.71	1.46	1.42	2.98	2.64	0.66	0.64	77.78	75.68	3.50	3.11
12H-2, 125–127	105.05	160.68	61.64	1.41	1.37	3.54	2.96	0.54	0.52	84.69	82.28	5.53	4.65
12H-3, 27–29	105.57	151.13	60.18	1.45	1.37	3.81	2.80	0.58	0.55	84.87	80.52	5.61	4.14
12H-3, 131–133	106.61	147.17	59.54	1.40	1.41	3.01	3.19	0.57	0.57	81.18	82.08	4.31	4.58
12H-4, 27–29	107.07	135.81	57.59	1.45	1.43	3.30	3.06	0.61	0.61	81.36	80.22	4.36	4.06
12H-4, 127–129	108.07	141.08	58.52	1.44	1.43	3.41	3.22	0.60	0.59	82.41	81.61	4.68	4.44
12H-5, 27–29	108.57	115.86	53.67	1.41	1.51	2.53	3.33	0.66	0.70	74.05	79.01	2.85	3.77
12H-5, 129–131	109.59	95.70	48.90	1.38	1.67	2.07	4.23	0.71	0.85	65.87	79.78	1.93	3.95
12H-6, 19–21	109.99	207.87	67.52	1.48	1.22		1.98	0.48	0.39	97.32	80.09		4.02
12H-6, 127–129	111.07	168.16	62.71	1.44	1.31	4.46	2.43	0.54	0.49	87.93	79.92	7.29	3.98
12H-7, 19–21	111.49	164.51	62.19	1.39	1.38	3.333	3.15	0.52	0.52	84.18	83.47	5.32	5.05
13H-1, 24–26	112.04	126.57	55.86	1.45	1.42	3.04	2.77	0.64	0.63	78.91	77.38	3.74	3.42
13H-1, 123–125	113.03	155.41	60.85	1.42	1.37	3.61	2.92	0.56	0.54	84.53	81.55	5.46	4.42
13H-2, 24–26	113.54	148.08	59.69	1.43	1.40	3.48	3.11	0.58	0.57	83.39	81.80	5.02	4.50
13H-2, 123–125	114.53	178.20	64.06	1.38	1.34	3.58	2.91	0.50	0.48	86.13	83.51	6.21	5.07
13H-3, 24–26	115.04	138.65	58.10	1.46	1.41	3.62	2.91	0.61	0.59	83.02	79.76	4.89	3.94
13H-3, 124–126	116.04	104.65	51.14	1.50	1.47	2.93	2.67	0.73	0.72	74.90	73.13	2.98	2.72
13H-4, 24–26	116.54	126.06	55.76	1.48	1.42	3.31	2.76	0.65	0.63	80.26	77.22	4.07	3.39
13H-4, 125–127	117.55	110.06	52.40	1.47	1.50	2.85	3.09	0.70	0.72	75.33	76.86	3.05	3.32
13H-5, 24–26	118.04	175.33	63.68	1.49	1.28		2.28	0.54	0.47	92.49	79.56		3.89
13H-5, 123–125	119.03	172.64	63.32	1.39	1.34	3.67	2.89	0.51	0.49	86.04	82.94	6.16	4.86
13H-6, 24–26	119.54	179.23	64.19	1.38	1.34	3.60	2.96	0.49	0.48	86.26	83.79	6.28	5.17
13H-6, 124–126	120.54	193.85	65.97	1.37	1.31	3.87	2.86	0.47	0.45	87.95	84.42	7.30	5.42
13H-7, 24–26	121.04	161.77	61.80	1.39	1.37	3.30	3.01	0.53	0.52	83.87	82.59	5.20	4.75
14H-1, 25–27	121.55	174.78	63.61	1.37	1.33	3.30	2.74	0.50	0.48	84.88	82.37	5.61	4.68
14H-1, 125–127	122.55	165.57	62.34	1.38	1.34	3.30	2.78	0.52	0.51	84.16	81.79	5.31	4.49
14H-2, 19–21	122.99	133.41	57.16	1.43	1.37	3.30	2.53	0.61	0.59	79.75	76.69	3.94	3.29
14H-2, 131–133	124.11	209.10	67.65	1.34	1.29	3.84	2.80	0.43	0.42	88.64	85.09	7.80	5.71
14H-3, 23–25	124.53	183.74	64.76	1.40	1.32	4.19	2.85	0.49	0.47	88.21	83.63	7.48	5.11
14H-3, 123–125	125.53	151.22	60.19	1.42	1.37	3.47	2.80	0.57	0.55	83.61	80.51	5.10	4.13
14H-4, 25–27	126.05	143.11	58.87	1.45	1.39	3.51	2.80	0.59	0.57	83.02	79.65	4.89	3.92
14H-4, 119–121	126.99	128.39	56.22	1.46	1.39	3.21	2.60	0.64	0.61	80.06	76.50	4.02	3.26
14H-5, 25–27	127.55	129.73	56.47	1.49	1.42	3.63	2.86	0.65	0.62	82.11	78.35	4.59	3.62
14H-5, 118–120	128.48	154.21	60.66	1.42	1.37	3.56	2.82	0.56	0.54	84.21	80.93	5.33	4.25
14H-6, 25–27	129.05	177.76	64.00	1.37	1.33	3.05	2.88	0.49	0.48	85.80	83.30	6.04	4.99

Table 14 (continued).

Core, section, interval (cm)	Depth (mbsf)	WC-d (%)	WC-w (%)	WBD[a] (g/cm^3)	WBD[b] (g/cm^3)	GD[a] (g/cm^3)	GD[b] (g/cm^3)	DBD[a] (g/cm^3)	DBD[b] (g/cm^3)	Por[a] (%)	Por[b] (%)	VR[a]	VR[b]
14H-6, 118–120	129.98	125.47	55.65	1.49	1.43	3.42	2.83	0.66	0.63	80.67	77.59	4.17	3.46
14H-7, 20–22	130.50	159.38	61.45	1.42	1.35	3.62	2.76	0.55	0.52	84.87	81.09	5.61	4.29
15H-1, 25–27	131.05	227.13	69.43	1.31	1.28	3.57	2.87	0.40	0.39	88.74	86.41	7.88	6.36
15H-1, 126–128	132.06	164.67	62.22	1.38	1.34	3.22	2.76	0.52	0.51	83.75	81.61	5.15	4.44
15H-2, 26–28	132.56	111.66	52.75	1.45	1.41	2.72	2.44	0.69	0.67	74.74	72.69	2.96	2.66
15H-2, 126–128	133.56	196.37	66.26	1.39	1.32	4.77	2.97	0.47	0.44	90.09	85.04	9.10	5.69
15H-3, 23–25	134.03	193.45	65.92	1.33	1.31	3.18	2.89	0.45	0.45	85.70	84.51	5.99	5.46
15H-3, 127–129	135.07	126.73	55.89	1.44	1.41	2.94	2.67	0.63	0.62	78.39	76.78	3.63	3.31
15H-4, 23–25	135.53	149.85	59.98	1.42	1.39	3.36	2.97	0.57	0.56	83.05	81.27	4.90	4.34
15H-4, 127–129	136.57	149.60	59.94	1.42	1.36	3.35	2.69	0.57	0.55	82.99	79.68	4.88	3.92
15H-5, 23–25	137.03	138.20	58.02	1.47	1.41	3.63	2.94	0.62	0.59	82.99	79.88	4.88	3.97
15H-5, 128–130	138.08	144.35	59.07	1.43	1.38	3.38	2.79	0.59	0.57	82.59	79.69	4.74	3.93
15H-6, 22–24	138.52	211.30	67.88	1.33	1.29	3.64	2.86	0.43	0.41	88.20	85.51	7.48	5.90
15H-6, 127–129	139.57	187.26	65.19	1.37	1.33	3.65	2.95	0.48	0.46	86.92	84.33	6.65	5.39
15H-7, 28–30	140.08	191.65	65.71	1.34	1.33	3.32	2.69	0.46	0.45	86.08	83.40	6.18	5.03
16H-1, 18–20	140.48	164.69	62.22	1.37	1.34	3.15	2.67	0.52	0.50	83.46	81.07	5.05	4.29
16H-1, 125–127	141.55	185.08	64.92	1.35	1.30	3.34	2.62	0.47	0.46	85.74	82.58	6.01	4.74
16H-2, 19–21	141.99	121.48	54.85	1.45	1.41	2.09	2.57	0.65	0.64	77.41	75.31	3.43	3.05
16H-2, 126–128	143.06	217.48	68.50	1.32	1.27	3.46	2.66	0.41	0.40	87.98	84.96	7.32	5.65
16H-3, 18–20	143.48	149.96	59.99	1.40	1.35	3.13	2.55	0.56	0.54	82.05	78.88	4.57	3.74
16H-3, 125–127	144.55	195.44	66.15	1.34	1.29	3.40	2.66	0.45	0.44	86.61	83.55	6.47	5.08
16H-4, 16–18	144.96	97.59	49.39	1.51	1.48	2.82	2.62	0.76	0.75	72.82	71.35	2.68	2.49
16H-4, 125–127	146.05	195.85	66.20	1.34	1.28	3.30	2.48	0.45	0.43	86.28	82.57	6.29	4.74
16H-5, 17–19	146.47	178.81	64.13	1.38	1.30	3.61	2.51	0.49	0.47	86.25	81.43	6.27	4.39
16H-5, 125–127	147.55	160.14	61.56	1.40	1.34	3.39	2.68	0.54	0.52	84.09	80.71	5.29	4.19
16H-6, 17–19	147.97	176.19	63.79	1.37	1.32	3.37	2.64	0.50	0.48	85.22	81.96	5.77	4.54
16H-6, 126–128	149.06	174.33	63.55	1.36	1.31	3.17	2.58	0.50	0.48	84.30	81.45	5.37	4.39
16H-7, 25–27	149.55	180.52	64.35	1.37	1.30	3.46	2.49	0.49	0.46	85.88	81.42	6.08	4.38
17H-1, 25–27	150.05	187.22	65.18	1.39	1.30	4.28	2.63	0.49	0.45	88.62	82.77	7.79	4.81
17H-1, 99–101	150.79	141.23	58.55	1.47	1.38	3.80	2.74	0.61	0.57	83.92	79.06	5.22	3.78
17H-2, 25–27	151.55	160.61	61.63	1.40	1.31	3.46	2.40	0.54	0.50	84.37	79.02	5.40	3.77
17H-2, 99–101	152.29	152.49	60.39	1.69	1.35		2.66	0.67	0.54	99.45	79.84		3.96
17H-3, 25–27	153.05	152.23	60.35	1.42	1.36	3.46	2.66	0.56	0.54	83.66	79.82	5.12	3.96
17H-3, 99–101	153.79	145.99	59.35	1.45	1.37	3.61	2.68	0.59	0.56	83.68	79.25	5.13	3.82
17H-4, 25–27	154.55	175.55	63.71	1.41	1.31	4.25	2.61	0.51	0.48	87.89	81.70	7.26	4.47
17H-4, 99–101	155.29	161.26	61.72	1.44	1.33	4.01	2.56	0.55	0.51	86.54	80.10	6.43	4.03
17H-5, 25–27	156.05	148.85	59.81	1.43	1.36	3.41	2.66	0.57	0.55	83.16	79.43	4.94	3.86
17H-5, 99–101	156.79	156.81	61.06	1.43	1.35	3.78	2.67	0.56	0.53	85.20	80.33	5.76	4.09
17H-6, 25–27	157.55	143.29	58.90	1.44	1.38	3.48	2.75	0.59	0.57	82.91	79.37	4.85	3.85
17H-6, 99–101	158.29	122.66	55.09	1.52	1.42	3.68	2.71	0.68	0.64	81.47	76.40	4.40	3.24
17H-7, 25–27	159.05	175.93	63.76	1.26	1.30	2.13	2.52	0.46	0.47	78.47	81.20	3.65	4.32
18H-1, 25–27	159.55	175.09	63.65	1.39	1.40	3.80	3.92	0.51	0.51	86.62	87.00	6.47	6.69
18H-1, 99–101	160.29	195.79	66.19	1.33	1.26	3.25	2.30	0.45	0.43	86.09	81.43	6.19	4.39
18H-2, 25–27	161.05	184.17	64.81	1.39	1.28	4.16	2.33	0.49	0.45	88.17	80.70	7.45	4.18
18H-2, 99–101	161.79	221.29	68.88	1.43	1.27		2.68	0.45	0.39	96.26	85.26		5.79
18H-3, 25–27	162.55	170.24	63.00	1.40	1.32	3.72	2.63	0.52	0.49	86.04	81.35	6.17	4.36
18H-3, 97–99	163.27	236.87	70.32	1.30	1.26	3.58	2.74	0.39	0.37	89.19	86.34	8.25	6.32
18H-4, 25–27	164.05	164.40	62.18	1.03	1.32	1.04	2.47	0.39	0.50	62.42	79.84	1.66	3.96
18H-4, 99–101	164.79	162.66	61.93	1.38	1.34	3.24	2.67	0.53	0.51	83.68	80.93	5.13	4.24
18H-5, 25–27	165.55	144.78	59.15	1.44	1.37	3.44	2.68	0.59	0.56	82.91	79.12	4.85	3.79
18H-5, 99–101	166.29	143.22	58.89	1.44	1.41	3.43	3.07	0.59	0.58	82.69	81.08	4.78	4.29
18H-6, 25–27	167.05	154.92	60.77	1.41	1.35	3.40	2.65	0.55	0.53	83.82	79.99	5.18	4.00
18H-6, 99–101	167.79	146.51	59.43	1.43	1.38	3.40	2.85	0.58	0.56	82.91	80.27	4.85	4.07
18H-7, 25–27	168.55	133.94	57.25	1.44	1.38	3.10	2.59	0.61	0.59	80.19	77.20	4.05	3.39
19H-1, 25–27	169.05	161.56	61.77	1.43	1.34	3.98	2.69	0.55	0.51	86.21	80.91	6.25	4.24
19H-1, 99–101	169.79	163.72	62.08	1.39	1.33	3.31	2.60	0.53	0.50	84.05	80.60	5.27	4.16
19H-2, 25–27	170.55	176.23	63.80	1.38	1.30	3.57	2.48	0.50	0.47	85.95	81.02	6.12	4.27
19H-2, 99–101	171.29	172.55	63.31	1.38	1.30	3.42	2.46	0.51	0.48	85.15	80.57	5.73	4.15
19H-3, 25–27	172.05	149.02	59.84	1.40	1.36	3.07	2.62	0.56	0.54	81.66	79.20	4.45	3.81
19H-3, 99–101	172.79	144.01	59.02	1.33	1.37	2.35	2.63	0.55	0.56	76.73	78.69	3.30	3.69
19H-4, 25–27	173.55	162.61	61.92	1.40	1.33	3.44	2.59	0.53	0.51	84.50	80.43	5.45	4.11
19H-4, 99–101	174.29	154.80	60.75	1.41	1.33	3.39	2.51	0.55	0.52	83.63	79.12	5.11	3.79
19H-5, 25–27	175.05	157.55	61.17	1.42	1.33	3.57	2.52	0.55	0.52	84.54	79.49	5.47	3.88
19H-5, 99–101	175.79	123.45	55.25	1.46	1.40	3.07	2.55	0.65	0.63	78.67	75.43	3.69	3.07
19H-6, 25–27	176.55	167.72	62.65	1.41	1.33	3.85	2.64	0.53	0.50	86.27	81.19	6.28	4.32
19H-6, 99–101	177.29	125.50	55.65	1.49	1.41	3.43	2.68	0.66	0.63	80.73	76.65	4.19	3.28
19H-7, 25–27	178.05	152.11	60.34	1.43	1.33	3.54	2.47	0.57	0.53	83.96	78.55	5.23	3.66
20H-1, 24–26	178.54	139.30	58.21	1.47	1.38	3.68	2.66	0.61	0.58	83.32	78.35	4.99	3.62
20H-1, 99–101	179.29	163.79	62.09	1.43	1.35	4.03	2.84	0.54	0.51	86.51	81.95	6.41	4.54
20H-2, 24–26	180.04	149.81	59.97	1.44	1.35	3.72	2.57	0.58	0.54	84.42	78.98	5.42	3.76
20H-2, 99–101	180.79	142.87	58.83	1.45	1.38	3.53	2.76	0.60	0.57	83.06	79.39	4.90	3.85
20H-3, 24–26	181.54	173.64	63.46	1.47	1.35	5.89	3.00	0.54	0.49	90.84	83.55	9.92	5.08
20H-3, 99–101	182.29	167.60	62.63	1.39	1.35	3.49	2.92	0.52	0.51	85.04	82.69	5.69	4.78
20H-4, 24–26	183.04	165.20	62.29	1.59	1.36		3.00	0.60	0.51	96.47	82.85		4.83
20H-4, 99–101	183.79	155.73	60.90	1.41	1.35	3.46	2.72	0.55	0.53	84.00	80.51	5.25	4.13
20H-5, 25–27	184.55	148.74	59.80	1.43	1.39	3.52	2.94	0.58	0.56	83.58	81.00	5.09	4.27
20H-5, 99–101	185.29	169.52	62.90	1.40	1.33	3.64	2.72	0.52	0.49	85.73	81.84	6.01	4.51
20H-6, 25–27	186.05	142.04	58.68	1.44	1.38	3.37	2.68	0.59	0.57	82.35	78.79	4.67	3.72
20H-6, 99–101	186.79	140.01	58.33	1.46	1.37	3.3	2.61	0.61	0.57	83.18	78.10	4.95	3.57
20H-7, 25–27	187.55	139.59	58.26	1.46	1.38	3.57	2.64	0.61	0.57	82.92	78.22	4.85	3.59
21H-1, 25–27	188.05	138.78	58.12	1.45	1.40	3.36	2.83	0.61	0.59	81.93	79.28	4.54	3.83
21H-1, 99–101	188.79	141.51	58.59	1.43	1.39	3.22	2.79	0.59	0.57	81.62	79.38	4.44	3.85
21H-2, 25–27	189.55	155.18	60.81	1.39	1.33	3.07	2.51	0.54	0.52	82.26	79.19	4.64	3.81
21H-2, 99–101	190.29	121.04	54.76	1.48	1.44	3.19	2.81	0.67	0.65	79.02	76.83	3.77	3.32
21H-3, 25–27	191.05	127.71	56.09	1.47	1.41	3.32	2.72	0.65	0.62	80.52	77.24	4.13	3.40
21H-3, 99–101	191.79	143.91	59.00	1.44	1.38	3.50	2.73	0.59	0.57	83.04	79.33	4.90	3.84
21H-4, 25–27	192.55	120.52	54.65	1.52	1.44	3.63	2.81	0.69	0.65	81.01	76.75	4.26	3.30
21H-4, 99–101	193.29	93.57	48.34	1.60	1.56	3.39	3.02	0.83	0.80	75.54	73.39	3.09	2.76
21H-5, 25–27	194.05	105.02	51.22	1.51	1.53	3.04	3.20	0.74	0.75	75.69	76.61	3.11	3.28

Table 14 (continued).

Core, section, interval (cm)	Depth (mbsf)	WC-d (%)	WC-w (%)	WBD[a] (g/cm³)	WBD[b] (g/cm³)	GD[a] (g/cm³)	GD[b] (g/cm³)	DBD[a] (g/cm³)	DBD[b] (g/cm³)	Por[a] (%)	Por[b] (%)	VR[a]	VR[b]
21H-5, 99–101	194.79	102.50	50.62	1.56	1.42	3.32	2.33	0.77	0.70	76.84	69.94	3.32	2.33
21H-6, 25–27	195.55	75.92	43.16	1.57	1.63	2.64	2.97	0.89	0.93	66.11	68.73	1.95	2.20
21H-6, 99–101	196.29	131.65	56.83	1.48	1.43	3.52	2.95	0.64	0.62	81.85	79.14	4.51	3.80
22H-1, 25–27	197.55	120.15	54.58	1.47	1.45	3.07	2.94	0.67	0.66	78.20	77.49	3.59	3.44
22H-1, 99–101	198.29	143.10	58.86	1.42	1.39	3.14	2.87	0.58	0.57	81.38	80.02	4.37	4.01
22H-2, 25–27	199.05	118.46	54.23	1.48	1.43	3.10	2.68	0.68	0.65	78.17	75.61	3.58	3.10
22H-2, 99–101	199.79	103.19	50.79	1.53	1.48	3.14	2.76	0.75	0.73	75.93	73.57	3.15	2.78
22H-3, 25–27	200.55	92.77	48.12	1.57	1.52	3.12	2.76	0.82	0.79	73.80	71.43	2.82	2.50
22H-3, 99–101	201.29	123.73	55.30	1.47	1.43	3.19	2.82	0.66	0.64	79.33	77.30	3.84	3.41
22H-4, 25–27	202.05	95.90	48.95	1.55	1.68	3.02	4.34	0.79	0.86	73.85	80.24	2.82	4.06
22H-4, 99–101	202.79	109.46	52.26	1.61	1.46	4.26	2.70	0.77	0.70	81.94	74.26	4.54	2.89
22H-5, 25–27	203.55	111.67	52.76	1.50	1.45	3.08	2.72	0.71	0.69	77.04	74.75	3.35	2.96
22H-5, 99–101	204.29	94.34	48.54	1.49	1.54	2.62	2.95	0.77	0.79	70.66	73.06	2.41	2.71
22H-6, 25–27	205.05	78.94	44.12	1.61	1.52	2.93	2.46	0.90	0.85	69.29	65.46	2.26	1.90
22H-6, 99–101	205.79	55.75	35.80	1.60	2.03	2.32	4.48	1.02	1.30	55.74	70.93	1.26	2.44
22H-7, 25–27	206.55	81.70	44.96	1.54	1.58	2.63	2.82	0.85	0.87	67.70	69.18	2.10	2.25
23H-1, 25–27	207.05	94.75	48.65	1.55	1.51	2.99	2.72	0.79	0.77	73.39	71.57	2.76	2.52
23H-1, 99–101	207.79	101.50	50.37	1.52	1.48	3.02	2.73	0.76	0.74	74.92	72.98	2.99	2.70
23H-2, 25–27	208.55	99.36	49.84	1.53	1.50	3.03	2.79	0.77	0.75	74.55	72.99	2.93	2.70
23H-2, 99–101	209.29	101.90	50.47	1.53	1.48	3.09	2.74	0.76	0.74	75.42	73.13	3.07	2.72
23H-3, 25–27	210.05	87.20	46.58	1.58	1.54	3.02	2.74	0.85	0.82	71.96	69.95	2.57	2.33
23H-3, 99–101	210.79	63.40	38.80	1.60	1.75	2.47	3.18	0.98	1.07	60.43	66.26	1.53	1.97
23H-4, 25–27	211.55	71.24	41.60	1.66	1.63	2.96	2.81	0.97	0.95	67.24	66.14	2.05	1.95
23H-4, 99–101	212.29	81.06	44.77	1.61	1.57	2.97	2.74	0.89	0.86	70.11	68.39	2.35	2.16
23H-5, 25–27	213.05	79.47	44.28	1.62	1.57	3.01	2.73	0.90	0.88	69.99	67.95	2.33	2.12
23H-5, 99–101	213.79	59.42	37.27	1.74	1.69	2.97	2.74	1.09	1.06	63.21	61.38	1.72	1.59
23H-6, 25–27	214.55	74.52	42.70	1.64	1.60	3.00	2.77	0.94	0.92	68.51	66.81	2.18	2.01
23H-6, 99–101	215.29	80.08	44.47	1.61	1.57	2.97	2.72	0.89	0.87	69.89	68.02	2.32	2.13
23H-7, 25–27	216.05	57.27	36.42	1.74	1.69	2.92	2.69	1.11	1.08	61.94	60.09	1.63	1.51

Notes: WC-d = dry water content (% dry sample weight); WC-w = wet water content (% wet sample weight); WBD = wet-bulk density; GD = grain density; DBD = dry-bulk density; Por = porosity; VR = void ratio.
[a]Value calculated using Method B.
[b]Value calculated using Method C.

Table 15. Index properties of lithologic units defined for Hole 907A.

Unit		WC-w (%)	WC-d (%)	WBD[a] (g/cm³)	DBD[b] (g/cm³)	GD[b] (g/cm³)	Por[a] (%)	VR[a]
I	N (23)	41.04	72.06	1.67	0.98	2.85	66.24	2.12
0–16.8	Min	27.78	38.47	1.45	0.65	2.66	51.69	1.07
mbsf	Max	55.42	124.31	1.91	1.37	3.01	80.47	4.12
	SE	1.47	4.52	0.03	0.04	0.02	1.61	0.16
II	N(54)	41.08	74.24	1.72	0.99	2.86	67.51	2.43
16.8–56.3	Min	21.71	27.74	1.37	0.41	1.50	44.25	0.79
mbsf	Max	64.42	181.03	2.36	1.58	3.39	86.18	6.24
	SE	1.28	4.44	0.02	0.03	0.03	1.31	0.18
IIIA	N(52)	59.74	154.56	1.45	0.57	3.10	84.34	6.14
56.3–94.1	Min	45.12	82.23	1.33	0.38	2.64	72.41	2.62
mbsf	Max	70.77	242.10	1.66	0.88	4.07	92.52	12.37
	SE	0.91	5.47	0.01	0.02	0.04	0.75	0.33
IIIB	N(33)	60.26	155.26	1.42	0.55	2.94	83.38	5.15
94.1–118.1	Min	48.91	95.70	1.32	0.40	1.98	65.87	1.93
mbsf	Max	68.65	218.96	1.50	0.85	4.23	97.32	8.54
	SE	0.84	5.41	0.01	0.02	0.06	0.99	0.27
IV	N(107)	60.94	157.54	1.41	0.56	2.72	83.7	5.31
118.1–197.3	Min	43.16	75.92	1.03	0.37	2.30	62.42	1.66
mbsf	Max	70.32	236.87	1.69	0.89	3.92	99.45	9.92
	SE	0.43	2.73	0.01	0.01	0.02	0.47	0.14
V	N(26)	47.13	91.55	1.57	0.83	2.90	71.72	2.71
197.3–216.3	Min	35.80	55.75	1.42	0.57	2.46	55.74	1.26
mbsf	Max	58.86	143.10	1.74	1.13	4.49	81.94	4.54
	SE	1.19	4.31	0.02	0.03	0.09	1.27	0.16
G-I	N(62)	39.58	68.51	1.72	1.02	2.84	65.38	1.90
0–45	Min	21.71	27.74	1.42	0.56	2.66	44.25	0.75
mbsf	Max	59.08	144.39	2.23	1.58	3.24	83.86	3.83
	SE	0.98	3.04	0.02	0.03	0.01	1.04	0.09
G-II	N(41)	55.68	138.05	1.53	0.66	3.03	81.31	5.57
45–75	Min	33.01	49.27	1.33	0.38	1.50	59.91	1.49
mbsf	Max	70.77	242.10	1.89	1.21	3.70	92.52	12.37
	SE	1.67	8.43	0.02	0.04	0.05	1.38	0.46
G-III	N(166)	60.32	155.44	1.42	0.55	2.82	83.59	5.31
75–197	Min	43.16	75.92	1.03	0.37	1.98	62.42	1.66
mbsf	Max	70.32	236.87	1.68	0.93	4.23	99.45	9.92
	SE	0.37	2.27	0.01	0.01	0.02	0.39	0.11

Table 15 (continued).

Unit		WC-w (%)	WC-d (%)	WBD[a] (g/cm³)	DBD[b] (g/cm³)	GD[b] (g/cm³)	Por[a] (%)	VR[a]
G-IV	N(26)	47.13	91.55	1.57	0.83	2.90	71.72	2.71
197–216.3	Min	35.80	55.75	1.42	0.57	2.46	55.74	1.26
mbsf	Max	58.86	143.10	1.74	1.30	4.49	81.94	4.54
	SE	1.19	4.31	0.02	0.03	0.09	1.27	0.16

Notes: WC-w = wet water content (% wet sample weight); WC-d = dry water content (% dry sample weight); WBD = wet-bulk density; DBD = dry-bulk density; GD = grain density; Por = porosity; VR = void ratio; SE = standard error. I to V = lithologic units; G-I to G-IV = geotechnical units.
[a]Value calculated using Method B.
[b]Value calculated using Method C.

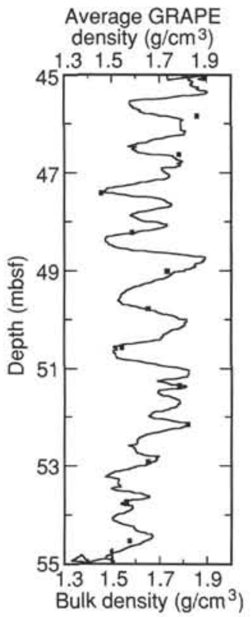

Figure 42. Smoothed GRAPE density (solid curve) and discrete laboratory determinations of bulk density (filled squares) plotted vs. depth for Core 151-907A-6H. The fluctuations in GRAPE density illustrate textural changes in the core between fine-grained, high-density intervals and coarser-grained, low-density intervals; discrete measurements at lower sample resolution correlate well with the GRAPE density values.

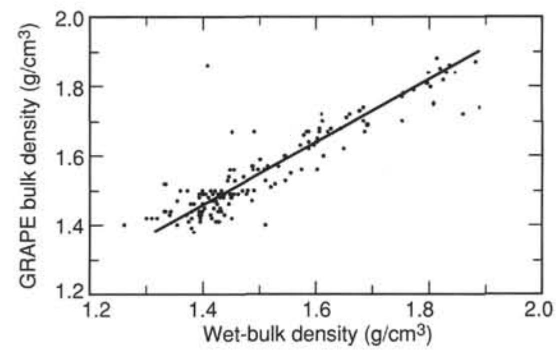

Figure 43. Relationship between GRAPE density and laboratory determinations of bulk density (Method B) for Hole 907A. The regression equation for this relationship is $y = -0.20242 + 1.1002x$; $R = 0.88147$.

Table 16. Summary of logging operations at Hole 907A.

6 Aug. 1993	
21:00	Last core on deck; prepare hole for logging.
7 Aug.	
	Pipe set at 83 mbsf.
03:15	Rig up NGT-DSI-DITE (+TLT).
04:28	RIH with NGT-DSI-DITE.
05:10	Cable head shorted out; POOH.
06:28	RIH with NGT-DSI-DITE having changed cable head.
07:25	"Repeat" upgoing log from TD (now 198.4 mbsf) to 134 mbsf.
07:53	Main upgoing log from TD to mud line (pipe pulled to 63 mbsf). POOH.
10:30	Rig up NGT-CNT-HLDT (+TLT).
11:15	RIH with NGT-CNT-HLDT.
11:59	"Repeat" upgoing log from TD (now 192.4 mbsf) to 134 mbsf.
12:18	Main upgoing log from TD to EOP (pulled to 63 mbsf). POOH.
13:30	Rig up NGT-FMS.
14:05	RIH with NGT-FMS.
14:54	Main upgoing log from TD (192.4 mbsf) to EOP (pulled to 63 mbsf).
15:22	Repeat upgoing log from 138.4 to EOP (caliper too large in base of hole). POOH.
16:45	Rig up NGT-AACT-GST (+TLT).
17:20	RIH with NGT-AACT-GST.
18:18	Main upgoing log from TD (now 189.3) to 74.5 mbsf.
18:58	Tool unable to enter into base of pipe. Repeated attempts to enter base of pipe failed. Suspected closed flapper, pumped mud in attempt to open flapper valve to no avail.
21:00	Decision made to crimp and cut cable.
21:25	Crimper sent down.
22:45	Cutter dropped down.
23:15	Spooled in cable and commenced pulling pipe.
8 Aug.	
03:55	Recovered tool on rig floor (hanging immediately below bit; flapper valve closed).

Notes: Times given in Universal Time Coordinated (UTC). Drillers TD (total depth) = 224.1 mbsf; WD (water depth) = 1811.6 mbrf; POOH = pull out of hole; RIH = run in hole; EOP = end of pipe. For explanation of logging tools, see "Downhole Measurements" section, this chapter.

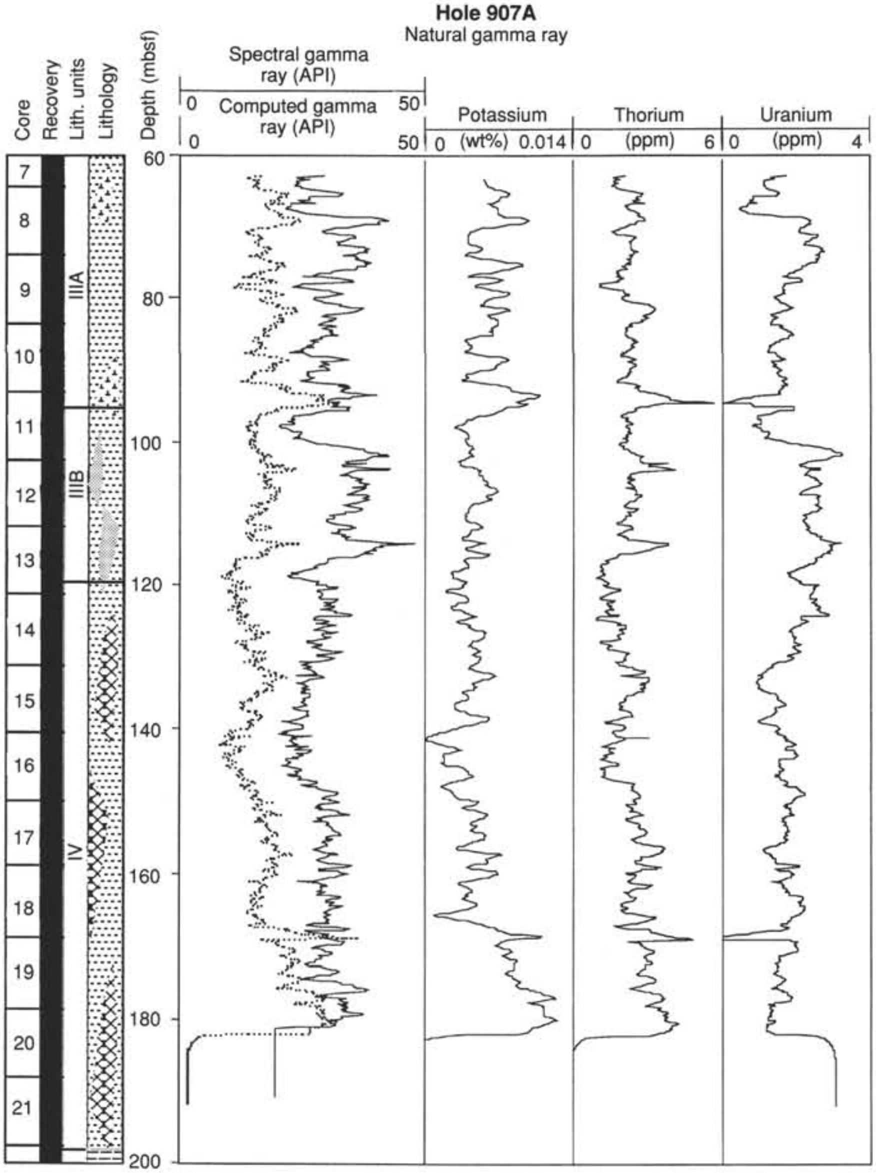

Figure 44. Data from the natural gamma-ray spectrometry tool (NGT) recorded on the seismic stratigraphy (63–161 mbsf) and Formation MicroScanner (161–182 mbsf) tool strings.

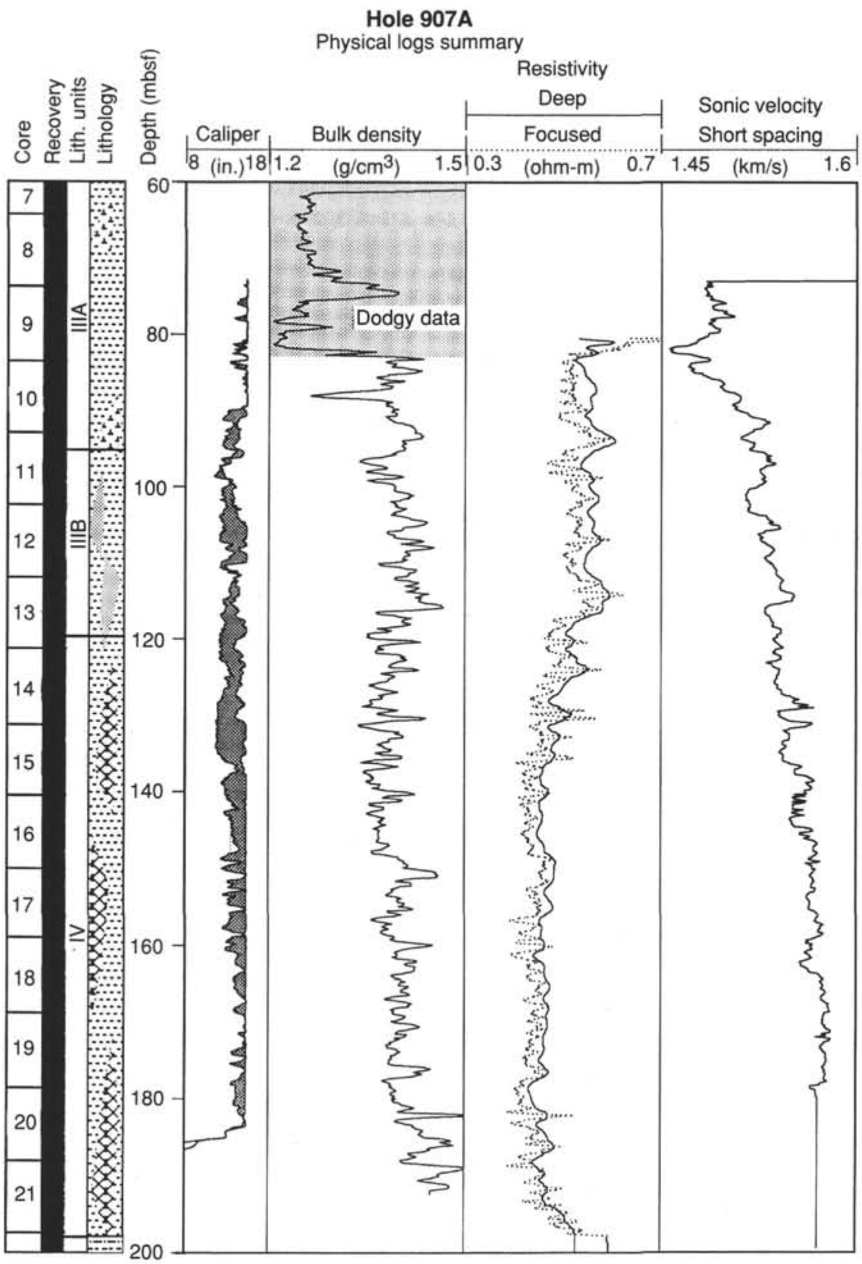

Figure 45. Orthogonal caliper data from Formation MicroScanner (FMS) shown with: bulk-density data from the high-temperature lithodensity tool (HLDT); deep phasor induction and spherically focused resistivity from the phasor dual induction tool (DIT); sonic velocity from the dipole shear sonic imager (DSI).

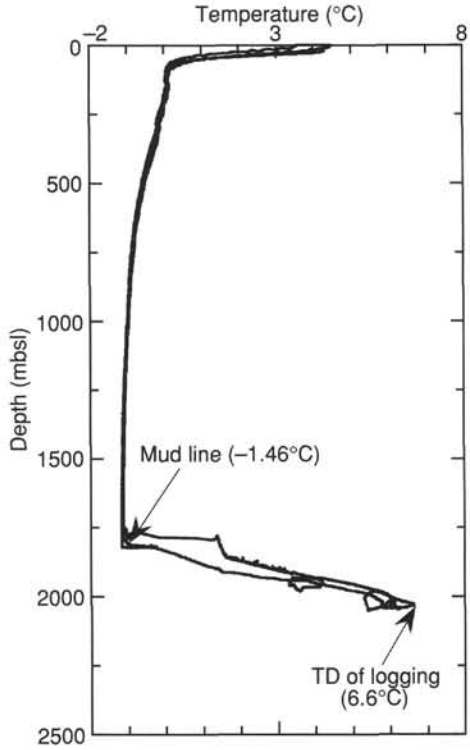

Figure 46. Temperature data recorded by the Lamont-Doherty temperature logging tool (TLT) on the seismic stratigraphy tool string, the first tool string to be run in Hole 907A. TD = total depth in hole.

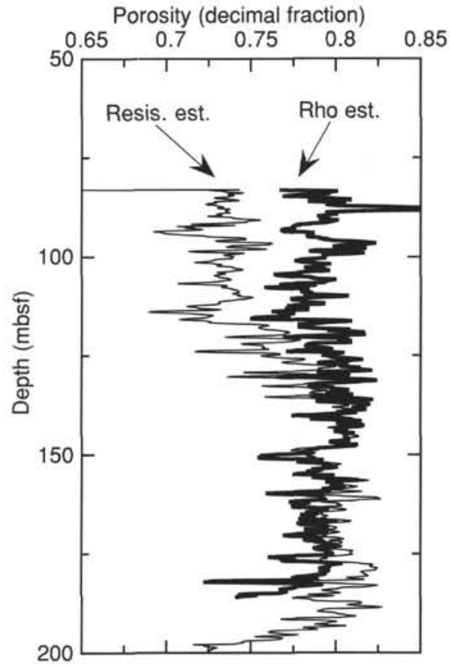

Figure 48. Comparison of porosity profiles derived from the resistivity and density logs. The resistivity-porosity is derived by applying Archie's law to the deep resistivity log of the dual induction tool (DIT). The density-porosity is determined from the wet-bulk-density log from the high-temperature lithodensity tool (HLDT) using a constant grain density of 2.8 g/cm^3. Resis. est. = estimate from resistivity; Rho est. = estimate from bulk density.

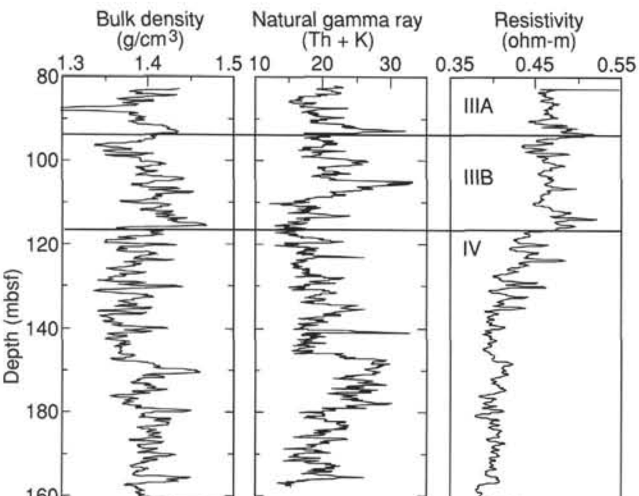

Figure 47. Comparison of the wet-bulk density, computed gamma-ray, and medium induction log data from Hole 907A.

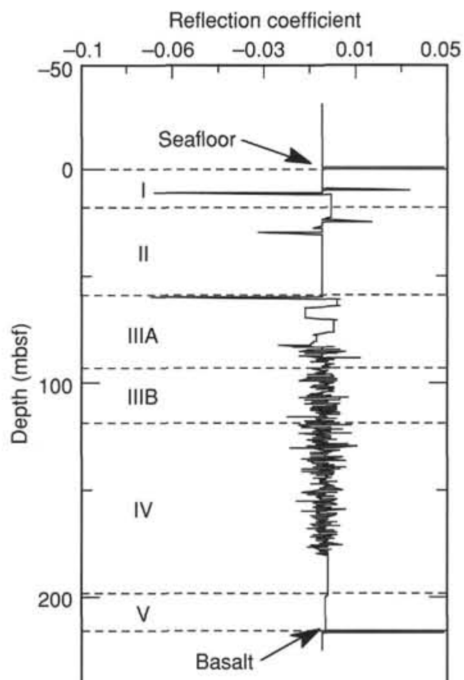

Figure 49. Reflection coefficient vs. depth at Site 907. Also shown are the lithostratigraphic unit boundaries from the "Lithostratigraphy" section (this chapter).

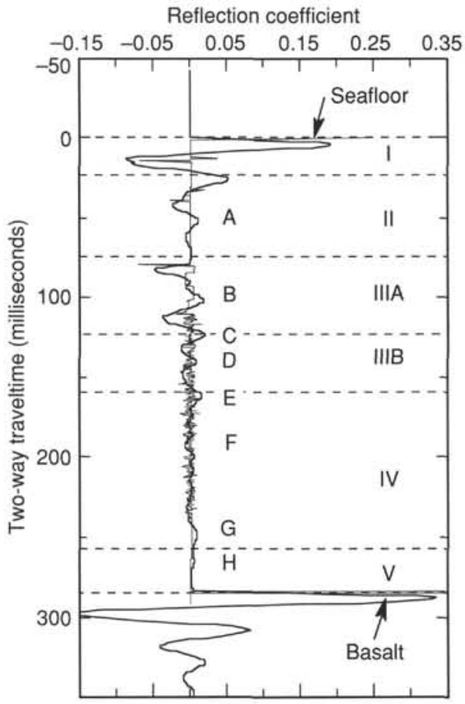

Figure 50. Reflection coefficient and synthetic seismogram shown against two-way traveltime. Locations of lithostratigraphic unit boundaries have been interpolated onto the figure.

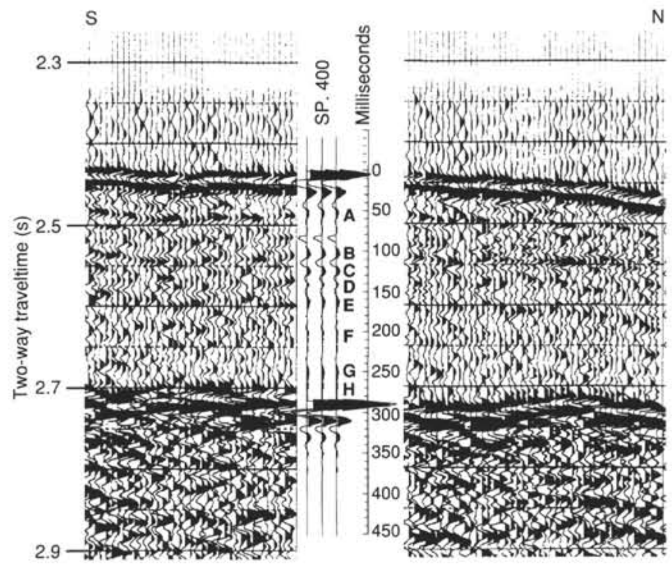

Figure 51. Comparison between synthetic seismogram from Site 907 and equivalent seismic section measured on ICEP1-89 Segment A. Reflector E marks the boundary between the biosiliceous upper/middle Miocene sediments and the detrital upper sediment column (lithostratigraphic Unit III/IV boundary). A–H = potential reflectors.

SHORE-BASED LOG PROCESSING

Hole 907A

Bottom felt: 1811.6 mbrf (used for depth shift to seafloor)
Total penetration: 224.1 mbsf
Total core recovered: 229.98 m (102%)

Logging Runs

Logging string 1: DIT/DSI/NGT
Logging string 2: HLDT/CNTG/NGT
Logging string 2: HLDT/CNTG/NGT
Logging string 3: FMS/GPIT/NGT (two passes)
Logging string 4: ACT/GST/NGT

Wireline heave compensator was used to counter ship heave resulting from the mild sea state conditions.

Drill Pipe/Bottom-hole Assembly/Casing

The following drill pipe depths are as they appear on the logs after differential depth shift (see **Depth shift** section) and depth shift to the seafloor. As such, there might be a discrepancy with the original depths given by the drillers on board. Possible reasons for depth discrepancies are ship heave, use of wireline heave compensator, and drill-string and/or wireline stretch.

DIT/DSI/NGT: Because the drill pipe was moved when the tool string was approaching the end of the pipe, each tool entered the pipe at different depths:

DIT: Bottom of drill pipe at ~83 mbsf.

NGT: Bottom of drill pipe at ~64.5 mbsf.

DSI: Bottom of drill pipe at ~76 mbsf.

HLDT/CNTG/NGT: Bottom of drill pipe at 62.5 mbsf.

FMS/GPIT/NGT: Bottom of drill pipe at 62.4 mbsf. Neither pass entered the pipe.

ACT/GST/NGT: Bottom of drill pipe at 76 mbsf.

Processing

Depth shift: All logs have been interactively depth shifted with reference to NGT from FMS/GPIT/NGT (main pass), and to the seafloor (–1811.6 m). A list of the amount of differential depth shifts applied at this hole is available upon request.

Gamma-ray processing: NGT data have been processed to correct for borehole size and type of drilling fluid.

Acoustic data processing: DSI (Dipole Sonic Imager) data were reprocessed on the shipboard MAXIS system.

Geochemical processing: (For detailed explanation of the processing, please refer to the "Explanatory Notes" chapter [this volume] or to the "geochem.doc" file on the enclosed CD-ROM). The elemental yields recorded by the GST tool represent the relative contribution of only some of the rock-forming elements (iron, calcium, chlorine, silica, sulfur, hydrogen, gadolinium, and titanium—the last two computed during geochemical processing) to the total spectrum. Because other rock-forming elements (such as aluminum, potassium, etc.) are present in the formation, caution is recommended in using the yields to infer lithologic changes. Instead, ratios (see "acronyms.doc" on CD-ROM) are more appropriate to determine changes in the macroscopic properties of the formation. A list of oxide factors used in geochemical processing includes the following:

$SiO_2 = 2.139$
$CaO = 1.399$
$FeO^* = 1.358$
$TiO_2 = 1.668$
$K_2O = 1.205$
$Al_2O_3 = 1.889$

FeO^* computed using an oxide factor that assumes a 50:50 combination of Fe_2O_3 and FeO factors.

Because the weight percent of calcium is zero or negative through the entire hole, to improve the calculation of the elemental yields of the other elements, the calcium yield has been redistributed among the other yields by using the proprietary Schlumberger repartitioning coefficients.

Quality Control

Hole diameter was recorded by the hydraulic caliper on the HLDT tool (CALI) and by the caliper on the FMS string (C1 and C2).

Invalid gamma-ray data were detected at 37, 48, and 57 mbsf (DIT/DSI/NGT string).

FACT = quality control curve in geochemical processing. Accuracy of the estimates is inversely proportional to the magnitude of the curve.

Note: Details of standard shore-based processing procedures are found in the "Explanatory Notes" chapter, this volume. For further information about the logs, please contact:

Cristina Broglia
Phone: 914-365-8343
Fax: 914-365-3182
E-mail: chris@ldeo.columbia.edu

Elizabeth Pratson
Phone: 914-365-8313
Fax: 914-365-3182
E-mail: beth@ldeo.columbia.edu

Hole 907A: Density-Porosity-Natural Gamma Ray Log Summary

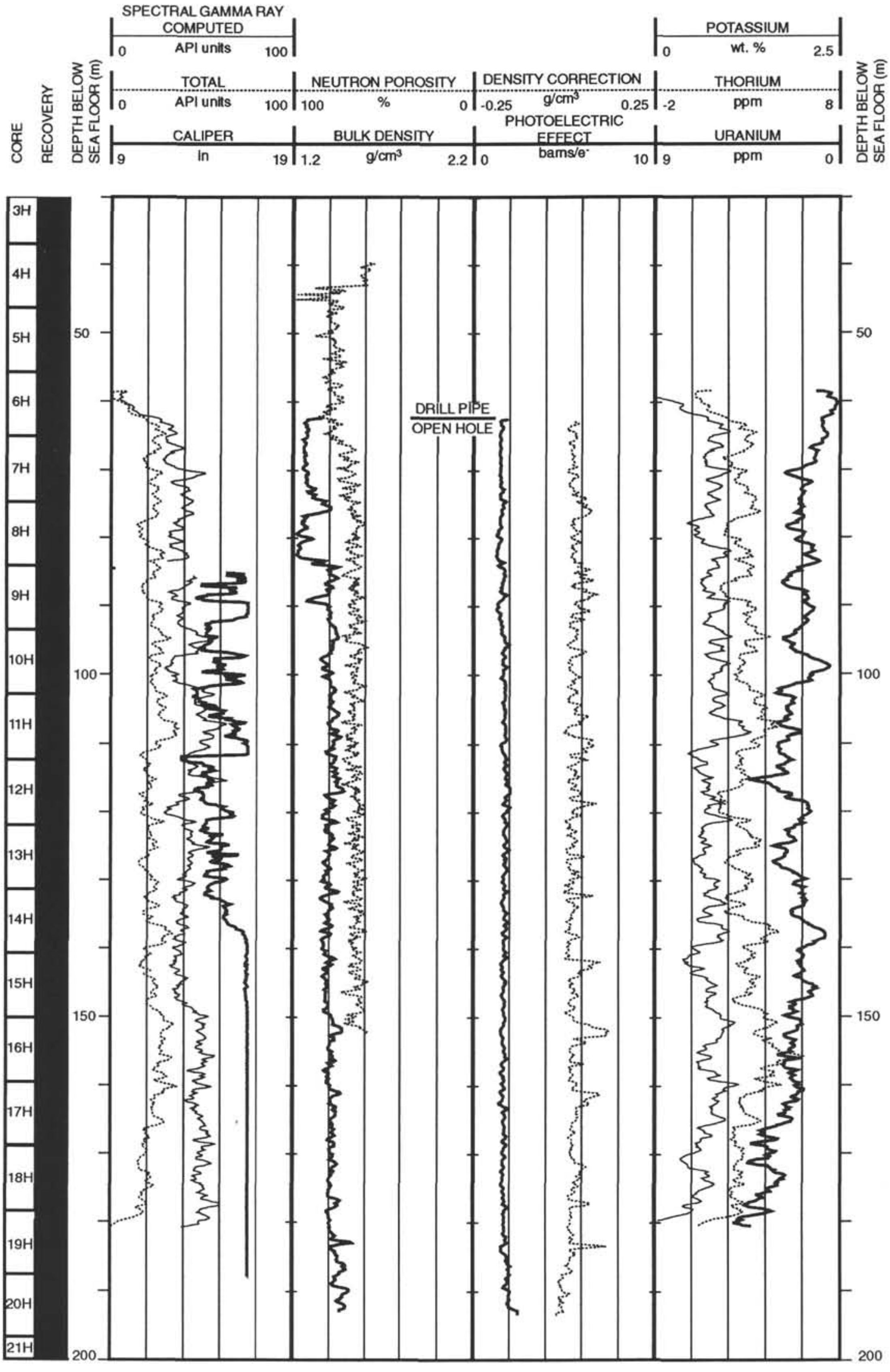

Hole 907A: Resistivity-Velocity-Natural Gamma Ray Log Summary

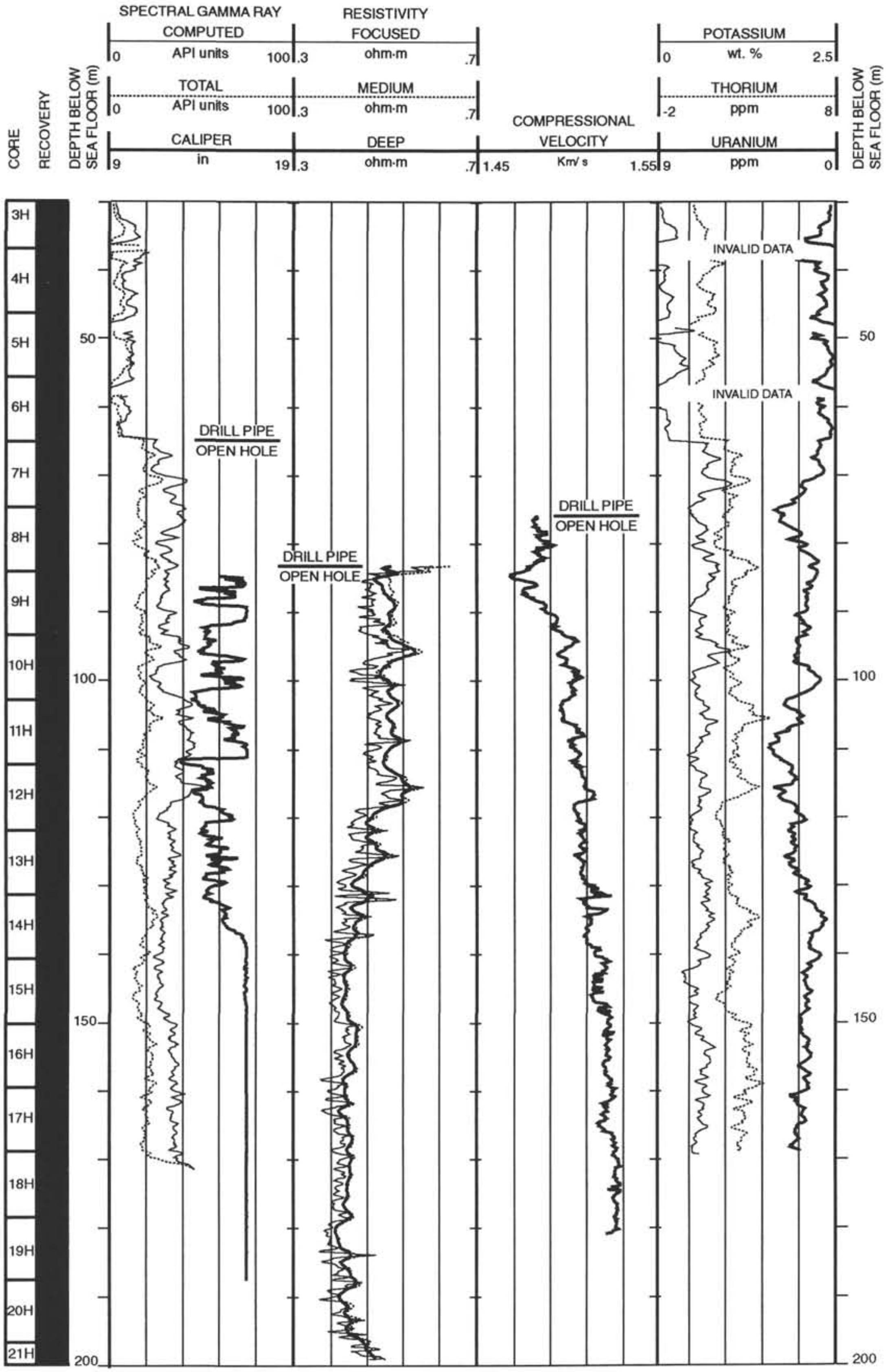

Hole 907A: Processed Geochemical Log Summary

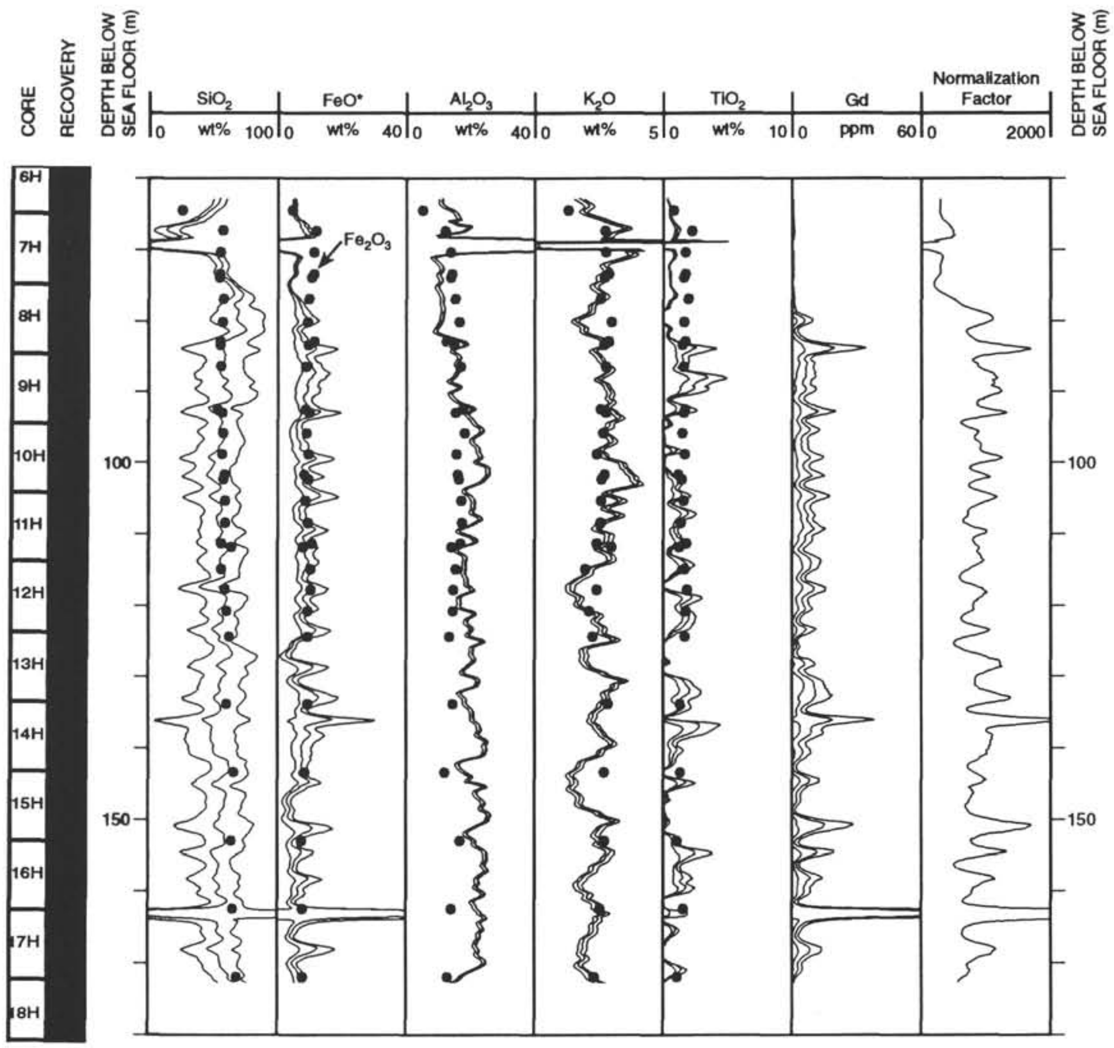

Hole 907A: Natural Gamma Ray Log Summary